

FREIE UNIVERSITÄT BERLIN

Probing the Structure and Dynamics of Disordered Systems by MD-averaged *ab initio* Magnetic Resonance

INAUGURAL-DISSERTATION

to obtain the academic degree

Doctor rerum naturalium (Dr. rer. nat.)

submitted to the Department of Biology, Chemistry and Pharmacy
of Freie Universität Berlin

by

Hossam Elgabarty

from Cairo, Egypt

Berlin, 2013



1st Reviewer: Prof. Dr. Daniel Sebastiani

2nd Reviewer: Prof. Dr. Beate Paulus

Date of defense: 29.08.2013

Acknowledgments

I would like to express my sincere gratitude to my advisor Prof. Daniel Sebastiani not only for the continuous support of my Ph.D study and research, his patience, and motivation, but also for his friendship. I would also like to thank Professor Beate Paulus for the insightful comments and discussions. Many thanks are also due to other members of the Sebastiani research group in Berlin.

On the domestic front, encouragement always came from my parents, my in-laws, my brothers, but most important, from my wife, Heba, who cheerfully stood by me throughout, and did a wonderful job raising up our daughter Laila at times when I was far too busy to contribute more than a few hours a day.

Hossam Elgabarty

List of Publications

- Heller, J.; Elgabarty, H.; Zhuang, B.; Sebastiani, D. and Hinderberger, D. '*Solvation of small disulfonate anions in water/methanol mixtures characterized by high-field pulse electron nuclear double resonance and molecular dynamics simulations.*' J. Phys. Chem. B, **2010**, 114, 7429-38.
- Elgabarty, H.; Wolff, M.; Glaubitz, A.; Hinderberger, D. and Sebastiani, D. '*First principles calculation of inhomogeneous broadening in solid-state cw-EPR spectroscopy.*' Phys. Chem. Chem. Phys., **2013**, Article In Press.
- Elgabarty, H.; Schmieder, P. and Sebastiani, D. '*Unraveling the existence of dynamic water channels in light-harvesting proteins: alpha-C-phycocyanobilin in vitro.*' Chem. Sci., **2013**, 4, 755-763.

Contents

1	Introduction	1
2	Theory	5
2.1	Molecular Dynamics Simulations	5
2.1.1	Integrating the classical equations of motion	5
2.1.2	MD simulations in the canonical ensemble	7
2.1.3	MD simulations with Force fields	9
2.1.4	Born-Oppenheimer <i>ab initio</i> Molecular Dynamics	10
2.2	Magnetic Resonance Spectroscopy	13
2.2.1	Basic Theory of Magnetic Resonance	13
2.2.2	The Empirical Spin Hamiltonian	14
2.2.3	The <i>ab initio</i> Spin Hamiltonian	15
3	Summary of the Published Papers	27
3.1	Paper I	27
3.2	Paper II	30
3.3	Paper III	34
4	Paper I	39
5	Paper II	51
6	Paper III	61
7	Conclusion	73
	English Summary	75
	German Summary	77
	Bibliography	79

Chapter 1

Introduction

The determination of the detailed microscopic structure and dynamics of (aqueous) solutions is still a challenge for modern physics and chemistry. Unlike the situation in crystalline systems where scattering experiments can provide very accurate atomic coordinates, aqueous systems (and frozen glasses) lack the required long-range order, which limits the applicability of these scattering techniques. The situation is even more challenging for heterogeneous mixtures of solvents, where small scale structural inhomogeneities and preferential solvation are also possible [Dixit et al. 2002, Guo et al. 2003, Lin et al. 2012, Asenbaum et al. 2012, Corsaro et al. 2013]. For such systems magnetic resonance spectroscopy has particularly proven to be highly valuable as it is able to probe the local structure around a spin without the need for long-range order, and at the same time with extremely high sensitivity to the local chemical environment like solvent polarity and fluctuations in the hydrogen bonding network.[Callaghan 2011, Kaupp et al. 2006, Sebastiani and Rothlisberger 2004, Corsaro et al. 2013].

In magnetic resonance spectroscopy, one probes transitions between energy levels which depend on the strength of a magnetic field. Systems that exhibit magnetic resonance always possess both magnetic moments and angular momentum¹, and the observed resonance is with the frequency of gyroscopic precession of the magnetic moment in an external magnetic field [Slichter 1996]. Magnetic resonance frequencies typically fall in the radio frequency region (for nuclear spins) or microwave region (for electron spins). Although the physical principles behind *nuclear magnetic resonance* (NMR) and *electron paramagnetic resonance* (EPR²) are essentially the same, there are significant differences in the magnitudes and signs of the magnetic interactions involved, and hence in the relevant time scales, which not only lead to significant differences in the historical development, experimental techniques, and fields of applications [Slichter 1996, Callaghan 2011], giving each of them its distinct flavor, but this probably also had a direct impact on the development of computational techniques to calculate NMR and EPR spectroscopic parameters [Carrington and McLachlan 1967, Neese and Munzarova 2004, Pyykkö 2004].

One of the most prominent features of magnetic resonance spectral parameters is their extremely strong dependence on the electronic structure and geometry of the system, which makes them ideal tools to probe matter at the atomic level of detail [Slichter 1996]. A known example is the well-established correlation in silicates between ²⁹Si NMR chemical shifts and

¹For our purposes these are always spins and their associated magnetic moments

²Also known as *electron spin resonance* (ESR). Strictly the two terms could have a slightly different meaning, but they are ubiquitously used interchangeably. Harriman [1978] discusses this point in the preface to his authoritative monograph.

the Si–O bond lengths, with a chemical shift difference of 0.1 ppm corresponding to a change of the bond length by only 0.00001 Å [Malkin et al. 1995, Grimmer 1993]. A very early example in ESR was the determination of the orientation of the heme groups in hemoglobin crystals from the g tensor of the iron (III) ion [Bennett and Ingram 1955, Ingram and Bennett 1954]. The iron ion lies at the center of a small moiety that is part of a large protein structure (Molecular weight \approx 20 kDa) and yet we can “see” the spin distribution associated with the valency electrons around one particular atom [McWeeny 2004, p. 65].

The interpretation of the rich and detailed information presented by magnetic resonance spectroscopy has always been challenging and spectroscopists are always looking for more elaborate tools to interpret their spectra. Perhaps a major milestone in the development of magnetic resonance spectroscopy was the introduction of the effective spin Hamiltonian in the 1950s [Pryce 1950], which has been described as “a major intellectual achievement with far reaching consequences for the development of EPR and NMR spectroscopy” [Neese and Munzarova 2004]. The spin Hamiltonian is an effective Hamiltonian containing only spin degrees of freedom interacting with each other and with the external magnetic field via numerical parameters (the spin Hamiltonian parameters) that are obtained from fitting to the experimental data [Neese and Munzarova 2004]. With the spin Hamiltonian, recourse to the extremely complicated underlying microscopic physics in the system becomes not necessary, or at least it can come at a later stage. Moreover, it is not only the summarizing of experimental findings that is greatly facilitated, but also the design of new experiments and pulse sequences [Schweiger and Jeschke 2001]. With the spin Hamiltonian available, theoretical NMR and EPR spectroscopy is thus reduced to predicting its parameters [Neese and Munzarova 2004]. In this regard, the introduction of Density functional theory (DFT) was a turning point for the calculations of the spin Hamiltonian parameters, for it has been shown to provide remarkably accurate values at reasonable computational costs [Al Derzi et al. 2003, Barone et al. 2006, Lund et al. 2007, Barone and Cimino 2009, Gauss et al. 2009, Arbuznikov et al. 2002, Neese 2001, Pauwels et al. 2011]. Although some of these parameters are available at much higher levels of theory [Gauss and Stanton 1995*b*; *a*; 1996, Gauss et al. 2009], the prohibitive scaling of these methods with the system size makes DFT the method of choice for large complex systems, especially when environmental and solvent effects are to be taken into account explicitly which is crucial if for example one wants to study heterogeneous solvent mixtures and solvation in them. In fact, the calculation of magnetic resonance parameters for liquids and solutions has only become possible in the last two decades. To this end, most accurate calculations use simulations followed by quantum chemical calculations to compute the parameter of interest [Searles and Huber 2004, Sebastiani and Parrinello 2001, Murakhtina et al. 2006]. In using molecular dynamics (MD) simulations to compute magnetic resonance parameters, the simulations may serve many purposes. One can simply use the simulations as a means to extract typical fluid/solvent configurations, and in this case, classical MD, *ab initio* MD and hybrid quantum mechanical-classical simulations (QMMM) MD have proven highly-successful [Searles and Huber 2004, Asher et al. 2004, Asher and Kaupp 2007, Pavone et al. 2004, Pavone, Cimino, De Angelis and Barone 2006, Pavone, Sillanpää, Cimino, Crescenzi and Barone 2006, Pavone et al. 2007, Pauwels et al. 2011]. Since the dynamics of the system leaves its highly-valuable fingerprint on the magnetic resonance lineshape, one can also use the MD trajectory to extract the relevant correlation times and relaxation rates [*e.g.* Schmidt et al. 2008] or even simulate the full magnetic resonance lineshape [Barone et al. 2006].

In this doctoral research, a number of studies have been performed that all share the common theme of combining the techniques of (*ab initio*) MD simulations with the *ab initio* calculation of magnetic resonance parameters (both NMR and EPR) to study condensed disordered systems under realistic thermodynamic conditions. In all cases the work was performed in

collaboration with experimental laboratories (the Max Planck Institute for Polymer Research and the Leibniz-Institut für Molekulare Pharmakologie), and the results of theory and experiment could be closely compared. The publications that have appeared in international journals based on this work are the core of this thesis and are fully reproduced as an integral part of it. The first system studied is a small inorganic free radical, Fremy's salt [Moser and Howie 1968], solvated in a mixture of water and methanol, a solvent mixture that has been shown to be microheterogeneous [Dixit et al. 2002, Guo et al. 2003, Lin et al. 2012, Asenbaum et al. 2012, Corsaro et al. 2013], and when frozen, gives a spectroscopically "poorly characterized" system where heterogeneous broadening of spectral lineshapes has additional contributions from "strain" effects and unresolved hyperfine coupling to solvent. The other system is the alpha-C-phytyocyanin protein with its chromophore, phytyocyanobilin, in aqueous solution. In both cases, the combination of (*ab initio* and QM/MM) simulations with MD-ensemble averaged magnetic resonance parameters not only yielded spectroscopic parameters in close agreement with experiment, but also gave deep insight into detailed atom-level structure, solvation, and dynamics of the system that in fact shed new light on the interpretation of the experimental findings.

The thesis is organized as follows: after this introduction, chapter 2 is dedicated to a discussion of the theoretical background of the methods used in this work. Since this thesis is focused on the combination of two techniques: *ab initio* magnetic resonance spectroscopy and (*ab initio*) MD simulations, the chapter is split into two roughly-equal parts discussing each technique in turn. chapter 3 gives an overview of the work done and the major findings, which is then followed by a full reproduction of the three published papers (chapters 4 to 6), and finally chapter 7 concludes the thesis.

Chapter 2

Theory

2.1 Molecular Dynamics Simulations

The essence of molecular dynamics simulations is the solution of the atomic and molecular many body problem by numerically integrating the (classical) equations of motion. With the immensely broad range of problems that can be tackled with such an approach, this technique has proved itself indispensable both in pure and applied research [Rapaport 2004]. In any molecular dynamics simulation there are three principal “axes” [Tuckerman 2010]: there is the model that describes the inter-particle interactions (empirical, semiempirical, *ab initio*), there is also the calculation of energies and forces from the chosen model, but at the heart of all this, there is the numerical integrator, the algorithm used to integrate the equations of motion.

2.1.1 Integrating the classical equations of motion

The Verlet algorithm

We start by a Taylor series expansion up to second order for the position of a particle at time $t + \Delta t$:

$$\begin{aligned}\mathbf{r}_i(t + \Delta t) &\approx \mathbf{r}_i(t) + \Delta t \dot{\mathbf{r}}_i(t) + \frac{1}{2} \Delta t^2 \ddot{\mathbf{r}}_i(t) \\ &\approx \mathbf{r}_i(t) + \Delta t \mathbf{v}_i(t) + \frac{\Delta t^2}{2m_i} \mathbf{F}_i(t)\end{aligned}\tag{2.1}$$

One can get rid of the velocity term in eq. (2.1) by writing a similar expansion for $\mathbf{r}_i(t - \Delta t)$:

$$\mathbf{r}_i(t - \Delta t) \approx \mathbf{r}_i(t) - \Delta t \mathbf{v}_i(t) + \frac{\Delta t^2}{2m_i} \mathbf{F}_i(t),\tag{2.2}$$

and adding eq. (2.1) and eq. (2.2):

$$\mathbf{r}_i(t + \Delta t) \approx 2\mathbf{r}_i(t) - \mathbf{r}_i(t - \Delta t) + \frac{\Delta t^2}{m_i} \mathbf{F}_i(t)\tag{2.3}$$

Equation (2.3) is the well-known *Verlet algorithm* [Verlet 1967]. Given a starting point in the

phase space, one can use eq. (2.1) to generate a set of coordinates at time Δt , which can then be propagated using eq. (2.3) to a trajectory of arbitrary length. The Verlet algorithm does not generate velocities, they can be computed at any point though as a centered difference:

$$\mathbf{v}_i(t) = \frac{\mathbf{r}_i(t + \Delta t) - \mathbf{r}_i(t - \Delta t)}{2\Delta t} \quad (2.4)$$

It is interesting to note that by adding eq. (2.1) and eq. (2.2) we get rid of all the odd-order terms, thus the *local* error in the Verlet algorithm is $\mathcal{O}(\Delta t^4)$, even though eq. (2.3) contains no explicit third-order term [Haile 1992].

The velocity Verlet algorithm

The Verlet algorithm has the disadvantage of *not generating* the complete phase space trajectory on the fly, as it does not propagate the velocities. The velocity Verlet algorithm [Swope et al. 1982] is a variant that explicitly evolves both positions and velocities.

Since the Newton's equations of motion are time-reversible, one can evolve eq. (2.1) in the reverse direction, i.e. start from $\mathbf{r}_i(t + \Delta t)$ and move by a time step of $-\Delta t$:

$$\mathbf{r}_i(t) \approx \mathbf{r}_i(t + \Delta t) - \Delta t \mathbf{v}_i(t + \Delta t) + \frac{\Delta t^2}{2m_i} \mathbf{F}_i(t + \Delta t) \quad (2.5)$$

substituting the value of $\mathbf{r}_i(t + \Delta t)$ from eq. (2.1) into eq. (2.5) and solving for $\mathbf{v}_i(t + \Delta t)$:

$$\mathbf{v}_i(t + \Delta t) \approx \mathbf{v}_i(t) + \frac{\Delta t}{2m_i} [\mathbf{F}_i + \mathbf{F}_i(t + \Delta t)] \quad (2.6)$$

The velocity Verlet algorithm is simply eqs. (2.1) and (2.6), thus it propagates positions and velocities simultaneously. Both the Verlet and the velocity Verlet algorithms possess two properties that are crucial for the long-time stability of numerical solvers. They both satisfy time-reversibility, that is propagating the equations backward in time will trace back the same trajectory. Time-reversibility is a fundamental symmetry of the classical equations of motion that should be preserved by a numerical integrator. Another important property that both integrators satisfy is the symplectic property¹. A symplectic algorithm has the important property that there exists a “*shadow*” Hamiltonian that along a trajectory remains close to the true Hamiltonian (*i.e.* approaches the exact Hamiltonian as $\Delta t \rightarrow 0$) and is exactly conserved by the map, thus ensuring that the numerical trajectory remains close to the true constant energy hypersurface [Tuckerman 2010, pp.121–123]. There are other integrators that are accurate to higher than second order, but yet many of these methods are neither symplectic nor

¹Introducing a phase space vector \mathbf{x} , Hamilton's equations can be written in the form:

$$\dot{\mathbf{x}} = \mathbf{M} \frac{\partial \mathcal{H}}{\partial \mathbf{x}} \quad (2.7)$$

where M is a block matrix:

$$\mathbf{M} = \begin{pmatrix} \mathbf{0} & \mathbf{I} \\ -\mathbf{I} & \mathbf{0} \end{pmatrix}$$

and $\mathbf{0}$ and \mathbf{I} are the zero and identity matrices. Equation eq. (2.7) constitutes the so-called symplectic structure [Tuckerman 2010, p. 23]. The time evolution of a system described by eq. (2.7) from \mathbf{x}_0 to \mathbf{x}_t can be viewed as a coordinate transformation with a Jacobian matrix \mathbf{J} which satisfies:

$$\mathbf{M} = \mathbf{J}^T \mathbf{M} \mathbf{J} \quad (2.8)$$

Equation (2.8) is known as the symplectic property.

time-reversible and lead to significant drifts in the total energy when used [Tuckerman 2010, p. 101].

2.1.2 MD simulations in the canonical ensemble

Starting with a number of particles N in a fixed volume V , a trajectory computed via the algorithms described in subsection 2.1.1 would allow us to follow the time evolution of the system on a constant energy hypersurface in the phase space *i.e.* E is a constant of motion. According to the ergodic hypothesis², a time average taken over the trajectory would correspond to an ensemble average, in this case the microcanonical (constant NVE) ensemble. However, it is very often more convenient to perform simulations that would sample from other ensembles. In order to reflect the more common experimental conditions, it is important to be able to sample from the canonical ensemble (constant NVT), or the isothermal-isobaric ensemble (constant NPT). For this aim, two rather different general approaches have been developed. One is based on mixing Newtonian MD with certain Monte Carlo moves, and the other is based on a reformulation of the Lagrangian equations of motion [Frenkel and Smit 2001].

The Nosé-Hoover thermostat

One of the more popular thermostats is the extended-ensemble approach first proposed by Nosé [1984a;b] and later modified by Hoover [1985]. Here, we follow closely the presentation given by Tuckerman [2010]. The Nosé Hamiltonian for a system of N particles contains an additional degree of freedom s and its conjugate momentum p_s :

$$\mathcal{H}_{\text{Nosé}} = \sum_{i=1}^N \frac{\mathbf{p}_i^2}{2m_i s^2} + U(\mathbf{r}_1, \dots, \mathbf{r}_N) + \frac{p_s^2}{2Q} + gkT \ln s \quad (2.9)$$

where $U(\mathbf{r}_1, \dots, \mathbf{r}_N)$ is the potential energy, k and T are the Boltzmann constant and the target temperature respectively, and g is equal to $3N + 1$. s acts as an “agent” that scales the velocities to shift the instantaneous kinetic energy towards the target level. Q is a parameter, with units of energy \times time², that determines the time scale on which the “thermostat” acts, and also can be viewed as an “effective mass” for s . In the extended system described by eq. (2.9), $\mathcal{H}_{\text{Nosé}}$ is conserved, and therefore we have a microcanonical ensemble. However, the “potential” term for s , $gkT \ln s$, was chosen such that the microcanonical distribution of the total $6N + 2$ -dimensional phase space of $\mathcal{H}_{\text{Nosé}}$ gives a *canonical* distribution in the physical $6N$ -dimensional phase space, which can indeed be shown to be the case by integrating the partition function of the $6N + 2$ -dimensional phase space over s and p_s [Tuckerman 2010, pp.180-181].

The equations of motion generated by $\mathcal{H}_{\text{Nosé}}$ are:

²Given an infinite amount of time, the system will be able to visit *all* configurations on the constant energy hypersurface [Tuckerman 2010, p. 98].

$$\begin{aligned}
\dot{\mathbf{r}}_i &= \frac{\partial \mathcal{H}_{\text{Nose}}}{\partial \mathbf{p}_i} = \frac{\mathbf{p}_i}{m_i s^2} \\
\dot{\mathbf{p}}_i &= -\frac{\partial \mathcal{H}_{\text{Nose}}}{\partial \mathbf{r}_i} = \mathbf{F}_i \\
\dot{s} &= \frac{\partial \mathcal{H}_{\text{Nose}}}{\partial p_s} = \frac{p_s}{Q} \\
\dot{p}_s &= -\frac{\partial \mathcal{H}_{\text{Nose}}}{\partial s} = \sum_{i=1}^N \frac{\mathbf{p}_i^2}{m_i s^3} - \frac{gkT}{s} = \frac{1}{s} \left[\sum_{i=1}^N \frac{\mathbf{p}_i^2}{m_i s^2} - gkT \right]
\end{aligned} \tag{2.10}$$

Following the reformulation by Hoover [1985] (with slight modification from Martyna et al. [1992]), eq. (2.10) can be put in a more convenient form by introducing the following change of variables:

$$\begin{aligned}
\mathbf{p}'_i &= \frac{\mathbf{p}_i}{s} \\
dt' &= \frac{dt}{s} \\
\frac{1}{s} \frac{ds}{dt'} &= \frac{d\eta}{dt'} \\
p_s &= p_\eta
\end{aligned} \tag{2.11}$$

and redefining g in eq. (2.9) to become $6N$, we end up with a new set of equations of motion:

$$\begin{aligned}
\dot{\mathbf{r}}_i &= \frac{\mathbf{p}_i}{m_i} \\
\dot{\mathbf{p}}_i &= \mathbf{F}_i - \frac{p_\eta}{Q} \mathbf{p}_i \\
\dot{\eta} &= \frac{p_\eta}{Q} \\
\dot{p}_\eta &= \sum_{i=1}^N \frac{\mathbf{p}_i^2}{m_i} - gkT
\end{aligned} \tag{2.12}$$

We see that the equation for momentum has a friction term (which can be positive or negative though) that depends on p_η , and that the evolution of this p_η is driven by the difference between the instantaneous kinetic energy and its canonical average gkT (the last equation). The friction term thus mimics the behavior of a heat bath by controlling the fluctuations in the kinetic energy, and hence the usual designation as a “thermostat”.

The Nosé-Hoover equations eq. (2.12) have an associated conserved quantity:

$$\mathcal{H}'(\mathbf{r}, \eta, \mathbf{p}, p_\eta) = \mathcal{H}(\mathbf{r}, \mathbf{p}) + \frac{p_\eta^2}{2Q} + gkT\eta, \tag{2.13}$$

which can be used to monitor the numerical stability of the simulation.

A well known problem with the Nosé-Hoover thermostat is that in some situations, they are non-ergodic. The most famous example is for a collection of harmonic oscillators. This problem can be circumvented by using Nosé-Hoover *chains*, *i.e.* coupling the variable p_η itself to a Nosé-Hoover-type thermostat using a new set of variables $\tilde{\eta}$ and \tilde{p}_η , which are in turn coupled to thermostat *ad infinitum* [Martyna et al. 1992]. Of course practically, the chain is truncated at some point giving a Nosé-Hoover chain of length N .

2.1.3 MD simulations with Force fields

Force fields are empirical potentials that – based on a “ball and spring” model for the atoms – try to reproduce the Born-Oppenheimer potential energy surface. MD forces can then be computed as the gradients of the energy with respect to nuclear Cartesian coordinates. Any force field can be defined by its three components: (1) Atom types: To improve accuracy and partially remedy ignoring the electrons in such a ball and spring model, force fields can represent one chemical element by a multitude of different atom types that differ in their parameters, thus accounting for different “bonding” environments. Force fields vary widely from very specific force fields tuned to compute particular properties of compounds composed from very few atom types (e.g. TraPPE [Martin and Siepmann 1998]), to more general purpose force fields with over a hundred atom types dedicated to specific classes of molecules (e.g. MMFF [Halgren 1996] for general organic compounds, CHARMM [MacKerell et al. 1998] for biological molecules), or even to “universal” forcefields that cover the whole periodic table (e.g. UFF [Rappe et al. 1992]). (2) Parameter set: Currently, these are mostly derived by fitting to results of *ab initio* calculations. (3) Functional form: Which is usually designed to be as simple and efficient to implement as possible, for example most force fields use a simple quadratic (harmonic) term to represent the bond-stretching energy, some use a cubic or quartic term, and very few use the more accurate Morse-potential. Similar arguments hold for the repulsive component of the Lennard-Jones potential. In general, force fields do not allow for bond breaking and formation (though “reactive” force fields do), and they require the input of the topology of the system.

The CHARMM force field is very widely used in simulations of biological systems (proteins, nucleic acids, biological membranes) [MacKerell et al. 1998, Mackerell et al. 2004, Vanommeslaeghe and Mackerell 2012]. It has the following functional form:

$$\begin{aligned}
 E = & \sum_{bonds} K_b(b - b_0)^2 + \sum_{angles} K_\theta(\theta - \theta_0)^2 + \sum_{Urey-Bradley} K_{UB}(r_{1,3} - r_{1,3;0})^2 \\
 & + \sum_{dihedrals} K_\phi(1 + \cos n\phi - \delta) + \sum_{improper} K_\psi(\psi - \psi_0)^2 \\
 & + \sum_{i,j>i} \frac{1}{4\pi\epsilon} \frac{q_i q_j}{|r_{ij}|} + 4\epsilon_{ij} \left[\left(\frac{\sigma_{ij}}{r_{ij}} \right)^{12} - \left(\frac{\sigma_{ij}}{r_{ij}} \right)^6 \right]
 \end{aligned} \tag{2.14}$$

The first five terms account for “bonded” interactions, where b_0 , θ_0 , ψ_0 , and $r_{1,3}$ respectively are the bond, angle, improper, and Urey-Bradley equilibrium values, the K ’s are the corresponding force constants, and n and δ are the dihedral (ϕ) multiplicity and phase. The last two terms are “non-bonded” interactions, represented by a Coulomb-type pairwise interaction between atoms based on their partial charges (q_i) (bonded atoms are excluded up to the third or fourth bonded neighbor), and a van der Waals term represented by the Lennard-Jones 6-12 potential [Lennard-Jones 1924] in which ϵ_{ij} is the well-depth and σ_{ij} is the distance at which the two terms in the potential exactly balance.

Given that force field MD is typically performed on large systems, by far the most expensive terms to evaluate are the non-bonded ones, which require computing pairwise distances between all (N) atoms and hence require $\mathcal{O}(N^2)$ operations. For the short-ranged van der Waals term a usual approach is to use “neighbor lists” (that need to be updated periodically), and then to compute the term only up to a cutoff distance which is covered by the neighbor list. For the electrostatic term on the other hand, the very slow decay as r^{-1} prevents the use of cutoff distances if one would like to avoid serious artifacts (see e.g. Patra et al. 2003). In this case the Ewald summation-related approaches [Ewald 1921, Essmann et al. 1995] that use

fast Fourier transform (FFT) are the standard approach, reducing the cost of the calculation to $\mathcal{O}(N \log N)$. The slowly and conditionally converging electrostatic term is replaced by two rapidly converging summations, one in real-space and the other in reciprocal space.

2.1.4 Born-Oppenheimer *ab initio* Molecular Dynamics

In *ab initio* MD, electronic structure methods are used to compute the forces on the atomic nuclei, whereas the “dynamics” is still described in terms of classical mechanics:

$$\begin{aligned} M_I \ddot{\mathbf{R}}_I(t) &= -\nabla_I \langle \Psi_0 | \hat{\mathcal{H}} | \Psi_0 \rangle \\ \hat{\mathcal{H}} \Psi_0 &= E_0 \Psi_0 \end{aligned} \quad (2.15)$$

Equation (2.15) thus describes classical nuclei moving under the potential defined by the Born-Oppenheimer ground state energy $E_0(\{\mathbf{R}_I\})$. Due to combination of accuracy and efficiency, density functional theory (DFT) Kohn-Sham [Hohenberg and Kohn 1964, Kohn and Sham 1965] is the method of choice. The field of *ab initio* molecular dynamics is a very rapidly growing field, and it has definitely witnessed many leaps since the seminal paper by Car and Parrinello in 1985, where they unified the fields of molecular dynamics and electronic structure, presenting the “Car-Parrinello molecular dynamics (CPMD)”. In this section, after a quick presentation of the Kohn-Sham method, two related approaches to *ab initio* MD are presented: the “Gaussian and plane waves” (GPW) method [Lippert et al. 1997], and its augmented extension, the “Gaussian and augmented plane waves” (GAPW) method [Lippert et al. 1999]. Both methods are implemented in Quickstep, which is part of the CP2K code [VandeVondele et al. 2005]. Unlike the CPMD method, which is based on an extended-Lagrangian formulation to propagate the nuclear coordinates *and* the electronic wavefunction *simultaneously*, Quickstep performs Born-Oppenheimer Molecular Dynamics (BOMD) by optimizing the electronic wavefunction in each MD time step given the set of fixed nuclear coordinates. Thus in CP2K the atomic nuclei are propagated using classical mechanics with the electronic ground state energy providing the potential energy surface. Because of a density matrix extrapolation scheme, BOMD in Quickstep is highly efficient, requiring only a small number of wavefunction optimization iterations per MD step. In this section, all equations are written in atomic units.

The Kohn-Sham method

In the Kohn-Sham method, one starts with a system of N *non-interacting* electrons in a local potential $V_s(\mathbf{r})$. For such an independent particle model the wavefunction can always be written as an antisymmetrized product of orthonormal orbitals ($\phi_i(\mathbf{r})$) *i.e.* a Slater determinant, with an electron density $n(\mathbf{r})$:

$$n(\mathbf{r}) = \sum_i |\phi_i(\mathbf{r})|^2 \quad (2.16)$$

with the orbitals being the solutions of one-particle Schrödinger equations:

$$\left(\frac{1}{2} \nabla^2 + V_s(\mathbf{r}) \right) \phi_i(\mathbf{r}) = \epsilon_i \phi_i(\mathbf{r}) \quad (2.17)$$

If one requires now that the local potential $V_s(\mathbf{r})$ reproduces exactly the density of the (molecular) system of interest, then application of the Hohenberg-Kohn theorems results in explicit

expressions for the potential and the total energy [VandeVondele et al. 2006]. The total Kohn-Sham electronic energy, a functional of the electron density, is split into the following contributions:

$$E^{\text{el}}[n(\mathbf{r})] = E_s^{\text{T}}[n(\mathbf{r})] + E^{\text{V}}[n(\mathbf{r})] + E^{\text{H}}[n(\mathbf{r})] + E^{\text{XC}}[n(\mathbf{r})] \quad (2.18)$$

where the successive terms are respectively: the electronic kinetic energy of the non-interacting electrons, the interaction energy with the external potential provided by the atomic nuclei, the electronic Hartree energy, and the exchange-correlation energy. The last term contains all the contributions from electron exchange and correlation in addition to self-interaction correction and correction to the non-interacting kinetic energy [Koch and Holthausen 2000]. Of course one always adds the coulomb interaction between the atomic nuclei to get the total Born-Oppenheimer energy of the molecule.

The Kohn-Sham potential is defined by:

$$V_s(\mathbf{r}) = V^{\text{V}} + V^{\text{H}} + V^{\text{XC}} \quad (2.19)$$

where the terms are respectively: the external potential, the Hartree potentials, and the exchange correlation potential which is the functional derivative of $E^{\text{XC}}[n(\mathbf{r})]$:

$$V^{\text{XC}} = \frac{\delta E^{\text{XC}}[n(\mathbf{r})]}{\delta n(\mathbf{r})} \quad (2.20)$$

Knowledge of eq. (2.20) amounts to exact knowledge of how the energy of the many particle systems depends on the electron density, and one could find the exact ground state energy and electron density by solving the Kohn-Sham equations for independent particles eq. (2.17) [Martin 2004]. In Density Functional Approximations (DFA), one tries to approximate the yet-unknown exchange correlation potential by various approximations. The hierarchy of approximations that has been developed so far, ranging from simple local approximations based on the homogeneous electron gas to rather sophisticated functionals incorporating *e.g.* sums over the unoccupied orbitals, has been described as a Jacob's ladder of successive rungs (approximations) climbing up to the "heaven of chemical accuracy" [Perdew and Schmidt 2001].

The GPW and GAPW methods

In the GPW approach a dual representation is used for the electron density. This dual representation allows for an efficient treatment of the electrostatic interactions and allows for a scheme for the calculation of the total energy and the Kohn-Sham matrix that scales linearly with the system size [VandeVondele et al. 2005].

The Kohn-Sham orbitals are represented using atom-centered Gaussian functions³:

$$n(\mathbf{r}) = \sum_{\mu\nu} \mathbf{P}^{\mu\nu} \phi_{\mu}(\mathbf{r}) \phi_{\nu}(\mathbf{r}) \quad (2.21)$$

where $\mathbf{P}^{\mu\nu}$ is the density matrix, and the functions $\phi_{\mu}(\mathbf{r})$ are the familiar contracted Gaussian basis functions. In addition to eq. (2.21), the density is also expanded in an auxiliary basis set

³In this section we follow the original presentation given by VandeVondele et al. [2005]

of plane waves:

$$\tilde{n}(\mathbf{r}) = \frac{1}{\Omega} \sum_{|\mathbf{G}| < G_C} \tilde{n}(\mathbf{G}) e^{i\mathbf{G} \cdot \mathbf{r}} \quad (2.22)$$

where Ω is the volume of the periodic cell and $E_C = \frac{1}{2}G_C^2$ is the plane wave cutoff energy which determines the number of plane wave vectors in the reciprocal grid. The expansion coefficients $\tilde{n}(\mathbf{G})$ in eq. (2.22) are such that $\tilde{n}(\mathbf{r})$ is equal to $n(\mathbf{r})$ on a regular (*i.e.* real space) grid, which thus allows for a rapid conversion between $\tilde{n}(\mathbf{r})$, $n(\mathbf{r})$ and $\tilde{n}(\mathbf{G})$ using an efficient mapping procedure and fast Fourier transforms (FFT). This in turn gives latitude in computing the different contributions to the Kohn-Sham energy in an efficient way.

With this dual representation of the density, the Kohn-Sham DFT energy functional in the GPW scheme is given by:

$$\begin{aligned} E[n] &= E^T[n] + E^V[n] + E^H[n] + E^{XC}[n] + E^{II}[n] \\ &= \sum_{\mu\nu} \mathbf{P}^{\mu\nu} \langle \phi_\mu(\mathbf{r}) | -\frac{1}{2} \nabla^2 | \phi_\nu(\mathbf{r}) \rangle \\ &\quad + \sum_{\mu\nu} \mathbf{P}^{\mu\nu} \langle \phi_\mu(\mathbf{r}) | V_{loc}^{PP}(\mathbf{r}) | \phi_\nu(\mathbf{r}) \rangle + \sum_{\mu\nu} \mathbf{P}^{\mu\nu} \langle \phi_\mu(\mathbf{r}) | V_{nl}^{PP}(\mathbf{r}, \mathbf{r}') | \phi_\nu(\mathbf{r}') \rangle \\ &\quad + 2\pi\Omega \sum_{|\mathbf{G}| < G_C} \frac{\tilde{n}^*(\mathbf{G})\tilde{n}(\mathbf{G})}{\mathbf{G}^2} + \int e^{xc}(\mathbf{r}) d\mathbf{r} + \sum_{A < B} \frac{Z_A Z_B}{|R_A - R_B|} \end{aligned} \quad (2.23)$$

where $E^T[n]$ is the electronic kinetic energy, $E^V[n]$ is the electronic interaction with the ionic cores, described by norm-conserving pseudopotentials that is split into a local and a non-local part, $E^H[n]$ is the Hartree energy, $E^{XC}[n]$ the exchange correlation energy, and $E^{II}[n]$ is the electrostatic interaction of the ionic cores. The kinetic energy term in eq. (2.23) is identical to the one used in standard atom-centered-orbital-based DFT and is computed in real space. The auxiliary expansion of the atomic all-electron density in terms of plane waves would be computationally very inefficient, so the well-established technique using pseudopotentials is used here (The second and third terms in eq. (2.23)). In Quickstep the pseudopotentials of Goedecker, Teter, and Hutter (GTH) are used [Goedecker et al. 1996, Hartwigsen et al. 1998]. The electrostatic contributions in eq. (2.23) are treated using the Ewald sum method [Ewald 1921] (The Hartree energy, the local pseudopotential terms, the electrostatic interaction of the ionic cores). The exchange correlation energy and potential are both represented discretely on the real-space grid. This discrete representation, though it permits a highly efficient calculation of the terms, lead to some numerical difficulties in regions of vanishing density, in particular (with such a pseudopotential-based approach) in the core region. This problem is overcome by performing the integration in real-space on a locally-averaged density employing a smoothing operator. This issue however is fundamentally resolved in the all-electron GAPW scheme.

Parallel to the evaluation of the energy, the calculation of the Kohn-Sham matrix elements is divided into two-halves. The matrix elements of the kinetic energy and the pseudopotential are integrated analytically using recursion relations, and the matrix elements of the Hartree and exchange correlation potential are calculated efficiently by switching between real-space and reciprocal-space representations on the FFT grid [Lippert et al. 1999].

In the GAPW approach [Lippert et al. 1999], the auxiliary representation of the density is switched from a pure plane wave to a Gaussian-augmented-plane waves one. This does not only allow for using a much smaller number of FFT grid points to obtain converged results, but it also avoids some of the numerical difficulties associated with calculating the exchange-

correlation energy, and more importantly – since we have particular interest in magnetic resonance parameters – it allows for an all-electron representation.

Once the energy is computed using either the GPW or the GAPW scheme, the forces on the ions can be evaluated by explicitly computing the gradient of the energy with respect to atomic positions.

2.2 Magnetic Resonance Spectroscopy

2.2.1 Basic Theory of Magnetic Resonance

The basic magnetic resonance experiment in NMR and EPR is essentially the same. The Hamiltonian giving the interaction energy between a static magnetic field \mathbf{B}_0 and an “entity” with magnetic moment $\hat{\boldsymbol{\mu}}$ is given by:

$$\hat{\mathcal{H}} = -\hat{\boldsymbol{\mu}} \cdot \mathbf{B}_0 \quad (2.24)$$

For a free nucleus with a dimensionless spin operator $\hat{\mathbf{I}}$:

$$\hat{\boldsymbol{\mu}} = \gamma \hbar \hat{\mathbf{I}} = g_N \mu_N \hat{\mathbf{I}} \quad (2.25)$$

while for a free electron with spin $\hat{\mathbf{S}}$:

$$\hat{\boldsymbol{\mu}} = g_e \mu_B \hat{\mathbf{S}} \quad (2.26)$$

where γ is the gyromagnetic ratio specific for the nucleus, g_N is a dimensionless constant, the nuclear g-factor, μ_N is the nuclear magneton which is equal to $e\hbar/2m_p$ with e the proton charge and m_p the proton rest mass, g_e is the free electron g-value ≈ 2.002319 , and μ_B is the Bohr magneton $e\hbar/2m$ with m the electron rest mass.

Employing the usual convention that \mathbf{B}_0 is along the z -axis:

$$\hat{\mathcal{H}} = -g\mu|\mathbf{B}_0|\hat{I}_z \quad (2.27)$$

The eigenvalues of eq. (2.27) take a simple form, being only multiples of m_z , the eigenvalues of \hat{I}_z and \hat{S}_z :

$$E = -g\mu|\mathbf{B}_0|m_z \quad (2.28)$$

In eqs. (2.27) and (2.28) the subscripts of g and μ has been dropped to denote a general (NMR or EPR) expression, and \hat{I}_z is also used in the same sense. It is clear that the degeneracy of different eigenstates of \hat{I}_z and \hat{S}_z is lifted, with a splitting that depends linearly on $|\mathbf{B}_0|$. This “Zeeman” splitting of the different $|m_S\rangle$ levels is depicted in fig. 2.1.

In magnetic resonance spectroscopy, the most common experimental setup to detect transitions between the manifold in fig. 2.1 is an alternating magnetic field applied perpendicular to the static field, conventionally defining the x -axis. From the matrix elements of \hat{I}_x , which vanish unless $\Delta m_z = \pm 1$, we get the resonance condition:

$$\begin{aligned} \hbar\omega &= g_N \mu_N |\mathbf{B}_0| = \gamma \hbar |\mathbf{B}_0| & (\text{NMR}) \\ &= g_e \mu_B |\mathbf{B}_0| & (\text{EPR}) \end{aligned} \quad (2.29)$$

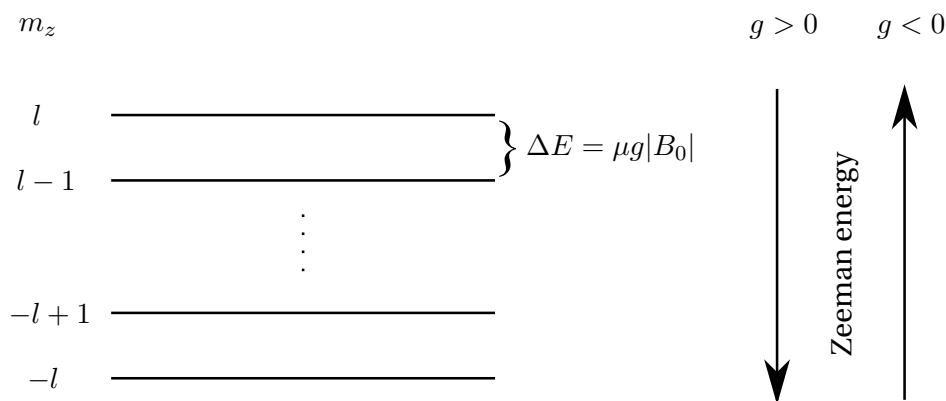


Figure 2.1: The Zeeman splitting of energy levels due to a static field B_0 along the z -axis.

If eq. (2.24) were the only spin-related term in the Hamiltonian, magnetic resonance would have been extremely boring and dull. As will be discussed in more detail in the next sections, there is a large number of other interactions that give a very rich structure to the spectrum. The outcome of these interactions is that different spins experience resonance at different frequencies (effectively as if they acquire different – possibly anisotropic – g -factors). Thus the single resonance peak that would be predicted from eq. (2.24) is split into a multitude of peaks, giving invaluable insight about the local chemical environments around the different spins in the sample. These individual peaks are additionally split due to interactions with neighboring spins. Moreover, many of these interactions are anisotropic – they depend on the orientation of the sample relative to B_0 , which is reflected in the spectrum unless the internal motion of the spin in the sample is fast enough to average out these anisotropies.

Another factor that clearly stands out in magnetic resonance spectroscopy is saturation and relaxation effects. Especially in NMR spectroscopy where typical relaxation times amount to milliseconds or longer, which means that saturation is much more prone to happen. Such long relaxation times do not only allow complex manipulations of the spins in the time domain of their evolution, but also leaves its signature on the spectral lineshape, which provides invaluable insights about the dynamics of the system, and provides the basis for some of the most interesting applications of magnetic resonance spectroscopy [Callaghan 2011].

2.2.2 The Empirical Spin Hamiltonian

The richness of detail in magnetic resonance spectra brought about by the spin interactions with other spins and with the surrounding lattice, motivated the development of a tool to facilitate the summarizing and interpretation of the information in the spectrum, which was achieved by the introduction of the spin Hamiltonian in the 1950s. The spin Hamiltonian has been described as “a major intellectual achievement with far reaching consequences for the development of EPR and NMR spectroscopy” [Neese and Munzarova 2004]. This *phenomenological* or *empirical* spin Hamiltonian is an effective Hamiltonian that contains only spin operators and numerical parameters obtained by fitting to the experimental spectrum, and acting only on electron and nuclear spin functions. The spin Hamiltonian in a sense is the “last outpost of the experimentalist” [Griffith 1964], where experimental results are presented in a concise form ready for interpretation. In the case of EPR, it is not even necessary that the spin used in the spin Hamiltonian is the total spin of the system, but it can be conveniently regarded as “fictitious spin” chosen such that the spin multiplicity matches the number of

states of interest. As an example, the continuous-wave (cw) EPR spectrum of a system with one unpaired electron and n nuclei with non-zero spin can be adequately described by a spin Hamiltonian of the form:

$$\hat{\mathcal{H}}_S = \mu_B \mathbf{B}_0 \cdot \mathbf{g} \cdot \mathbf{S} + \sum_n \mathbf{S} \cdot \mathbf{A}_n \cdot \mathbf{I}_n - \mu_N \sum_n g_N^n \mathbf{B}_0 \cdot (1 - \sigma) \cdot \mathbf{I}_n + \sum_n \mathbf{I}_n \mathbf{Q}_n \mathbf{I}_n \quad (2.30)$$

Where the successive terms account for the Zeeman interaction between the electron spin \mathbf{S} and the applied magnetic field \mathbf{B}_0 , the hyperfine interaction between \mathbf{S} and the nuclear spins \mathbf{I}_n , the nuclear Zeeman interaction with the external field including the chemical shift σ , and the nuclear quadrupolar interaction for nuclei with $\mathbf{I} > \frac{1}{2}$. In case of NMR on an $S = 0$ system, the first two terms would vanish, while additional small terms that were ignored in eq. (2.30) would be taken into account e.g. a dipolar and a scalar coupling between the nuclear spins. In all cases the leading terms of the Spin Hamiltonian always occurs in bilinear form like in eq. (2.30):

$$\hat{\mathcal{H}}_S = \sum_{A,B} c_{A,B} \mathbf{v}^A \cdot \mathbf{T} \cdot \mathbf{v}^B \quad (2.31)$$

where $c_{A,B}$ is a constant scalar, \mathbf{v}^A is a vector operator (\mathbf{I} , \mathbf{S} , or \mathbf{B}), and \mathbf{T} is a 3×3 coupling matrix.

Since the spin Hamiltonian eigenvalue problem is far easier to solve than the full electronic Schrödinger equation, the experimentalist can focus on experimental design and interpretation [Neese and Munzarova 2004]. On the other hand the spin Hamiltonian reduces the task of theoretical work to computing its parameters, and thus serves as a common meeting ground between theory and experiment. Before outlining how an equation equivalent to eq. (2.30) can be obtained from first principles, the next section outlines the origin of the “small terms” in the Hamiltonian that lead to magnetic splitting of energy levels, eventually giving rise to eq. (2.30).

2.2.3 The *ab initio* Spin Hamiltonian

The Origin of Magnetic Energy Levels

In this outline of the quantum-mechanical origin of magnetic energy levels, we adopt a semi-classical approach, where only the molecular system is described at a quantum mechanical level, while classical electrodynamics is used to describe the fields. In such an approach, the perturbing external field as well as the nuclear moments are not influenced by the molecular system, the so-called minimal coupling approximation [Sauer 2011, Harriman 1978, p. 5]. A full first-principles treatment of the interaction of molecules and fields would require quantum electrodynamics (QED). However, quantum electrodynamics is yet far too complicated to be regularly employed in the calculation of electromagnetic properties, and results of explicit QED calculations on atomic/molecular systems indicate that the effects are expected to be very small, especially for light elements [Beier et al. 2000].

The classically-inferred Hamiltonian

In order to account for the interaction of molecules with a static magnetic field, the first step would be to incorporate such a field in the Hamiltonian. Starting from the classical Hamil-

tonian for a particle with charge q and mass m in the presence of a field specified by the potentials ϕ and \mathbf{A} [Hinchliffe and Munn 1985, p. 160]:

$$H = \frac{1}{2m}(\mathbf{p} - q\mathbf{A})^2 + q\phi \quad (2.32)$$

One can easily setup a quantum mechanical Hamiltonian for a system of interacting particles⁴:

$$\hat{H} = \sum_i \frac{1}{2m_i} |\hat{\mathbf{p}}_i - q_i \mathbf{A}(\mathbf{r}_i)|^2 + \sum_i q_i \phi(\mathbf{r}_i) + \frac{1}{4\pi\epsilon_0} \sum_{i,j>i} \frac{q_i q_j}{r_{ij}} \quad (2.33)$$

Here, $\mathbf{p}(i)$ is the canonical momentum operator, ϕ and \mathbf{A} represent the scalar and vector potential respectively. Expanding the squared kinetic momentum, and employing the Coulomb gauge ($\nabla \cdot \mathbf{A} = 0$) eq. (2.33) becomes [McWeeny 1989, p. 362]:

$$\hat{H} = \hat{H}_0 + \sum_i q_i \phi(\mathbf{r}_i) - \sum_i \frac{q_i}{m_i} \mathbf{A}(\mathbf{r}_i) \cdot \hat{\mathbf{p}}_i + \sum_i \frac{q_i^2}{2m_i} A^2(i) \quad (2.34)$$

Where \hat{H}_0 is the field-free Hamiltonian:

$$\hat{H}_0 = \sum_i \frac{\hat{\mathbf{p}}_i^2}{2m_i} + \frac{1}{4\pi\epsilon_0} \sum_{i,j>i} \frac{q_i q_j}{r_{ij}} \quad (2.35)$$

Two points are in order here. First, if we were to employ the Born-Oppenheimer approximation to perform a fixed-nuclei calculation using eq. (2.34), we should keep in mind that the separation of internal motion from translational motion of the molecule as a whole is not valid here. Charged particles experience forces when translated through a field, and thus translations would affect the internal dynamics of the system. However, with weak fields and neutral molecules moving at thermal velocities, these effects are very small and are nearly always neglected [McWeeny 1989, p. 362]. The second point is that the classically-inferred Hamiltonian operator eq. (2.34) is incomplete. Since it was derived from a nonrelativistic classical Hamiltonian eq. (2.32), it disregards any relativistic field considerations (e.g. retarded potentials) [McWeeny 1989, p. 367], and it totally omits spin and its associated magnetic moment, which has no classical analogue anyway and hence cannot be derived in the usual manner with the correspondance principle [Shankar 1994, p. 122]. A relativistic treatment would remedy these omissions. Nevertheless, one can still “attach” spin-related terms to the Hamiltonian in a purely phenomenological manner, in essentially the same spirit as the Pauli method accounts for electron spin in nonrelativistic quantum mechanics by postulating an additional degree of freedom. Once the spin and its associated magnetic moment are postulated, one can go on and add magnetic interaction terms to eq. (2.34) by analogy with classical theory [Harriman 1978, p. 38] e.g. a term $-\boldsymbol{\mu} \cdot \mathbf{B}$ accounting for a spin magnetic moment $\boldsymbol{\mu}$ interacting with the external magnetic field \mathbf{B} , while the corresponding vector potential \mathbf{A} will give a dipole term . . . etc (see for example [Kutzelnigg 2004]). Besides the aesthetic objection to such an *ad hoc* approach, a very practical problem is that one can never be sure that all the relevant terms have been “patched up” to the Hamiltonian, and – as mentioned before – the correspondance principle offers no help here since there is no classical counterpart to spin [Harriman 1978, p. 38], [Moss 1973, p. ix].

⁴SI units are used in this section

Origin of the “small terms” in the Hamiltonian

Dirac was the first to attempt reconciling quantum mechanics with the requirements of the special theory of relativity [Dirac 1928]. Starting from the classical relativistic Hamiltonian for a free particle, and – to avoid difficulties in interpreting the square root in the Lorentz-invariant Hamiltonian – introducing two linear factors $\alpha = (\alpha_x, \alpha_y, \alpha_z)$ and β , chosen such that they factorize the Hamiltonian, Dirac ended up with a Schrödinger-like equation for the electron, *the Dirac equation*:

$$i\hbar \frac{\partial \psi}{\partial t} = (c \boldsymbol{\alpha} \cdot [\mathbf{p} - q\mathbf{A}] + q\phi + \beta mc^2) \psi \quad (2.36)$$

For consistency, it turns out that the factors α and β , in analogy to the Pauli matrices, should follow the following anticommutation relation:

$$[\alpha_\mu, \alpha_\nu]_+ = 2\delta_{\mu\nu} \quad (2.37)$$

where the indices μ and ν run over all the four factors $(\alpha_x, \alpha_y, \alpha_z, \beta)$. Since we now have four factors, it is not possible to find a two-dimensional representation as in the case of the three Pauli matrices in the nonrelativistic treatment [McWeeny 2004, p. 48]. A four-dimensional representation is required here, which means that unlike the Pauli method where one ends up with a *two-component spinor*, the wavefunction in eq. (2.36) is a *four-component spinor*. In the simplest representation⁵, the factors α and β take the form:

$$\alpha_\mu = \begin{pmatrix} \mathbf{0}_2 & \boldsymbol{\sigma}_\mu \\ \boldsymbol{\sigma}_\mu & -\mathbf{0}_2 \end{pmatrix}, \quad \beta = \begin{pmatrix} \mathbf{I}_2 & \mathbf{0}_2 \\ \mathbf{0}_2 & -\mathbf{I}_2 \end{pmatrix} \quad (2.38)$$

where the $\boldsymbol{\sigma}_\mu$ are the Pauli spin matrices and \mathbf{I}_2 , $\mathbf{0}_2$ are the two-dimensional unit and zero matrices.

The Dirac equation can be solved exactly in a few cases, including the free electron in a uniform magnetic field, and the Coulomb field (e.g. the hydrogen-like atom in the limit of infinite nuclear mass) [Harriman 1978, pp. 20–36]. In these solutions we find that the equation naturally gives an intrinsic angular momentum, and an associated magnetic moment with the correct proportionality constant that is twice the gyromagnetic ratio associated with orbital angular momentum (the free electron g -value = 2.0).⁶ Both magnetic moments (spin and orbital) interact with a magnetic field and interact with each other. Thus, by satisfying the requirements of special relativity and those of quantum mechanics, we end up with Equation eq. (2.36) which accounts for the basic electron spin resonance (ESR) phenomenon – including the hyperfine interaction – without any additional postulates.

Given the success of the Pauli method in nonrelativistic quantum mechanics, one is tempted to think that in the non-relativistic-limit, it is possible to project eq. (2.36) onto a two-dimensional representation. Indeed, several methods do exist to accomplish this task (e.g. Harriman 1978 Chapter 1, Moss 1973 Chapter 8, van Lenthe et al. 1993; 1994)

An exact relativistic many-electron Hamiltonian is not available, thus if one wants to avoid the formidable complications of QED, extending the Dirac equation to the many-electron case always involves approximate Hamiltonians [Kutzelnigg 2004, p. 55]. Breit generalized

⁵In fact several representations are possible, but any other representation can be shown to be a trivial extension of the 4×4 matrix representation, see Harriman 1978, p. 18.

⁶QED corrections give $g \approx 2.002319$

the Dirac equation to two particles, taking account of magnetic and retardation effects to order v^2/c^2 [Breit 1929; 1932]. For the many electron case, it is customary to simply assume pairwise-additivity of the interactions. Such a relativistic many-electron Hamiltonian can then be reduced to a Pauli form, but now the terms in the spinless nonrelativistic Hamiltonian are only the leading terms, with a large number of “small terms” (including the classically-expected terms) that are usually collected in a perturbation Hamiltonian H' [McWeeny 1989, p. 367]. In a fixed-nuclei approximation, the more important terms in H' are now given⁷, assuming a uniform magnetic field and the absence of external electric fields ($\phi = 0$, $\mathbf{A} = \frac{1}{2}\mathbf{B} \times \mathbf{r}$): [McWeeny 1989, p. 369]

$$\hat{H}' = \hat{H}_{mag} + \hat{H}_{SL} + \hat{H}_{SS} + \hat{H}_Z + \hat{H}_N \quad (2.39)$$

where:

- \hat{H}_{mag} Terms arising from an external magnetic field interacting with orbital magnetic moment.
- \hat{H}_{SL} Spin-Orbit interaction terms.
- \hat{H}_{SS} Electron spin-spin interaction terms.
- \hat{H}_Z Electron Zeeman interaction.
- \hat{H}_N Nuclear “hyperfine” terms.

1. \hat{H}_{mag}

$$\begin{aligned} \hat{H}_{mag} &= \mu_B \sum_i \mathbf{B} \cdot \mathbf{L}_i + \frac{e^2}{8m} \sum_i (\mathbf{B} \times \mathbf{r}_i)^2 \\ &= \hat{H}_{para} + \hat{H}_{dia} \end{aligned} \quad (2.40)$$

Where $\mu_B = e\hbar/2m$ (the Bohr magneton). The first term, sometimes called the “orbital Zeeman term”. gives the orbital paramagnetism in systems with non-quenched orbital angular momentum (e.g. free atoms in non S-states), this term also contributes to diamagnetism in second order. The main contribution to diamagnetism comes from the second term \hat{H}_{dia} .

2. \hat{H}_{SL}

$$\hat{H}_{SL} = \frac{g\mu_B^2}{4\pi\epsilon_0 c^2} \left[\sum_{n,i} \frac{Z_n \mathbf{S}_i \cdot \mathbf{M}_i^n}{r_{nl}^3} - \sum_{i,j \neq i} \frac{2\mathbf{S}_i \cdot \mathbf{M}_j^i + \mathbf{S}_i \cdot \mathbf{M}_i^j}{r_{ij}^3} \right] \quad (2.41)$$

Where $\boldsymbol{\pi}_i = \hat{\mathbf{p}}_i - q_i \mathbf{A}(\mathbf{r}_i)$, and the gauge-invariant angular momentum $\hbar \mathbf{M}_q^p = \mathbf{r}_{pq} \times \boldsymbol{\pi}_q$ is associated with the angular momentum of a particle at q about point p [McWeeny 1989, p. 370] and the index n runs over the nuclei. These terms give the spin-orbit interaction due to motion in the electric field of the nucleus (first term) and the electrons (second term, comprising the spin-other-orbit and spin-orbit terms) [Moss 1973, pp. 177,182].

3. \hat{H}_Z

$$\hat{H}_Z = g\mu_B \sum_i \mathbf{B} \cdot \mathbf{S}_i - \sum_i \frac{g\mu_B}{2m^2 c^2} (\mathbf{B} \cdot \mathbf{S}_i) \pi_i^2 \quad (2.42)$$

Gives the orbitally-independent Zeeman term arising from interaction of an electron's

⁷Following [McWeeny 1989]. For a more comprehensive listing of the small terms in the Hamiltonian, see [Harriman 1978, Appendix F]

spin magnetic moment with the external magnetic field. The second term is a relativistic mass correction.

4. \hat{H}_{SS}

$$\hat{H}_{SS} = -\frac{g^2 \mu_B^2}{8\pi \epsilon_0 c^2} \sum_{i,j \neq i} \left[\frac{3(\mathbf{S}_i \cdot \mathbf{r}_{ij})(\mathbf{S}_j \cdot \mathbf{r}_{ij}) - r_{ij}^2 \mathbf{S}_i \cdot \mathbf{S}_j}{r_{ij}^5} + \frac{8\pi}{3} \delta(\mathbf{r}_{ij}) \mathbf{S}_i \cdot \mathbf{S}_j \right] \quad (2.43)$$

This term arises from magnetic dipole–dipole interactions between pairs of electrons. The term with the delta function is the contact term. It can be shown that this contact term does not lead to any spin-dependence of energy, it is thus of little interest in NMR and EPR spectroscopy [McWeeny 1989, p. 370].

5. \hat{H}_N

$$\begin{aligned} \hat{H}_N &= -\mu_n \sum_n g_n \mathbf{B} \cdot \mathbf{I}_n + \frac{2\mu_n \mu_n}{4\pi \epsilon_0 c^2} \sum_{n,i} \frac{g_n \mathbf{I}_n \cdot \mathbf{M}_i^n}{r_{ni}^3} \\ &+ \frac{g \mu_B \mu_n}{4\pi \epsilon_0 c^2} \sum_{n,i} g_n \left(\frac{3(\mathbf{S}_i \cdot \mathbf{r}_{ni})(\mathbf{I}_n \cdot \mathbf{r}_{ni}) - r_{ni}^2 \mathbf{I}_n \cdot \mathbf{S}_i}{r_{ni}^5} + \frac{8\pi}{3} \delta(\mathbf{r}_{ni}) \mathbf{I}_n \cdot \mathbf{S}_i \right) \\ &- \frac{\mu_n^2}{8\pi \epsilon_0 c^2} \sum_{n,n' \neq n} g_n g_{n'} \frac{3(\mathbf{I}_n \cdot \mathbf{r}_{nn'})(\mathbf{I}_{n'} \cdot \mathbf{r}_{nn'}) - r_{nn'}^2 \mathbf{I}_n \cdot \mathbf{I}_{n'}}{r_{nn'}^5} \\ &= \hat{H}_{NZ} + \hat{H}_{Nmag} + (\hat{H}_N^{dip} + \hat{H}_N^{contact}) + \hat{H}_{NN} \end{aligned} \quad (2.44)$$

This term gives all the nuclear hyperfine terms in the order: the nuclear Zeeman term, nuclear dipolar interaction with electronic orbital motion, electron-nuclear dipole-dipole interaction including the contact correction, and nuclear-nuclear dipole-dipole interaction.

Other terms may also be added to account for nuclear quadrupole moments, the latter however would require treating the nucleus as a structured particle.

The *ab initio* effective spin Hamiltonian: A sum-over-states approach

As mentioned in section 2.2.2, experimental magnetic resonance spectra are summarized in the form of an effective spin Hamiltonian with a relatively small number of parameters. In order to exploit the full potential of magnetic resonance as a tool to probe and understand atomic and molecular systems, one requires a careful interpretation of the connection between the empirical spin Hamiltonian parameters and the electronic structure or electron density [McWeeny 2004, p. 65]. The goal of this section is to show how one can relate the *ab initio* Hamiltonian, including the small terms listed before, to the effective spin Hamiltonian obtained by fitting to experimental results. In fact, the approach presented here provides a rigorous basis for the whole concept of the spin Hamiltonian. Historically, the sum-over-states (SOS) approach that is presented here was the “cornerstone of EPR and NMR theory” for a long time [Neese 2007] in the form of Ramsey’s theory of NMR parameters and the theory developed by Abragam and Pryce for the EPR spin Hamiltonian [Abragam and Bleaney 1970]. The latter was however formulated in terms of ligand field theory (which is the form still presented in most EPR books). The general formulation presented here was first given by McWeeny [McWeeny 1965] based on the idea of effective Hamiltonians due to Löwdin and McWeeny himself [Löwdin 1959; 1963, McWeeny 1959]. According to Neese and Munzarova, “this rigorous and convenient approach remains, perhaps, unsurpassed today” [Neese and

[Munzarova 2004](#)]. This was also the approach [Harriman](#) chose to present in his monograph on ESR [[Harriman 1978](#), p. 164].

We start with the partitioned Hamiltonian:

$$\hat{H} = \hat{H}_0 + \hat{H}' \quad (2.45)$$

Where the zero-order part, \hat{H}_0 , is assumed to be independent of external magnetic fields and spins, thus it includes the usual nonrelativistic field-free Hamiltonian in eq. (2.35), and possibly also spin and magnetic field-independent relativistic corrections. H' contains the “small terms” collected in eqs. (2.39) to (2.44). In magnetic resonance, one is generally probing the splittings between some – originally degenerate or near-degenerate – eigenstates of H_0 , whose degeneracy has been lifted by H' . It is useful at this point to partition the set of (possibly approximate) eigenstates of \hat{H}_0 ($\{\phi_K\}$) into two sets, A and B . The finite set A includes the degenerate states we are interested in and set B is the (infinite) set of remaining eigenstates of \hat{H}_0 :

$$\{\phi_K\} = \{\phi_1^A, \dots, \phi_n^A, \phi_1^B, \dots, \phi_n^B\} \quad (2.46)$$

$$\Psi = \sum_K c_K \phi_K = \sum_a c_a^A \phi_a^A + \sum_b c_b^B \phi_b^B \quad (2.47)$$

and $\{\phi_K\}$ is assumed to be orthonormal and complete for $n_B \rightarrow \infty$. We additionally assume that the functions $\{\phi_K\}$ are variationally determined eigenfunctions (or approximations) such that \mathbf{H}_0 is diagonal. In a matrix representation, a partitioning of the full set ($n_A + n_B$) of secular equations follows:

$$\begin{pmatrix} \mathbf{H}^{AA} & \mathbf{H}^{AB} \\ \mathbf{H}^{BA} & \mathbf{H}^{BB} \end{pmatrix} \begin{pmatrix} \mathbf{c}^A \\ \mathbf{c}^B \end{pmatrix} = E \begin{pmatrix} \mathbf{c}^A \\ \mathbf{c}^B \end{pmatrix} \quad (2.48)$$

Following this partitioning, it is trivial to show that one can write a totally equivalent smaller system of equations in the A -space [[Löwdin 1959](#)]:

$$\mathbf{H}_{\text{eff}} \mathbf{c}^A = E \mathbf{c}^A \quad (2.49)$$

where \mathbf{H}_{eff} is an $n_A \times n_A$ matrix representation of an effective Hamiltonian:

$$\mathbf{H}_{\text{eff}} = \mathbf{H}^{AA} + \mathbf{H}^{AB} (E \mathbf{1}^{BB} - \mathbf{H}^{BB})^{-1} \mathbf{H}^{BA} \quad (2.50)$$

So far, eq. (2.50) is exact and presents no simplifications. We simply managed to reduce the dimensions of the secular equation using a truncated basis A . The influence of the remainder set B is included in the additional terms in the effective Hamiltonian. Approximating the exact energy in eq. (2.50) by the zero-order energy, [Löwdin](#) showed how to iteratively obtain order-by-order approximations to the solution [[Löwdin 1951; 1959](#)]. Writing down the perturbation in the form: $\hat{H}' = \lambda \hat{H}^\lambda$, where the familiar perturbation parameter λ is used to separate different orders of the perturbation, the matrix elements of \mathbf{H}_{eff} are then found to be [[McWeeny 1989](#), p. 372–373]:

$$\langle \phi_a | \hat{H}_{\text{eff}} | \phi_{a'} \rangle = \delta_{aa'} E_a^{(0)} + \lambda \langle \phi_a | \hat{H}^\lambda | \phi_{a'} \rangle + \lambda^2 \sum_b \frac{\langle \phi_a | \hat{H}^\lambda | \phi_b \rangle \langle \phi_b | \hat{H}^\lambda | \phi_{a'} \rangle}{E_a^{(0)} - E_b^{(0)}} + \dots, \quad (2.51)$$

which is correct up to second order in λ . Assuming that the A set functions are the correct zeroth order functions, the perturbed functions to first order take the form:

$$\tilde{\phi}_a^{(\lambda)} = \phi_a + \lambda \sum_b \frac{\phi_b \langle b | \hat{H}^\lambda | a \rangle}{E_a^{(0)} - E_b^{(0)}} = \phi_a + \lambda \phi_a^\lambda \quad (2.52)$$

where $\tilde{\phi}_a^{(\lambda)}$ refers to a first order perturbed wavefunction. One can discard the first term in eq. (2.51), implying that energies are relative to that of the unresolved A states. In this way, the last two terms in eq. (2.51) respectively give the first and second order splitting due to \hat{H}' . This result looks exactly like the familiar Rayleigh-Schrödinger perturbation energy expression, eq. (2.51) however is more general as it does not require knowledge of exact unperturbed wavefunctions of \hat{H}_0 [Harriman 1978, p. 166; McWeeny 1989, p. 48].

Equation eq. (2.51) can also be written in terms of the first order perturbed A -states eq. (2.52). The second order term takes the form:

$$\langle \phi_a | \hat{H}_{\text{eff}} | \phi_{a'} \rangle^{\lambda\lambda} = \frac{1}{2} \langle \tilde{\phi}_a^{(\lambda)} | \hat{H}^\lambda | \tilde{\phi}_{a'}^{(\lambda)} \rangle^{\lambda\lambda} \quad (2.53)$$

Equation eq. (2.53) provides physical insight into the results. The matrix elements of the *effective* Hamiltonian (which is a convenient mathematical object set up to yield energies correct to second order) are replaced by those of the *actual* Hamiltonian with respect to perturbed states [McWeeny 1989, p.375].

We can also extend these results to a double perturbation. Writing the perturbation Hamiltonian as:

$$\hat{H}' = \lambda \hat{H}^\lambda + \mu \hat{H}^\mu \quad (2.54)$$

Where again λ and μ are dummy parameters to keep track of the orders of the different terms, the first and second order parts of the effective Hamiltonian take the form:

$$\begin{aligned} \langle \phi_a | \hat{H}_{\text{eff}} | \phi_{a'} \rangle^{(1)} &= \lambda \langle \phi_a | \hat{H}^\lambda | \phi_{a'} \rangle + \mu \langle \phi_a | \hat{H}^\mu | \phi_{a'} \rangle \\ \langle \phi_a | \hat{H}_{\text{eff}} | \phi_{a'} \rangle^{(2)} &= \lambda^2 \sum_b \frac{\langle \phi_a | \hat{H}^\lambda | \phi_b \rangle \langle \phi_b | \hat{H}^\lambda | \phi_{a'} \rangle}{E_a^{(0)} - E_b^{(0)}} + \mu^2 \sum_b \frac{\langle \phi_a | \hat{H}^\mu | \phi_b \rangle \langle \phi_b | \hat{H}^\mu | \phi_{a'} \rangle}{E_a^{(0)} - E_b^{(0)}} \\ &\quad + \lambda\mu \sum_b \frac{\langle \phi_a | \hat{H}^\lambda | \phi_b \rangle \langle \phi_b | \hat{H}^\mu | \phi_{a'} \rangle}{E_a^{(0)} - E_b^{(0)}} + \mu\lambda \sum_b \frac{\langle \phi_a | \hat{H}^\mu | \phi_b \rangle \langle \phi_b | \hat{H}^\lambda | \phi_{a'} \rangle}{E_a^{(0)} - E_b^{(0)}} \end{aligned} \quad (2.56)$$

In first order, the double perturbation is simply additive, while in second order we have both “pure” terms, and “cross” terms that give rise to interesting interactions between the two perturbations (It is these cross terms that give rise to many of the EPR and NMR parameters). Both kinds of second order terms can also be expressed in terms of first order perturbed functions ($\tilde{\phi}_a^{(\lambda)}$ or $\tilde{\phi}_a^{(\mu)}$). We already know that the pure terms (λ^2, μ^2) give eq. (2.53), while the mixed terms together ($\lambda\mu$ and $\mu\lambda$) may be determined using the same “ λ -perturbed” functions but keeping only the $\mu \hat{H}^\mu$ term in \hat{H}' :

$$\langle \phi_a | \hat{H}_{\text{eff}} | \phi_{a'} \rangle^{\lambda\mu} = \langle \tilde{\phi}_a^{(\lambda)} | \mu \hat{H}^\mu | \tilde{\phi}_{a'}^{(\lambda)} \rangle^{\lambda\mu} \quad (2.57)$$

Or alternatively, if we choose to use the μ -perturbed functions:

$$\langle \phi_a | \hat{H}_{\text{eff}} | \phi_{a'} \rangle^{\lambda\mu} = \langle \tilde{\phi}_a^{(\mu)} | \lambda \hat{H}^\lambda | \tilde{\phi}_{a'}^{(\mu)} \rangle^{\lambda\mu} \quad (2.58)$$

and thus the cross-terms can in either case be computed as if the two perturbations were applied successively, by first computing the first-order wavefunctions from one perturbation, and then computing the matrix elements for the other [McWeeny 1989, p. 376]. Practically, this means that one has freedom to choose whichever of the two perturbations that is easier to handle in calculating the perturbed wavefunction.

One can now establish a connection to the phenomenological spin Hamiltonian. Via the partitioning method, the full secular problem can be contracted to smaller dimensions, which one can choose to coincide with the dimensions of the spin Hamiltonian secular equation. For a (fictitious) spin S and n nuclei each with spin I_n , the size of the A -set in eq. (2.48) would be $(2S + 1) \prod_n (2I_n + 1)$. One can then relate the matrix elements of the *exact and contracted* Hamiltonian to those of a *phenomenological* spin Hamiltonian. We look for operators $\hat{H}_S^{(1)}$ and $\hat{H}_S^{(2)}$ containing only spin operators and numerical parameters, such that:

$$\langle \theta_a | \hat{H}_S^{(1)} | \theta_{a'} \rangle = \langle \phi_a | \hat{H}' | \phi_{a'} \rangle \quad (2.59)$$

$$\langle \theta_a | \hat{H}_S^{(2)} | \theta_{a'} \rangle = \sum_b \frac{\langle \phi_a | \hat{H}' | \phi_b \rangle \langle \phi_b | \hat{H}' | \phi_{a'} \rangle}{E_a^{(0)} - E_b^{(0)}} \quad (2.60)$$

where the states $|\theta_a\rangle$ are electron-nuclear spin states with a total number of states exactly like the the A -space. Now, the eigenvalues of the spin Hamiltonian:

$$\mathbf{H}_S \mathbf{c}^A = E \mathbf{c}^A \quad (2.61)$$

are numerically equivalent, to second order, to those of the full secular problem eq. (2.48). Using this approach, McWeeny showed the origin of the different terms of the spin Hamiltonian as depicted in fig. 2.2. Griffith [1960] showed how the equivalents in eq. (2.59) and eq. (2.60) can be obtained under rather general conditions, thus, replacing the spatial and spin operators on the right hand side of eqs. (2.59) and (2.60) by purely spin operators and parameters. McWeeny used the Wigner-Eckart theorem to construct operators satisfying eq. (2.59) and eq. (2.60) in his seminal paper on the origin of the spin Hamiltonian, where he made extensive use of reduced spin density matrices [McWeeny 1965; 2004].

Although this SOS approach provides a beautiful theoretical foundation for the concept of a spin Hamiltonian, it is of limited practical utility for the calculation of second order properties, since it is rarely possible to compute more than a few dozen terms from low-lying excited states [Neese 2007], although in this regard one has to mention Neese's spectroscopy oriented multireference configuration interaction (SORCI) approach and its application to EPR parameters [Neese 2004]. Another drawback of this approach is that it breaks down if the unperturbed state under consideration is orbitally degenerate (though near-degeneracies were considered in Harriman's presentation). In the next section an alternative approach is outlined.

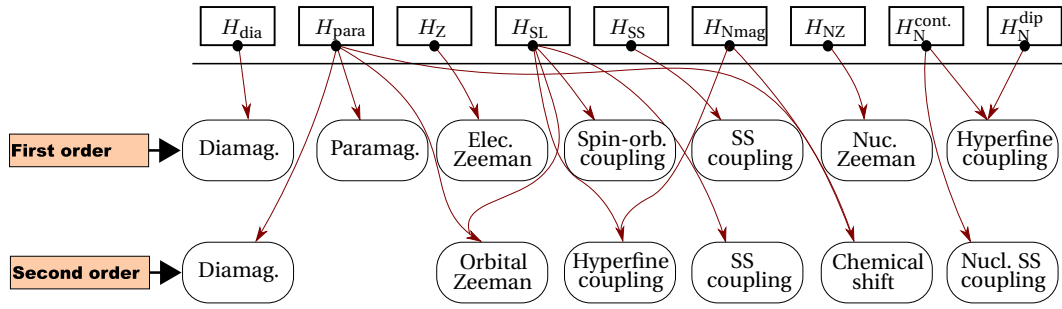


Figure 2.2: Origin of the different terms of the spin Hamiltonian. (Slightly modified from [McWeeny 2004])

Spin Hamiltonian parameters as energy derivatives

Since as already noted, the leading terms in the spin Hamiltonian occur in bilinear form (See eq. (2.31)), the spin Hamiltonian parameters can be computed as second partial derivatives (computed for example using the Hellmann-Feynman theorem) with respect to two perturbations [Neese 2007]. One can expand the total energy in a Taylor series truncated after the bilinear term:

$$\left. \frac{\partial^2 E}{\partial \lambda \partial \mu} \right|_{\lambda=\mu=0} \quad (2.62)$$

where – using the same symbols as in eq. (2.54) – λ and μ are the two perturbations (perturbing field or spin operators). One can then identify the relevant terms by comparing with the equivalent expansion of the spin Hamiltonian [Neese 2007]. In the following, the small terms of the Hamiltonian contributing to the g tensor, the NMR chemical shift, and the hyperfine coupling, will be given based on the definition of these parameters as energy derivatives. To put the expressions in as a simple form as possible, atomic units are used in this section.

Neese points out that all the second partial derivatives involving one-electron or effective one-electron (*e.g.* effective spin orbit) perturbing operators can be written in the general form [Neese 2007]:

$$\left. \frac{\partial^2 E}{\partial \lambda \partial \mu} \right|_{\lambda=\mu=0} = \sum_{\nu\delta} P_{\nu\delta}^{\pm} \langle \nu | \hat{h}_{\lambda\mu} | \delta \rangle + \sum_{\nu\delta} \frac{\partial P_{\nu\delta}^{\pm}}{\partial \lambda} \langle \nu | \hat{h}_{\mu} | \delta \rangle \quad (2.63)$$

where a set of basis functions $\{\phi_{\lambda}, \phi_{\delta} \dots\}$ has been introduced in which the orbitals are expanded. P^{\pm} represents a spin density matrix element, and the one electron operators $\hat{h}_{\lambda\mu}$ and \hat{h}_{μ} represent the second- and first derivative of the total Hamiltonian with respect to the perturbation. The two terms in eq. (2.63) replace the first- and second-order contributions in the SOS expansions in eq. (2.51) [Neese 2007]. This expression is rather general since the only place where the specific electronic structure method enters is in computing the density matrix. The latter can be the usual density matrix for variational electronic structure methods, or the “response densities” [Gauss and Cremer 1992] for non-variational methods *e.g.* Møller-Plesset perturbation theory and coupled-cluster.

The g tensor

For the g tensor, the pair of perturbation parameters is Cartesian components of the external magnetic field B_x and the net electron spin component S_y . Using the Hellmann-Feynman theorem for double perturbation theory [Declerck 2008]

$$g_{xy} = \frac{2}{\alpha} \frac{\partial}{\partial B_x} \langle \Psi_{B_x} | \frac{\partial H}{\partial S_y} | \Psi_{B_x} \rangle \Big|_{\mathbf{S}=0} \Big|_{\mathbf{B}=0} \quad (2.64)$$

where α is the fine structure constant ($\approx 1/137$ in atomic units) and Ψ_{B_x} is the wavefunction perturbed by a static magnetic field in the x -direction. Equation (2.64) means that we only need to compute the first order correction to the wavefunction for the three components of the magnetic field separately, and that for the perturbing terms we only need to consider terms linear in the electron spin operators and of zeroth or first order in the magnetic field [Declerck 2008]. By inspection of the small terms introduced in section 2.2.3 (eqs. (2.39) to (2.44)), one can identify four contributions to the g tensor [McWeeny 1989, Harriman 1978, Stone 1963, Angstl 1989]:

$$g_{xy} = g_e \delta_{xy} + \Delta g^{RMC} \delta_{xy} + \Delta g_{xy}^{GC} + \Delta g_{xy}^{OZ/SOC} \quad (2.65)$$

The first term is simply the free electron g value, and the second term is a relativistic mass correction to the Zeeman term [Angstl 1989]. Both terms were collected in the H_Z term eq. (2.42) and have the desired bilinear dependence on \mathbf{S} and \mathbf{B} , giving a first order contribution to the g matrix elements. The third term is a gauge correction term which is also first order (this would arise on substituting $\pi_q \rightarrow p_q - q\mathbf{A}$ in eq. (2.41)), and can be computed from the ground state spin density and the kinetic energy integrals [Neese 2001]:

$$\Delta g^{RMC} = -\frac{\alpha^2}{S} \sum_{\mu,\nu} \mathbf{P}_{\mu\nu}^{\alpha-\beta} \langle \varphi_\mu | \hat{T} | \varphi_\nu \rangle \quad (2.66)$$

The final term in eq. (2.65) is a second order one which in perturbation theory arises from a cross term between the orbital Zeeman term (H_{para}) and the spin-orbit coupling terms (c.f. eq. (2.60) and fig. 2.2). The second and third terms in eq. (2.65) are small and tend to cancel each other, and the more challenging second order term dominates the g tensor [Neese 2001].

Hyperfine coupling (The A tensor)

Again, the hyperfine coupling for a nucleus N is a mixed second partial derivative that can be computed by double perturbation theory [Declerck 2008]:

$$A_{xy}^N = \frac{\partial^2 E}{\partial I_x^N \partial S_y} \Big|_{\mathbf{I}^N=\mathbf{S}=0} \quad (2.67)$$

This time the perturbation is by the respective components of nuclear and electron spin. The same arguments hold like the case of the g tensor, and one can identify a first order contribution to the A tensor from the third term in eq. (2.44) (the Fermi contact term and the dipolar coupling) which can be computed simply as expectation values over the unperturbed wavefunction. In addition, there is a second order contribution involving the spin orbit coupling. The first order term is in most cases the dominant one.

The NMR shielding tensor

The NMR shielding at a nucleus N can also be expressed as a mixed second derivative of the energy in analogy to the g tensor, the only difference is replacing the electron spin component by a nuclear spin component I^N :

$$\sigma_{yx}^N = \left. \frac{\partial^2 E}{\partial B_x \partial I_y^N} \right|_{\mathbf{B}=\mathbf{I}^N=0} \quad (2.68)$$

And the shielding tensor can be identified as a second order property which in perturbation theory arises from a cross term between the orbital Zeeman term (\hat{H}_{para} in eq. (2.40)) and \hat{H}_{Nmag} (second term in eq. (2.44)).

It can be shown that eq. (2.68) leads to the familiar expression of the chemical shift tensor as the derivative of the induced magnetic field \mathbf{B}^{ind} at the position of the given nucleus \mathbf{r}_N with respect to the static external magnetic field \mathbf{B}^{ext} (see for example [Chesnut 1996](#)):

$$\sigma_{xy}^N = - \frac{\partial \mathbf{B}_x^{ind}(\mathbf{r}_N)}{\partial \mathbf{B}_y^{ext}} \quad (2.69)$$

where the induced field is given by [\[Sebastiani and Rothlisberger 2004\]](#):

$$\mathbf{B}^{ind}(\mathbf{r}) = \frac{1}{c} \int \frac{\mathbf{r} - \mathbf{r}'}{|\mathbf{r} - \mathbf{r}'|^3} \times \mathbf{j}(\mathbf{r}') d^3\mathbf{r}' \quad (2.70)$$

$$= -\frac{1}{c} \nabla \times \int \frac{\mathbf{j}(\mathbf{r}')}{|\mathbf{r} - \mathbf{r}'|} d^3\mathbf{r}' \quad (2.71)$$

and $\mathbf{j}(\mathbf{r})$ is the electronic current density. The problem of computing the chemical shielding tensor is thus reduced to calculating the induced current density $\mathbf{j}(\mathbf{r})$.

Chapter 3

Summary of the Published Papers

3.1 Solvation of Small Disulfonate Anions in Water/Methanol Mixtures Characterized by High-Field Pulse Electron Nuclear Double Resonance and Molecular Dynamics Simulations

In this work [Heller et al. 2010], which was done in collaboration with the Spiess research group from the Max Planck Institute for Polymer Research (MPIP), the solvation of Fremy's salt (FS, fig. 3.1) [Frémy 1845, Moser and Howie 1968] in binary solvent mixtures was investigated by means of EPR and pulse (Mims and Davies) orientation-selective electron nuclear double resonance (ENDOR) spectroscopy and molecular dynamics (MD) simulations. Though much of modern EPR is performed on frozen glasses, and nitroxide spin labels are very popular in EPR [Jeschke 2013], yet the effect of the nitroxide solvation is only rarely discussed. In this study, FS was chosen as a simple model ion to investigate its solvation in binary water-organic solvent mixtures. The importance of this investigation however far transcends the interests of the EPR community, as the understanding of ion solvation in multicomponent systems and "preferential solvation" phenomena is crucial for all branches of chemistry, from organic and inorganic chemistry, to electrochemistry, biochemistry, and even physiology [Reichardt and Welton 2011, Bagotsky 2005, Marcus 2002]. The term "preferential solvation" refers to the situation in mixed solvents where the solute may interact specifically with one solvent species, thus changing the composition of solvation shell from that of the bulk [Marcus 2002]. The chosen solvent mixture, methanol-water, represents the simplest case of a hydro-alcoholic mixture. Though the hydrophobic part of methanol molecules, the methyl group, is the smallest hydrocarbon chain possible, yet experimental evidence strongly indicates the existence of small scale structural inhomogeneities in water/methanol mixtures [Dixit et al. 2002, Guo et al. 2003, Lin et al. 2012, Asenbaum et al. 2012, Corsaro et al. 2013].

Field-swept echo-detected EPR in the W-band (~ 94.5 GHz) were performed on the frozen glass at 20 K. At the W-band, the increase in the Zeeman energy leads to higher resolution in the solid-state EPR spectrum, which enabled resolving the g-tensor principal values, and hence, specific turning points in the spectrum could be used to select certain orientations of FS with respect to the magnetic field. The so-called "orientation selection" technique uses these magnetic field positions at the turning points to obtain *single-crystal-like* ENDOR spectra. From orientation-selective ENDOR, hyperfine coupling tensors were elucidated with respect to the g-tensor principal axes. For nitroxides, the commonly used axes system is depicted in fig. 3.1. By using different mixtures of methanol-water where either the exchange-

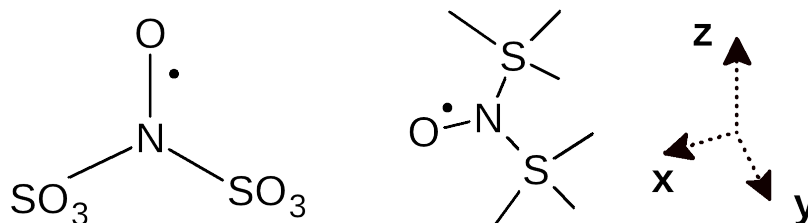


Figure 3.1: Fremy's salt (FS). The commonly used reference axes system is depicted on the right side.

able or non-exchangeable protons were deuterated, detailed information about the solvation shell could be extracted. Specifically, exchangeable protons were found to be distributed nearly isotropically, forming a hydrogen-bonded network around the sulfonate groups, while the non-exchangeable (methyl) protons were found more prominently along the molecular z-axis (perpendicular to the approximate plane spanned by ON(S)₂). Using a point-dipole approximation of the hyperfine coupling, the latter protons are found at an average distance of 3.5 Å from the electron.

The contribution of the author of this thesis to the work comprised the parametrization of force field parameters for FS by fitting to the DFT potential energy surface. Based on the obtained force field parameters, classical MD simulations were performed on FS in 50:50 methanol-water solvent at 300 K. The low-temperature solvation configurations corresponding to the experimental situation were obtained by repeatedly annealing snapshots (200 in total) which were extracted from the 300 K trajectory at regular intervals.

Analysis of the trajectory revealed not only very good agreement with experiment regarding the average geometry of FS, and the absence of ion-pairing with the counter-ions in solution, but also very good agreement with the solvent distribution revealed by pulse ENDOR results. This was demonstrated by computing the spatial distribution function of the solvent protons around FS (fig. 3.3), their angular distribution, and the coordination numbers of different FS oxygen atoms. In fact, the molecular picture of the solvation around FS which is derived from the MD simulations, is in full agreement with ENDOR results. Both exchangeable species (water and hydroxyl protons) are able to establish hydrogen bonds to FS with an angular distribution that reflects the sterical hindrance of the NO hydrogen-bond acceptor site by the sulfonate groups. Hence, exchangeable protons come in closest contact with the NO moiety along the molecular y-axis of the probe molecule. If the methanol-OH group (instead of water) is hydrogen bonded to the sulfonate groups, it is energetically favorable to not place the methyl group at the sulfonate group, as this would disturb the existing H-bond network and reduce the number of H-bonds. It is thus favorable to place the methyl groups on the “top” and “bottom” of the (approximate) plane spanned by O-N-(S)₂. Also, the largest “free” space for the methyl groups is given at these positions of the molecule due to the sulfonate groups. Thus, the preferential arrangement of methyl groups along the molecular z-direction of the nitroxide can be explained by the interplay of electrostatic and hydrogen-bonding (H-bonds around sulfonate groups) and steric (bulky methyl group and smaller water) effects. The elucidation of the microscopic solvation of a small probe molecule in binary solvent mixtures represents the first step for understanding the interactions in more complex biochemical systems, a field where EPR spectroscopy has proved itself to be very valuable [Jeschke 2013]. In particular, this includes the potential perturbation of the H-bond network due to the presence of a spin probe.

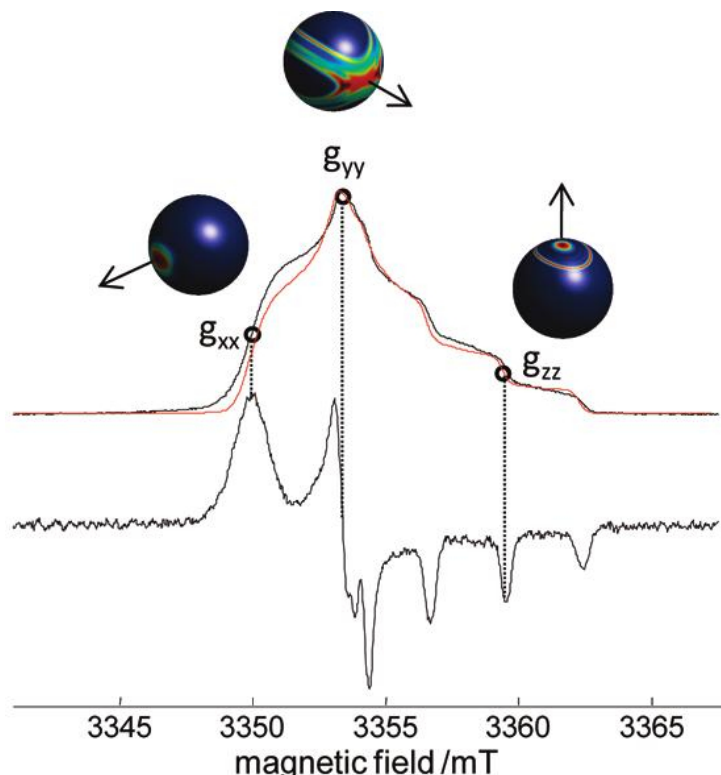


Figure 3.2: Upper: field-swept, echo-detected EPR spectrum of 2.5 mmol FS in $\text{CH}_3\text{OD}/\text{D}_2\text{O}$ recorded at 94.18 GHz and 20 K. Lower: The pseudomodulated spectrum calculated with a modulation amplitude of 0.25 mT from the absorption spectrum. The dotted lines indicate the position of the nitroxide principal axis components. Circles indicate observer field positions used for ENDOR measurements. The red spectrum shows the rigid-limit EPR spectrum simulation performed with a rhombic g-tensor and a nearly axial A-tensor. The unit spheres show the representation of orientation selections for the field positions underlying the simulations of the ENDOR spectra.

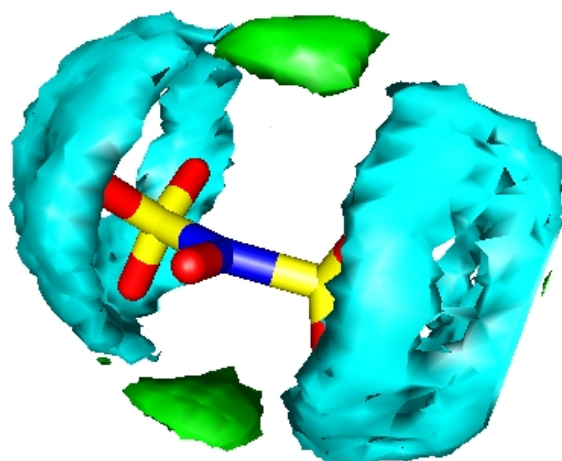


Figure 3.3: Spatial distribution function of both types of solvent protons around FS as revealed by MD simulations. Green: non-exchangeable (methyl) protons, cyan: exchangeable (polar) protons.

3.2 First principles calculation of inhomogeneous broadening in solid-state cw-EPR spectroscopy

In this work, a scheme was presented for the first-principles calculation of inhomogeneously-broadened continuous-wave-EPR (cw-EPR) lineshapes of spin centers in complex chemical environments. The approach is based on *ab-initio* MD simulations and *ab-initio* calculations of the ensemble of g- and A-tensors along the trajectory. The method incorporates temperature effects as well as the full anharmonicity of the intra- and intermolecular degrees of freedom of the system. Again the focus here was on poorly-characterized systems, e.g. powders and frozen glasses with variable microsolvation structures. As already mentioned, much of modern EPR is performed on such systems. This work in fact represents the first such attempt pertaining to a glassy frozen solution state. A number of studies that combine *ab initio* MD simulations and theoretical EPR spectroscopy have already come out [Asher et al. 2004, Asher and Kaupp 2007, Pauwels et al. 2011] which do indeed demonstrate the strength and utility of this approach. These previous studies were either focused on aqueous solutions or crystalline solids, thus they either dealt with a system in the “motionally-narrowed” limit or a system embedded a regular periodic lattice.

Solid-state spectra are generally *inhomogeneously* broadened [Poole and Farach 1971, Chapter 9], which in the context of magnetic resonance refers to the situation where the ensemble of spins in the sample has a distribution of resonance frequencies and widths, with the individual widths being much less than the total width of the frequency distribution i.e. the distribution of the effective field at different spins is broader than the natural linewidth. This happens when the dynamics of the surrounding lattice is much slower than the resonance phenomenon [Nitzan 2006, Simons and Nichols 1997]. In this situation the overall spectral line consists of a spectral distribution of individual lines merged together under one envelope. Although inhomogeneities of the static field and unresolved fine/hyperfine structure do play role in the line broadening, however, the two major non-relaxational sources of broadening in this particular case are g-tensor and nitrogen A-tensor anisotropies [Stoneham 1969, Poole and Farach 1971]. At each spin center, the values of the g and A-tensors are a complicated function of both intramolecular as well as intermolecular (solvation) factors, and it is usually the task of the spectroscopist to infer useful insight about the (possibly heterogeneous) solvation structure and the geometry of the free radical from the average lineshape. Furthermore, in the case of a powder spectrum – as is the case with glasses – the lineshape is an average over all the possible orientations of the tensors relative to the applied magnetic field.

This work can be viewed as a continuation of the previous work on FS in methanol/water [Heller et al. 2010], but this time, the focus was on presenting a more quantitative description of the solvation environment by means of *ab initio* MD simulations, combined with first principles calculations of the EPR spin Hamiltonian parameters and hence constructing an MD-averaged lineshape that explicitly accounts for inhomogeneous broadening due to g-tensor and nitrogen A-tensor anisotropies and unresolved hyperfine couplings to the solvent protons. In such a heterogeneous frozen glass, not only the relative orientation or distance between solvent molecules and FS may vary from site to site, but also the local numbers of water or methanol molecules also vary. Such poorly characterized systems present special challenges in EPR spectroscopy Pilbrow [1994]. In order to capture such heterogeneity, and its effects on the inhomogeneously broadened EPR lineshape we have designed a simulation scheme as depicted in fig. 3.4. 30 *ab initio* MD trajectories were started at regular time points from a classical MD trajectory. Each *ab initio* MD trajectory was run at a constant temperature of 300 K for 3.5 ps, followed by annealing down to 200 K in 3 ps, and a final rapid annealing

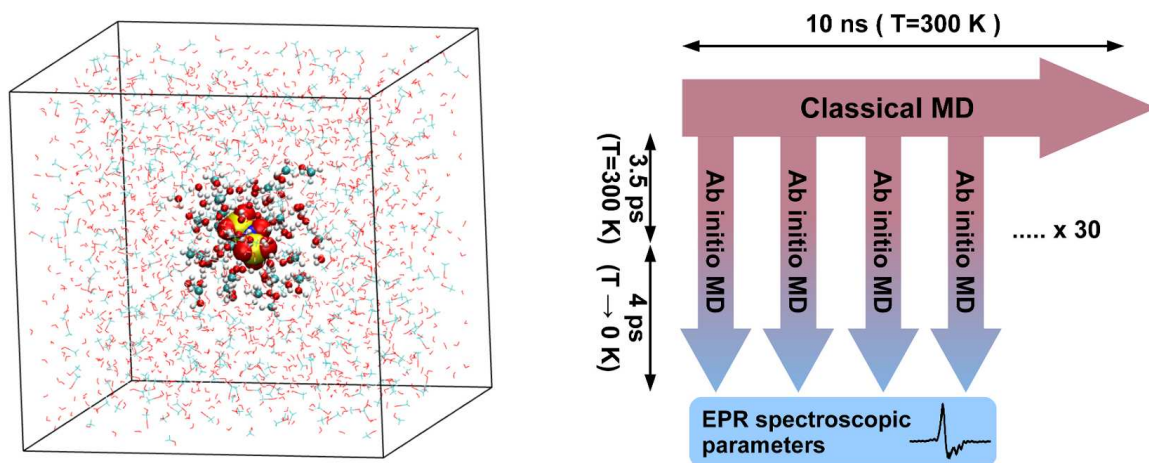


Figure 3.4: Left: A snapshot taken from classical (force field) MD trajectory of FS solvated in 50:50 methanol/water. The central part depicted in spheres represent the sub-system that is extracted for *ab initio* MD. Right: Simulation scheme.

down to 20 K in 1 ps. The final configuration from each of the annealed trajectories was used to compute spin Hamiltonian parameters (g and A -tensors, quadrupolar couplings), and then finally used to construct an EPR lineshape. EPR lineshapes were computed via exact diagonalization of the spin Hamiltonian:

$$\hat{\mathcal{H}} = \mu_B \mathbf{B}_0 \cdot \mathbf{g} \cdot \mathbf{S} + \sum_i \mathbf{S} \cdot \mathbf{A}_i \cdot \mathbf{I}_i - \mu_N \sum_i g_N \mathbf{I}_i \cdot \mathbf{B}_0 + \mathbf{I} \cdot \mathbf{Q} \cdot \mathbf{I}$$

Where the terms from left to right are the electron Zeeman term, the hyperfine coupling, the nuclear Zeeman terms, and the quadrupolar coupling (only for nitrogen). Only the five most strongly coupled solvent hydrogens were included in the simulation. A C++ program was developed (construct the spin Hamiltonian, perform the diagonalization, compute the transition moments, powder averaging) using the Eigen template library [Guennebaud et al. 2010]. Adaptive segmentation of the field values was implemented [Stoll and Schweiger 2003], and powder averaging was performed on a Lebedev 101 hemispherical grid [Lebedev and Laikov 1999, Stevansson and Edén 2006] (MPI-parallelized). No explicit relaxation term was included in the spin Hamiltonian, instead the damping of the spin coherences (transverse relaxation) was accounted for phenomenologically by convoluting the frequency domain spectrum with a decaying exponential.

Analysis of the *ab initio* MD trajectories provides a picture of the solvation shell very close to the one from classical MD. Again, it is found to be highly anisotropic with clear and distinct spatial preferences for water and for methanol. The structure of the hydrogen bonding networks, and the conformational preferences of the solvated salt (chapter 5, figs 4–6), all agree very well with evidence from EPR and ENDOR spectroscopy [Heller et al. 2010, Hinderberger et al. 2004].

MD-averaged nitrogen A -tensor components showed excellent agreement with experiment (fig. 3.5 left). *ab initio* g tensor components were not as good (particularly the g_{xx} -component) (fig. 3.5 right), but this is a well-known issue with DFT predictions of this quantity, where errors of the order of 1000 ppm are not uncommon, and the quality of the g -tensor prediction here is consistent with previous studies [Neese 2001, Pauwels et al. 2011, Neese 2005, Declerck et al. 2006, Malkina et al. 2000].

We have also established a number of correlations between g -tensor and nitrogen A -tensor

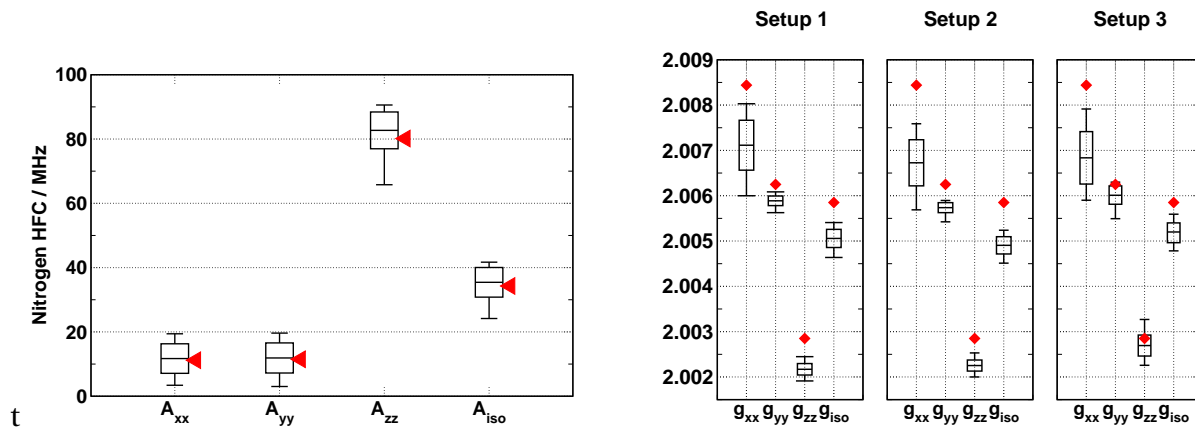


Figure 3.5: Left: MD-averaged principal values of the nitrogen hyperfine coupling tensor (Center bar of each rectangle), their standard deviation (upper/lower border of rectangle), and minimum/maximum values from the sampling (error bars). The red triangles mark the experimental values. Right: Same plot for the g tensor computed using three different setups. Setup 1: PBE0 and GIAO (Gaussian 09 [Frisch et al. 2009]), setup 2: PBE0 in Orca [Neese 2001; 2005], setup 3: PBE using GAPW in CP2K [Weber et al. 2009]. The diamond symbols mark the experimental values.

components and inter/intra molecular geometric parameters. Generally, both tensors are more sensitive to the geometry of FS itself, followed by solvation effects. One of the more important correlations we found is between the nitrogen A_{iso} and the S-N-O-S improper torsion of FS (fig. 3.6 left), which is largely insensitive to solvation effects, and thus can serve as an experimental “probe” of the planarity of FS. The MD-averaged improper angle was found to be slightly off-planar, which also agrees with the results previously reported by Hinderberger et al. based on rotational diffusion tensors from the simulation of cw-EPR spectra [Hinderberger et al. 2004]. We also found that the rhombicity of the nitrogen A-tensor is related to the hydrogen bond between the nitroxy group and solvent (fig. 3.6 right). Though this rhombicity is not detectable in cw-EPR, it is detectable with other techniques *e.g.* ENDOR.

The simulated MD-averaged lineshape shows good agreement with experiment (fig. 3.7 left), reproducing all the experimental lineshape features except for the low-field peak corresponding to g_{xx} , which is attributed to the relatively large error in the corresponding computed quantity, and strong variation in this particular g-tensor component with the (highly variable) hydrogen bond strength to the NO. Decomposing the total computed lineshape into two limiting situations: the strongly hydrogen bonded limit, and the non-solvated limit reveals the g-tensor strain corresponding to this variability in the NO solvation. It is worth noting here that the low-field peak of the experimental spectrum was not very-well reproduced also by the empirical spin Hamiltonian based on least-squares fitting, which was also attributed previously to g-tensor strain [Heller et al. 2010]. Thus, even though this particular part of the experimental spectrum is not well-reproduced by our theoretical lineshape, we were still able to explicitly show how variation in the solvation structure is directly reflected in the lineshape.

All the work in this publication was done by the author of this thesis with small contributions from Milian Wolff (MPI parallelization) and Adrian Glaubitz (integration over the Lebedev Grids).

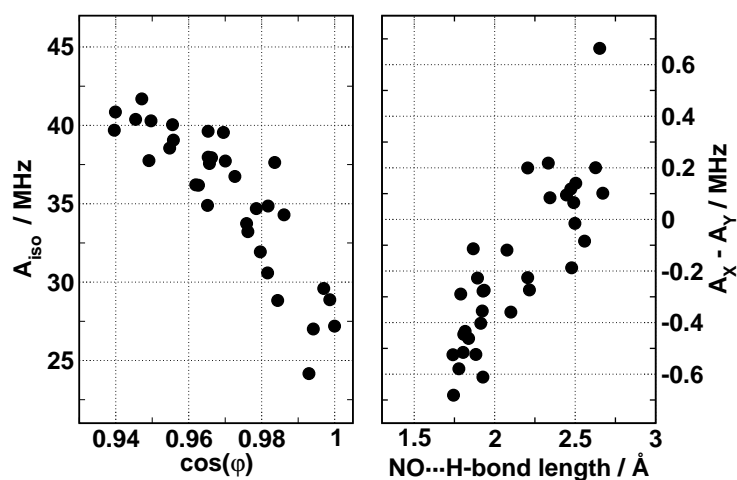


Figure 3.6: Scatterplots of nitrogen A_{iso} against FS improper torsion (Left) and of the nitrogen A-tensor rhombicity (δA) against the NO...H-bond length (right).

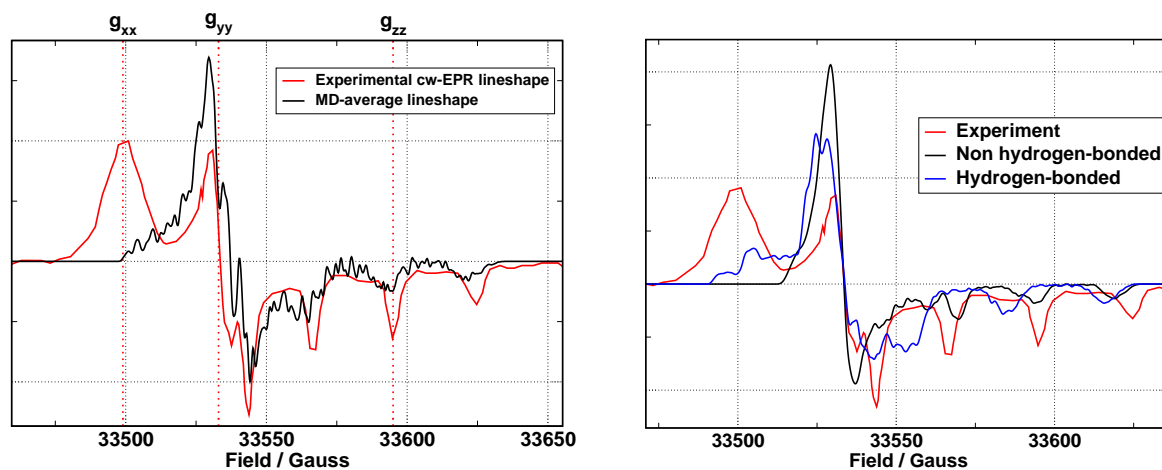


Figure 3.7: Left: Annealed MD-averaged cw-EPR lineshape. The three dotted red lines mark the experimental principal components of the g-tensor. Right: Decomposing the total annealed MD-averaged lineshapes into two lineshapes according to solvation of the FS nitroxy group (NO). Black lineshape: NO strongly hydrogen bonded, Red lineshape: NO not hydrogen bonded.

3.3 Unraveling the existence of dynamic water channels in light-harvesting proteins: α -C-phyocyanobilin in vitro

X-ray crystallography and NMR spectroscopy are the main experimental techniques that provide protein structures at atomic resolution [Snyder et al. 2005]. Each of the two methods has its well-known advantages and technical limitations [Kirchmair et al. 2008]. Soon after the introduction of x-ray crystallography, it was accepted that it gives the correct picture of protein folding in spite of the non-physiological environment of a single crystal. However, some differences between solution-state and crystal structures of proteins are expected to — and indeed known to — exist. For instance, in single crystals the protein molecules are densely packed, which may immobilize surface side-chains or even backbone segments that exhibit high mobility in the isolated protein [Billeter et al. 1992]. As early as 1964, comparisons between NMR and x-ray structures of proteins were already being done to investigate differences between solution-state and crystal structures [Praissman 1964]. In the second half of the 1980s, NMR established itself as an alternative method for protein structure determination at a resolution comparable to that given by X-ray crystallography. According to the statistics posted on the PDB website as of April 2012, the protein data bank has a total of 74603 deposited protein structures. Approximately 10% of these were obtained using NMR, the absolute majority coming from X-ray crystallography. Comparisons between protein structures obtained by both methods require the availability of coordinates from both NMR and from X-ray crystallography for the same protein. This excludes proteins from different species, cases where one structure is for the free protein and the other for a complexed form, or where protein fragments do not have the same length [Billeter et al. 1992]. Fortunately, with the exponential growth in the number of entries in the PDB, statistically-significant comparisons are becoming more and more accessible. A large scale comparison on a set of 148 protein structure pairs revealed that in 73 proteins, the core heavy atoms are located at statistically different positions [Andrec et al. 2007]. The authors suggest several reasons for this finding: Crystal packing effects, the presence of interactions (steric interactions, salt bridges, hydrogen bonds) in the crystalline state that are otherwise missing for the single protein, and the different refinement methods of both approaches. In another study on 78 proteins determined by both NMR and X-ray methods, it was found that 18 proteins had obvious large-scale structural differences that seem to reflect a difference of crystal and solution structures. There was also a statistically-significant difference in the other 60 pairs of structures in inter-residue contacts, which was mainly attributed to a difference in mathematical treatment of experimental results. In addition to such static structural differences, differences in the dynamics of NMR and X-ray protein structures are also known to exist. As one might expect, the large-amplitude motions sampled in solution are restricted in protein crystals [Yang et al. 2007].

In a relatively recent study, the ^{15}N NMR spectrum of α -C-Phycocyanin (α -C-PC) from *Mastigocladus laminosus* has been compared to that of the cyanobacterial phytochrome Cph1, providing insight into the structure and dynamics of the binding pocket of the latter [Hahn et al. 2007]. In that study, the ^1H , ^{15}N HMQC NMR spectrum of labeled α -C-PC revealed five coherences with a nitrogen chemical shift more than 130 ppm (chapter 6, fig 3). Of these five signals, two showed an interaction in the NOESY spectrum and were thus identified as **HB** and **HC** of the chromophore, phycocyanobilin (PCB, see fig. 3.8) due to their proximity. In the original published assignment a peak was observed showing an interaction with two protons in the 7.0–7.5 ppm range, and was identified as **HA** due to its proximity to the backbone amine protons of Ala75 and Tyr74. **HD** did not show any interactions, possibly due to its location at the edge of the binding pocket facing the bulk solvent, and the correlation at 149.4/9.5 ppm was assigned to it. Such assignment seemed to be the most plausible initially, however, based

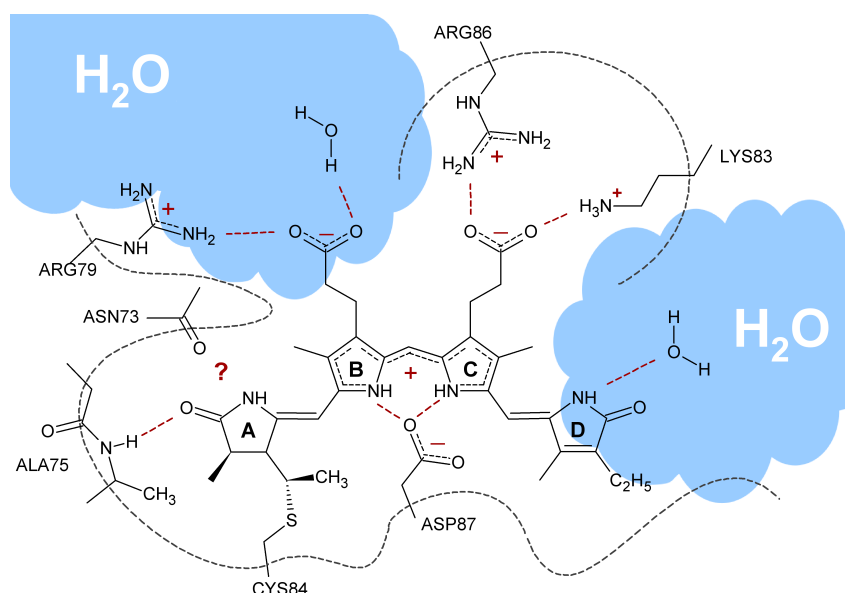


Figure 3.8: A two-dimensional projection of PCB in the α -C-PC binding pocket showing the various interactions with the binding site. The four nitrogens in PCB are referred to as NA, NB, NC, and ND, and their attached hydrogens similarly: HA, HB, HC, and HD.

on more recent NMR work on isolated PCB in HMPT [Röben and Schmieder 2011], and from solid-state NMR of cyanobacterial phytochrome (Cph1) [Rohmer et al. 2008], there was some doubt that the initial assignment of ring D, might not be correct.

In this work [Elgabarty et al. 2013] classical (force field) and hybrid *ab initio* QM/MM MD simulations and theoretical NMR chemical shift calculations were performed on the bilin chromophore phycocyanobilin in the binding pocket of α -C-PC (fig. 3.8). We exploited the high sensitivity of *ab initio* NMR calculations as an extremely sensitive local probe at the sub-Angstrom range, to reveal structural differences between the crystal structure and the solution state structure. More generally, we propose an *ab initio* approach that can accurately account for local geometric differences between the X-ray structure of a protein and its solution structure, requiring only a minimal set of experimental NMR measurements. For the MD simulations, the QM region consisted of the PCB chromophore, the attached CYS84 side chain, and the ASP87 side chain fig. 3.8. The QM/MM bond interfaces in CYS84 and ASP87 were handled using an optimized capping potential [Schiffmann and Sebastiani 2011, Ihrig et al. 2011]. For NMR chemical shielding calculations, which were also computed in a QM/MM setup, the QM region was extended to include the part of the protein backbone that faces ring A of PCB as shown in fig. 3.9.

Figure 3.10 left shows the X-ray structure of one α -C-PC monomer. The monomer has eight α -helices arranged in a globin-like fold [Schirmer et al. 1987, Duerring et al. 1988]. The first two helices in the α -subunit (residues 1–33, depicted in light-blue color) are packed against the β -subunit in the trimeric X-ray structure. Classical MD simulations revealed a large-amplitude motion in solution: we found that the first two helices, free in water, undergo a swinging motion around a hinge at residues ARG33-ALA34, between the second and third alpha-helix (fig. 3.10 middle). The classical MD-time evolution of backbone atoms RMSD relative to the X-ray structure is shown on the right in fig. 3.10. Two plots are shown, one for the entire protein chain, and the other excluding the first two helices. The RMSD excluding the first two helices is very stable with an average of 1.28 Å. On the other hand, the RMSD of the entire α -subunit shows significant deviation from the X-ray structure, with an average of 3.15 Å, which is attributed to the swinging movement just described.

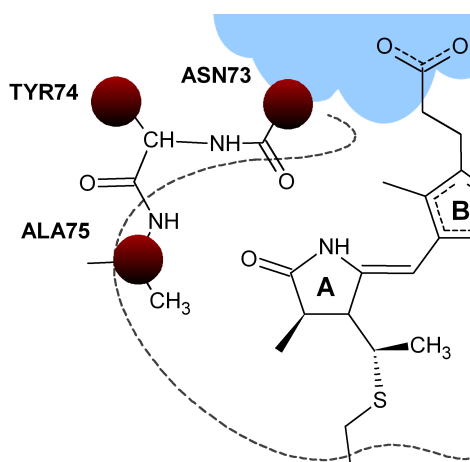


Figure 3.9: QM/MM partitioning used for the NMR calculations. Additional capping atoms were introduced to encompass the backbone segment between ASN73 and ALA75 in the QM region [Ihrig et al. 2011].

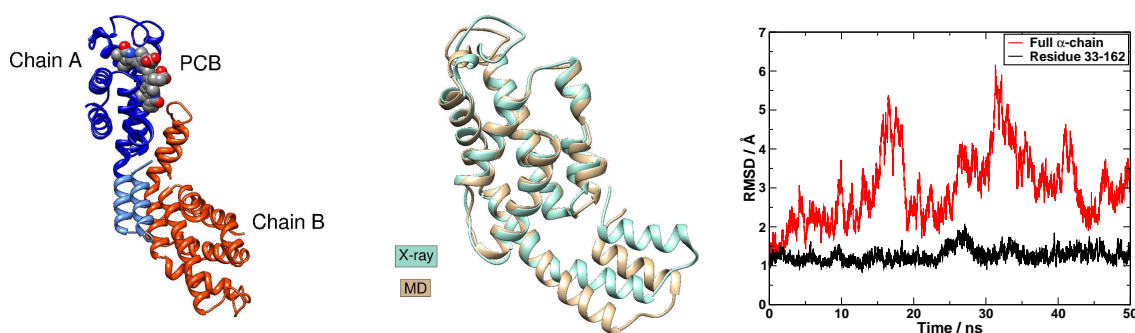


Figure 3.10: Left: X-ray structure of a C-PC monomer showing the α (blue) and β (orange) subunits. Each subunit has an eight α -helical globin-like fold. The two light-blue helices in the α -chain (residue 1 to 33) are packed against the β -subunit. Middle: X-ray structure of the α -subunit (cyan) aligned to average structure (yellow) from last 10 ns of classical MD trajectory. Right: Backbone RMSD relative to the X-ray structure along the classical MD trajectory. The red trace is for the whole protein backbone, and the black one is obtained when residues 1 to 33 are excluded.

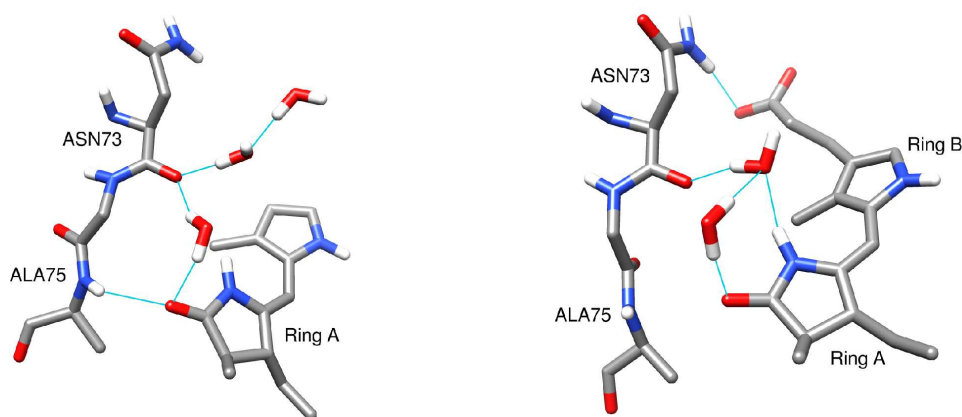


Figure 3.11: Examples of the water wires that form inside the PCB binding pocket, bridging ring A to ASN73.

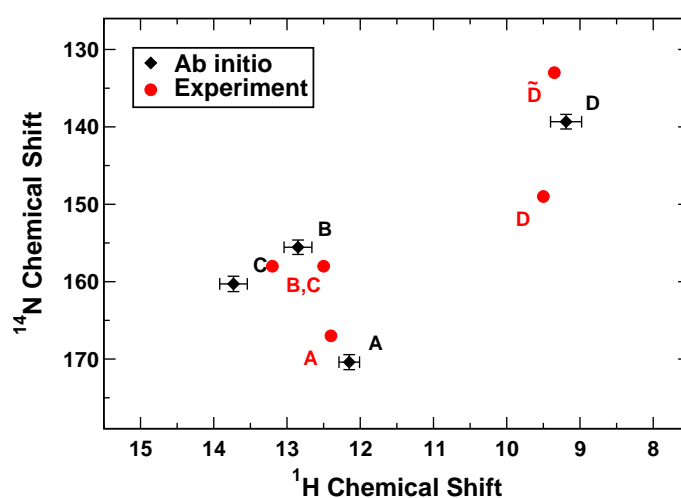


Figure 3.12: MD-averaged NMR chemical shifts taken from the QM/MM trajectory in which a water wire bridges ring A to ASN73 and connects to bulk water (fig. 3.11). Error bars indicate the standard error.

Further comparison of computational and experimental data leads to more subtle structural differences between the solution-state and the crystalline structure, in particular regarding the microsolvation of ring A of the bilin chromophore. The loop in the PCB binding site which is packed against the crystal packing surface, has more freedom in solution which leads to its movement away from PCB. This allows one water molecule to pour inside in the binding pocket, bridging ring A to ASN73 backbone, and eventually forming a stable water wire that connects to bulk solvent fig. 3.11. The QM/MM MD-averaged NMR chemical shifts based on this structural picture show very good agreement with experiment fig. 3.12.

This approach of computing ensemble averaged NMR chemical shifts from first principles molecular dynamics simulations leads to considerable improvement in agreement between theoretical and experimental results. More generally, it provides a working method to reconcile X-ray crystal structures and solution state structures using a minimal set of experimental NMR data. The speed with which NMR chemical shifts can be computed on modern computers makes the method quite affordable, even with the extensive sampling required to converge the averaged *ab initio* NMR chemical shifts. Another possible application of this approach is for membrane proteins with poorly resolved structures. If one is particularly interested in one region, then this method provides a microscopic probe that can look

at distances at the sub-angstrom range provided that experimental NMR/EPR signatures are available. The argument applies equally well to protein structures that cannot be investigated by NMR (large proteins). This work can be viewed as a continuation of the efforts that utilize *ab initio* QM methods in structural biology, from assessing the quality of X-ray structures by *ab initio* ^{13}C NMR [Vila and Scheraga 2009], to the use of *ab initio* methods in optimizing and refining X-ray structures [Ryde and Nilsson 2003, Hsiao et al. 2010]. We go here one step further by combining MD and NMR calculations to provide results directly comparable to a highly sensitive experimental observable. It is interesting to note that Bertini et al. suggested a scheme where solution structures of proteins can be determined from X-ray data and a minimal set of *experimental* NMR Data, and applied it to Calmodulin-peptide complexes as examples [Bertini et al. 2009]. Our method here can be considered as the theoretical complement of their work.

Chapter 4

Paper I

Solvation of Small Disulfonate Anions in Water/Methanol Mixtures Characterized by High-Field Pulse Electron Nuclear Double Resonance and Molecular Dynamics Simulations

Jeannine Heller, Hossam Elgabarty, Bilin Zhuang, Daniel Sebastiani, and Dariush
Hinderberger

J. Phys. Chem. B, 2010, 114, 7429-38.

Reproduced with permission. Copyright 2010 American Chemical Society.

<http://dx.doi.org/10.1021/jp910335t>

Solvation of Small Disulfonate Anions in Water/Methanol Mixtures Characterized by High-Field Pulse Electron Nuclear Double Resonance and Molecular Dynamics Simulations

Jeannine Heller,[†] Hossam Elgabarty,[‡] Bilin Zhuang,[†] Daniel Sebastiani,^{*,‡} and Dariush Hinderberger^{*,†}

Max Planck Institute for Polymer Research, Ackermannweg 10, 55128 Mainz, Germany, and Department of Physics, Freie Universität Berlin, Arnimallee 14, 14195 Berlin, Germany

Received: October 29, 2009; Revised Manuscript Received: April 23, 2010

The solvation of Fremy's salt, the paramagnetic nitrosodisulfonate anion $\text{ON}(\text{SO}_3^-)_2$, in binary solvent mixtures was investigated by means of pulse (Mims- and Davies-type) electron nuclear double resonance (ENDOR) spectroscopy and molecular dynamics (MD) simulations. ^1H and ^2H pulse ENDOR measurements were performed on small Fremy's salt radicals in isotope-substituted solvent mixtures of methanol and water in frozen solution. We were able to obtain well-resolved, orientation-selective, high-field/high-frequency pulse ENDOR spectra of *methyl* protons from the alcohol moiety and *exchangeable* protons from the alcohol-hydroxyl group and water. In the studied solvent systems (volume ratio $v/v = 30:70, 50:50, 70:30$), the solvation of 2.5 mM Fremy's salt by methyl protons was found to be almost identical. From the analysis of the dependence of pulse ENDOR spectra on the observer field position and spectral simulations, we obtained the principal components of the hyperfine coupling (hfc) tensor for each class of protons. The combination of Mims- and Davies-type pulse ENDOR measurements was necessary to obtain blind spot free information on hfc that spans a broad range of 0.25–6 MHz. Using the point-dipole approximation, the dipolar hfc component yields a prominent electron–nuclear distance of 3.5 Å between Fremy's salt and methyl protons, which was found along the molecular z -axis (perpendicular to the approximate plane spanned by $\text{ON}(\text{S})_2$) of the probe molecule. Exchangeable protons were found to be distributed nearly isotropically, forming a hydrogen-bonded network around the sulfonate groups. The distribution of exchangeable and methyl protons found in MD simulations is in very good agreement with the pulse ENDOR results, and we find that solvation is dominated by an interplay of H-bond (electrostatic) interactions and steric properties. The elucidation of the microscopic solvation of a small probe molecule in binary solvent mixtures represents the first step for understanding the interactions in more complex biochemical systems. In particular, this includes the potential perturbation of the H-bond network due to the presence of a spin probe or other polar molecules.

1. Introduction

The understanding of ion solvation in multicomponent systems is crucial for many chemical reactions,¹ in electrochemistry,² and for understanding the role of ions in biological systems. In solution, ions interact with one another and with solvent molecules. In mixed solvents, the solute may interact specifically with one solvent species, thus changing the composition of solvation shell from that of the bulk. This phenomenon of "preferential solvation"³ has been studied extensively during the past years by applying experimental^{4–7} and theoretical^{8–11} methods.

The study of solvation of paramagnetic ions with methods of electron paramagnetic resonance (EPR) spectroscopy was established more than 20 years ago, in particular for transition metal ions.^{12–14} The solvation shell of the VO^{2+} ion was one of the first examined with continuous wave (CW) electron nuclear double resonance (ENDOR) spectroscopy.^{13,15,16} These measurements were restricted to paramagnetic ions that exhibit large g -anisotropy even at low magnetic field. Today, modern

spectrometers operating at higher magnetic field offer the possibility to study systems with very small g -anisotropies like nitroxides. Nitroxides are compounds containing the



group which has an unpaired electron located in a $2p\pi^*$ molecular orbital of the NO group (two-center, three-electron bonding). EPR spectra are very sensitive to environmental changes like polarity of the solvents, and especially the A_{zz} principal value of the nitrogen hyperfine tensor and the g_{xx} principal value of the g -tensor were found to depend on the local dielectric medium and hydrogen bonding to the N–O group, which allows their use in biochemical research of diamagnetic proteins in combination with site-directed spin labeling.^{17,18} Although in such EPR measurements binary solvent mixtures are usually employed because of the need for a cryoprotectant (pulsed measurements are usually performed at cryogenic temperatures), the effect of the nitroxide solvation is only rarely discussed. In this study, we chose Fremy's salt as a simple model ion to investigate its solvation in binary water–organic solvent mixtures.

In magnetic resonance spectroscopy, Fremy's salt (FS, potassium nitrosodisulfonate $\text{ON}(\text{SO}_3^-)_2$) is a well-known and frequently used free radical. It is used as an EPR standard for

* To whom correspondence should be addressed. E-mail: dariush.hinderberger@mpip-mainz.mpg.de. Tel.: +49 6131 379 126. Fax: +49 6131 379 100. E-mail: daniel.sebastiani@fu-berlin.de. Tel.: +49 30 838 53037.

[†] Max Planck Institute for Polymer Research.

[‡] Freie Universität Berlin.

g-value determination and radical quantitation¹⁹ and, due to the sensitivity of its ¹⁴N hyperfine splitting toward temperature, as an internal thermometer in solution EPR.²⁰ As an oxidizing agent, it is widely used as a model for reactive oxygen species (ROS).^{21,22} Recently, the narrow line shape of FS—resulting from the lack of unresolved ¹H hyperfine splittings—has been utilized in new applications; e.g., it could be used to study the distribution of counterions in polyelectrolyte systems in solution^{23–25} and for NMR signal enhancement by dynamic nuclear polarization (DNP).²⁶

We chose methanol–water mixtures as binary solvent mixtures as they represent the simplest case of an aqueous solution with a cryoprotectant (usually a higher alcohol like ethylene glycol or glycerol is used). Furthermore, such mixtures are used as reaction media in organic synthesis,¹ and it was found that a higher methanol content is responsible for enhanced kinetics in some oxidation reactions, indicating an important potential effect of preferential solvation.²⁷

In this study, we use Mims²⁸ and Davies²⁹ pulse ENDOR experiments to study the solvation of FS in methanol–water mixtures at high magnetic field *B*/high frequency (W-Band, *B* ~ 3350 mT, microwave frequency ~94.5 GHz). Our main tool to achieve selectivity concerning the solvation of the small probe molecule is the selective isotope modification of either *methyl* protons (–CH₃) of methanol or *exchangeable* protons from the alcohol-hydroxyl group and water. Working at high magnetic field has two advantages: (i) the **g**- and **A**-matrices are fully resolved in the nitroxide EPR spectrum, thus allowing orientation-resolved EPR and ENDOR, and (ii) the Larmor frequency of ¹H is about 149 MHz and of ²H is 23 MHz, hence they are well separated from each other. Together, this allows independent and molecular orientation-dependent monitoring of either proton–electron hyperfine (hf) interactions or deuteron–electron hf interactions in one ENDOR experiment and with this a selective “switching off” of one chemical proton species (exchangeable or methyl protons). In an ¹H-ENDOR spectrum of the CH₃OD–D₂O mixture, only methyl protons contribute to the ENDOR signal, while in an ²H-ENDOR measurement of the same sample only exchangeable protons that are hyperfine coupled to FS are monitored. Neglecting the small isotope effect of deuteration,^{30,31} combining high-field ENDOR and selective isotope substitution allows a more simplified data interpretation. The qualitative comparison of the EPR spectroscopic findings with the picture of solvation derived from our classical molecular dynamics simulations gives unique insights into the solvation shell of the small disulfonate anions in water/methanol solution.

2. Experimental Section

2.1. Samples. Fremy’s salt, FS (K₂[ON(SO₃)₂] potassium nitrosodisulfonate, ICN Biomedicals Inc.), was used without purification. D₂O (99.9%), methanol-*d*₁ (CAS 1455-13-6, CH₃OD, 99.5%), methanol-*d*₃ (CAS 1849-29-2, CD₃OH, 99.8%), and methanol-*d*₄ (CAS 811-98-3, CD₄O, 99%) were obtained from Aldrich. All solutions were prepared at ambient conditions without the use of inert gas. Fremy’s salt undergoes decomposition in the solid state³² and in aqueous³³ as well as nonaqueous³⁴ solution. The optimum solution pH for FS stability is between 9 and 10,³³ and therefore solutions are usually basified with either potassium hydroxide (KOH),³⁵ carbonate (K₂CO₃),³⁶ or hydrogen carbonate (KHCO₃).³⁷ The two latter have the advantage of not only producing alkaline solutions but also buffering these solutions. Nevertheless, we explicitly used KOH solutions to adjust the pH to exclude the introduction of a new ion species (carbonate ions) into the system. In all samples, we

TABLE 1: Investigated Samples of 2.5 mM Fremy’s Salt in Methanol–Water Mixtures^a

solvent	<i>V</i> _M : <i>V</i> _W	<i>x</i> _M	<i>w</i> _M	ε	η [mPa s]
CH ₃ OD:D ₂ O	30:70	0.15	0.24	76	1.47
CH ₃ OD:D ₂ O	50:50	0.31	0.42	65	1.57
CH ₃ OD:D ₂ O	70:30	0.49	0.63	53	1.34
CD ₃ OH:H ₂ O	50:50	0.31	0.46	65	1.57
CD ₃ OD:D ₂ O	50:50	0.31	0.44	65	1.57
CH ₃ OH:H ₂ O	50:50	0.31	0.44	65	1.57

^a The static dielectric constant ε (adapted from ref 39) and the absolute viscosity η (adapted from ref 38) of the solvent mixtures are listed for binary solvent mixtures at *T* = 298.15 K. *V*_M, *V*_W: Volume ratio for methanol and water. *x*_M, *w*_M: Molar ratio and weight ratio of methanol.

used a KOH concentration of *c*_{KOH} = 9.8 × 10^{−4} M and FS concentrations of 2.5 mM.

Stock solutions of 10 mM FS in Milli-Q water (Millipore) and D₂O were prepared, and a solution of 2 M KOH solution was added. The obtained solutions were diluted to 5 mM FS concentration and stored at −18 °C. From the aqueous solutions, the alcohol/water mixtures were prepared by adding the according volume of methanol. Volume ratios of methanol–water *v/v* = 30:70, 50:50, and 70:30 were prepared (Table 1), corresponding to a methanol molar ratio of *x*_M = 0.16, 0.31, and 0.49, respectively. Solutions with higher methanol ratios (*x*_M > 0.5) were not prepared due to reduced solubility of FS in these mixtures. Lower concentrations (*x*_M < 0.16) could not be tested as they do not form glassy solutions upon freezing within our experimental setup. In purely aqueous frozen solutions, local crystallization will change the solvation characteristics and complicate data analysis and is therefore not desired. All experiments are analyzed under the assumption that the shock frozen solutions with methanol as cryoprotectant represent the solvation characteristics at room temperature (or more precisely at the glass transition temperature). This assumption is essential for the comparison of the ENDOR data and the MD simulations.

The following solvent mixtures were used to distinguish between exchangeable protons arising from hydroxyl groups and water and nonexchangeable protons from the methyl group: H₂O/CH₃OH, i.e., the completely protonated mixture; D₂O/CD₃OD, i.e., the completely deuterated mixture; D₂O/CH₃OD, where only the exchangeable hydrogens are replaced by ²H; and H₂O/CD₃OH, where the nonexchangeable hydrogens are deuterated. The prepared samples are listed in Table 1 together with some properties of the respective pure methanol–water mixtures. Both dielectric constant ε and viscosity η are highly temperature dependent and are only shown for ambient conditions, under which the samples were prepared (*T* ~ 298 K). The viscosity of pure methanol–water mixtures reaches a maximum at a methanol molar ratio of approximately *x*_M ~ 0.29.³⁸

2.2. EPR Spectroscopy. Instrumentation. W-band measurements were performed on a BRUKER EleXsys E680 spectrometer using a Bruker EN 660-1021 H Tera Flex ENDOR-resonator. The resonator dip was broad enough that further overcoupling was not needed. All measurements were performed at 20 K with liquid helium cooling by an Oxford CF935 cryostat with an Oxford ITC4 temperature controller. Samples were loaded with a Hamilton syringe into 0.7 mm inner diameter homemade CFQ-quartz capillaries to a height of about 3 mm and inserted into the resonator at 50 K and then cooled to 20 K.

Orientation Selection. EPR spectra of nitroxides in frozen solutions result from superposition of EPR signals from all

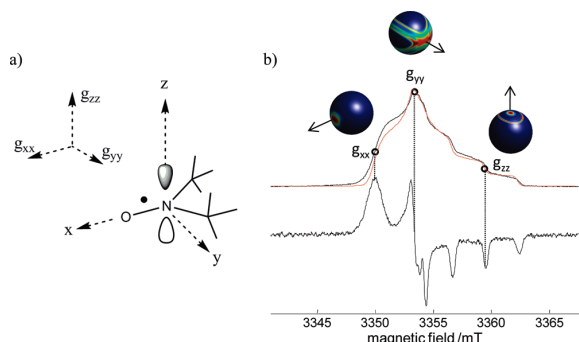


Figure 1. (a) Nitroxide group and its molecular coordinate axis system with the x -axis along the NO bond and z -axis along the $2p_{\pi}$ orbital. The \mathbf{g} -tensor principal axes system coincides with the molecular axes and the hyperfine tensor coordinate system.⁴⁰ (b) Upper: field-swept, echo-detected EPR spectrum of 2.5 mM Fremy's salt in $\text{CH}_3\text{OD}/\text{D}_2\text{O}$ with a volume ratio of $v/v = 70/30$, recorded at 94.18 GHz and 20 K. The pulse sequence was $\pi/2-\tau-\pi-\tau$ -echo, with $t_{\pi/2} = 48$ ns, $t_{\pi} = 96$ ns, and $\tau = 300$ ns. Lower: The pseudomodulated spectrum calculated with a modulation amplitude of 0.25 mT from the absorption spectrum. The dotted lines indicate the position of the nitroxide principal axis components as shown in the left scheme. Circles indicate observer field positions B_{ENDOR} used for ENDOR measurements. The red spectrum shows the rigid-limit EPR spectrum simulation performed with a rhombic \mathbf{g} -tensor ($g_{zz} < g_{yy} < g_{xx}$) and a nearly axial \mathbf{A} -tensor. The unit spheres show the representation of orientation selections for the field positions underlying the simulations of the ENDOR spectra.

molecular orientations with respect to the outer magnetic field. Depending on the magnitude of the magnetic field B_0 , the g -anisotropy, and the inhomogeneous line width due to unresolved hf couplings, each field position in the EPR spectrum represents a specific manifold of relative molecular orientations from the entire orientation distribution. Going from conventional X- (~ 9.4 GHz) to W-band (~ 94.5 GHz) frequencies, the increase of the Zeeman energy, which is proportional to the static external magnetic field B_0 , leads to a higher spectral resolution in the EPR spectrum. In particular, for nitroxides which have only small g -anisotropies (in the range of 10^{-3} – 10^{-4}), the respective increase of B_0 to ~ 3400 mT is necessary to resolve the \mathbf{g} -tensor principal values.⁴⁰ This is not yet possible at the X-band and only partially achieved at intermediate frequencies (e.g., Q-band, 35 GHz). If the g -anisotropy is larger than the hyperfine interaction (as is the case for nitroxides at the W-band), specific turning points in the spectrum can be used to select certain orientations of a radical with respect to the magnetic field. From these magnetic field positions, “single-crystal-like” ENDOR spectra can be obtained equivalent to those from oriented single crystals, and hf tensors can be elucidated with respect to the \mathbf{g} -tensor principal axes system. This is commonly known as “orientation-selection” or “angle-selection”⁴¹ and was first introduced in 1970 by Rist and Hyde.⁴²

For nitroxides, the common right-hand Cartesian molecular frame is chosen, such that the x -axis coincides with the direction of the N–O bond and the z -axis is directed along the long axis of the singly occupied molecular orbital (SOMO), simplified as a $2p$ orbital of nitrogen (Figure 1a). Assuming full g -resolution, and setting the laboratory magnetic field B_{ENDOR} to the low-field turning point in the EPR spectrum of a frozen solution, a single orientation can be selected such that B_{ENDOR} is aligned parallel to the N–O bond of the nitroxide. At the high-field turning point, only those orientations are selected, for which the unique axis of the SOMO is parallel to the outer

magnetic field. At intermediate magnetic field positions, a well-defined set of orientations is selected, and the ENDOR pattern is in general more complex than a single-crystal-like spectrum.^{43,44} Due to the symmetry of the SOMO, its molecular frame coincides with the principal axis of both, the \mathbf{g} - and the \mathbf{A} -tensors.⁴⁰ The subsequent analysis of the hyperfine couplings assumes colinearity of the \mathbf{g} -tensor and hyperfine-tensor frames, which is known to be a viable approximation in nitroxide radicals in general and has been shown for Fremy's salt, too.²⁴

Pulse EPR and ENDOR Experiments. The field-swept, electron spin echo (ESE) detected EPR spectra were recorded by integrating over the echoes created with the pulse sequence $\pi/2-\tau-\pi/2$ -echo, with the pulse lengths $t_{\pi/2} = 48$ ns, $t_{\pi} = 96$ ns, and an interpulse delay of $\tau = 300$ ns. From echo-detected spectra, the characteristic points for ENDOR measurements were assigned as shown in Figure 1a. ^1H and ^2H ENDOR spectra were recorded using the Mims three-pulse scheme ($\pi/2-\tau-\pi/2-T-\pi/2$),²⁸ with the radiofrequency (RF) pulse applied during time T . A $\pi/2$ pulse length of 48 ns was used. Since Mims-type ENDOR spectra are hampered by blind spots depending on the pulse interval τ , measurements for different values of τ were performed. For ^1H measurements, typical values for τ were 172 or 200 ns, for ^2H 400–600 ns. The RF pulse length varied for ^1H and ^2H nuclei and was optimized for the studied nucleus. A typical value for ^1H was 20 μs . The RF was swept from 20 to 24 MHz for detection of deuterium hf couplings and from 139 to 147 MHz for proton hf couplings. The Davies ENDOR sequence²⁹ $\pi-T-\pi/2-\tau-\pi$ -echo was used to record ^1H spectra. The inversion π pulse was 200 ns. A radio frequency pulse length of 20 μs was applied during the time T . In the detection sequence ($\pi/2-\tau-\pi$ -echo), pulse lengths of $t_{\pi/2} = 200$ ns and $t_{\pi} = 400$ ns were used with an interpulse delay of $\tau = 548$ ns. The signal was accumulated over 2–5 h for the x - and y -position and at least 14 h for the z -position (due to the weak signal intensity, see Figure 1a).

Mims ENDOR was recorded for both proton species (methyl and exchangeable protons) and both isotopes (^1H and ^2H). Davies ENDOR was recorded only for the ^1H isotope for both proton species since the small deuterium couplings (~ 2 MHz) and weak signal intensities cannot be properly detected by the Davies ENDOR sequence.⁴⁵

2.3. Spectral Analysis. Spin Hamiltonian. The stationary Hamiltonian describes the time-independent spin-interaction energies and is given for the interaction of an $S = 1/2$ electron spin coupled to i nuclei by⁴⁵

$$H = \mu_B \mathbf{B}_0 \mathbf{g} \mathbf{S} + h \sum_i \mathbf{S} \mathbf{A}_i \mathbf{I}_i - \mu_N \sum_i g_N \mathbf{I}_i \mathbf{B}_0 + \sum_i \mathbf{I}_i \mathbf{Q}_i \mathbf{I}_i \quad (1)$$

The first term describes the electron Zeeman interaction, the second term the hyperfine interactions, the third term the nuclear Zeeman interactions, and the last term the nuclear quadrupole interactions (for nuclei with $I > 1/2$, e.g., ^2H). The terms are ordered according to their relative magnitude. \mathbf{A}_i and \mathbf{Q}_i denote the hyperfine (hf) and quadrupolar tensors, μ_B and μ_N the Bohr and nuclear magnetons, and \mathbf{S} and \mathbf{I} the electron and nuclear spin operator. \mathbf{g} is the \mathbf{g} -interaction matrix and g_N the nuclear g -factor, respectively. To first order, the last two terms do not contribute to the EPR spectrum. At low magnetic field (X-band 9.5 GHz), the powder pattern is dominated by the anisotropy of the field-independent hyperfine term. Therefore, the x - and y -orientations of the nitroxide \mathbf{g} -tensor (Figure 1) are indistinguishable. At ten times higher magnetic field (W-band 94.5

GHz), the anisotropy of the Zeeman term and all principal axis orientations are resolved.

The hf tensor \mathbf{A} consists of an isotropic part, a_{iso} , and a dipolar part T and has the principal components, $\mathbf{A} = [A_{xx}A_{yy}A_{zz}]$. If the anisotropic hyperfine coupling can be described by the point-dipole approximation, the principal values of \mathbf{A} become $A_{xx} = A_{yy} = A_{\perp} = -T + a_{\text{iso}}$ and $A_{zz} = 2T + a_{\text{iso}}$, and $T = [\mu_0/(4\pi\hbar)]g\mu_B g_N \mu_N (1/r^3)$ with r being the electron–nuclear distance.

The first-order ENDOR transition frequencies (no quadrupolar coupling) for a nucleus N are given by

$$\nu_{\pm} = \left| \nu^N \pm \frac{A^N}{2} \right| \quad (2)$$

where $\nu^N = g_N \mu_N B_0 / \hbar$ is the nuclear Larmor frequency and A^N is the orientation-dependent hyperfine coupling constant. For protons at a magnetic field of ~ 3500 mT, $\nu^H > A^H/2$, and the ENDOR spectrum is a doublet centered at the proton Larmor frequency ν^H and split by A^H . For nuclei $I > 1/2$, the nuclear frequencies additionally depend on the nuclear quadrupole interaction Q .

The anisotropic hf and quadrupolar interactions tilt the quantization axis of a nuclear spin. The criterion for the magnetic field at which the effects of tilting can be neglected is $g_N \mu_N B_0 > T_{\text{II}}, Q_{\text{II}}$ and is usually valid for nitroxides at 95 GHz.

In the case of axial symmetry of the hf interaction tensor, the distance dependence of the perpendicular component T is given by eq 3

$$T = \frac{\mu_0 \rho}{4\pi\hbar} \cdot \frac{g\mu_B g_N \mu_N}{r^3} \quad (3)$$

where $\rho = |\psi(0)|^2$ is the electron spin density.⁴⁵

Spectral simulations were performed with the program package EasySpin 3.0.0.⁴⁶ Line positions and intensities were calculated by exact matrix diagonalization of the respective spin Hamiltonian. The \mathbf{g} -tensor principal values and ^{14}N hf coupling were obtained from simulation of the powder EPR spectrum (including all orientations). The ENDOR transition frequencies were only calculated for the set of molecules that contribute to the ENDOR spectrum at the observer field position B_{ENDOR} and that are excited within a Gaussian EPR line width calculated from the pulse length t_p of the first pulse that was applied in the ENDOR experiment. The full width at half-maximum (fwhm) of this Gaussian line was determined by $2/t_p$. In all simulations, the line widths (Gaussian, Lorentzian, or Voigtian) were set empirically to fit the experimental spectra. Line widths and relative amplitudes were not determined analytically in ENDOR spectra.

Data Treatment. All spectra were background-corrected using a home-written MATLAB program, by subtracting a first-order polynomial fit from the first and last 15% of the data points (baseline regions). Mims ENDOR signals were inverted; all types of ENDOR spectra were centered around the corresponding Larmor frequency; and spectra were normalized either by their maximum or relative to the intensity of their position B_{ENDOR} in the ESE-detected EPR spectrum.

2.4. Molecular Dynamics Simulations. A Fremy's salt anion was charge neutralized by two potassium cations. The whole system was solvated with 492 methanol and 1104 water molecules in a cubic box of side length 40 Å, which corresponds to a water:methanol volume ratio of 1:1. A classical molecular

dynamics (MD) run was performed under periodic boundary conditions using the Gromacs simulation package.⁴⁷ The box was kept at a temperature of 300 K by means of Nose–Hoover thermostats^{48,49} with a coupling constant of 0.1 ps. The total simulation time was 10 ns, using a time step of 0.5 fs. The particle-mesh Ewald (PME) algorithm^{50,51} was used for long-range electrostatics interactions, and a cutoff of 9 Å was employed for the Lennard-Jones interactions with analytic long-range dispersion corrections for energy.

The OPLS force field⁵² was used for the alcohol molecules, together with the TIP3P water model.⁵³ To obtain force field parameters for the FS anion, a scan of the potential energy surface was performed in Gaussian 03 at the B3LYP/6-31+G* level.⁵⁴ We scanned each of the N–O, N–S, and S–O bond stretching modes, as well as all the bond angles in the molecule. Harmonic stretching and bending force constants were obtained by parabolic fitting of the obtained potential energy profiles. Standard values for the dihedral potentials of the FS anion were extracted from the OPLS force field. Partial atomic charges were obtained by fitting to the molecular electrostatic potential (B3LYP/6-31+G*) using the RESP method.⁵⁵

To mimic the shock freezing treatment (as done in the EPR experiments), snapshots were taken, each 50 ps from the trajectory. Each snapshot was annealed down slowly to 250 K over a time period of 200 ps and then down to 50 K in another 100 ps.

3. Results

Electron Spin Echo (ESE)-Detected EPR Spectra. All ESE-detected EPR spectra exhibit the typical nitroxide powder pattern line shape expected for a dilute distribution of nitroxide radicals. The spectra show full resolution of the \mathbf{g} -tensor and its elements g_{xx} , g_{yy} , and g_{zz} with a total width of 15 mT. Figure 1b shows a representative ESE-detected EPR spectrum (black). The spectral simulation is plotted in red. The spheres were calculated from the simulated spectra and represent the selected orientations for the field positions marked with a circle and hence the orientations selected in ENDOR experiments at these positions. As mentioned above, only at the turning points (g_{xx} and g_{zz}) a finite solid angle of molecular orientation is selected, whereas at the intermediate position and g_{yy} a well-defined set of orientations contribute to the ENDOR signal. In particular, at the maximum of the EPR spectrum molecular orientations that have x - and z -contributions also contribute to the ENDOR spectrum.

The best simulations were obtained by introducing an anisotropic line width that can model small effects such as unresolved hyperfine splitting or g - or A -strain. The EPR parameters found from simulating the experimental EPR spectra are $g = [2.00844, 2.00625, 2.00285] \pm 2 \times 10^{-5}$ and $A = [0.41, 0.40, 2.86]$ mT for the principal values of the \mathbf{g} - and \mathbf{A} -tensor, respectively. The errors for \mathbf{A} -tensor components are ± 0.1 mT for the x -, ± 0.02 mT for the y -, and ± 0.01 mT for the z -component. A Voigtian-type line width is found with a fwhm of 0.3 mT (Gaussian part) and 0.09 mT (Lorentzian part). In solid state EPR spectra, homogeneous line broadening (T_2 -broadening) is usually negligible. Thus, the slight mismatch between simulation with a purely Gaussian line and experiment might be due to nuclear relaxation effects. An orientation-dependent phenomenological broadening of 15–25 MHz is found along x , 8–17 MHz along y , and 8–19 MHz along z , in which the magnitude follows the order $x > z > y$ for all samples. Due to this broadening, the error for the x -component of the \mathbf{A} -tensor is much higher than for the other components. Even

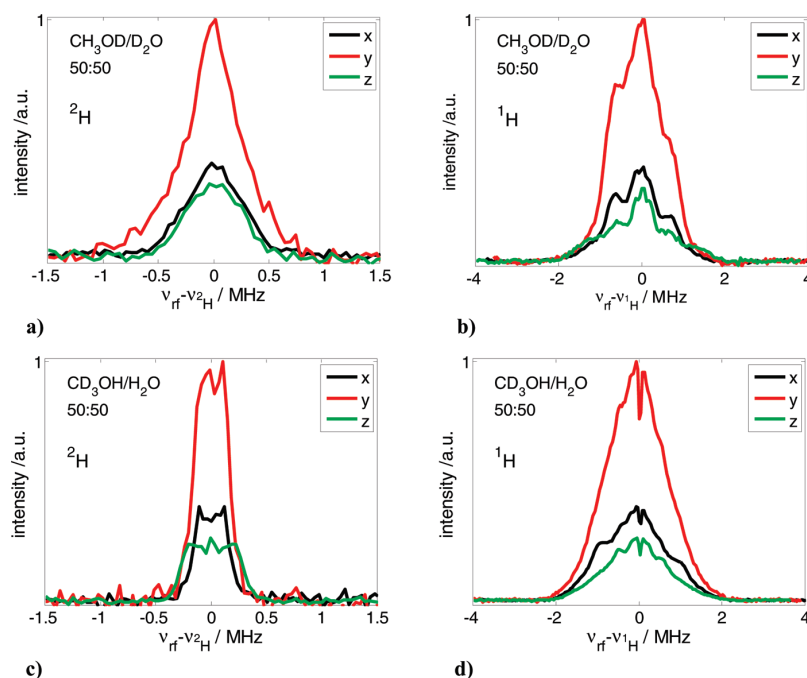


Figure 2. Orientation-selective Mims-ENDOR spectra of 2.5 mM Fremy's salt in frozen solution. (a), (b) ^2H spectra and ^1H spectra of the solvent mixture $\text{CH}_3\text{OD}/\text{D}_2\text{O}$ ($v/v = 50:50$). (c), (d) ^2H spectra and ^1H spectra of the solvent mixture $\text{CD}_3\text{OH}/\text{H}_2\text{O}$ ($v/v = 50:50$). Spectra were recorded from the low-field turning point g_{xx} (black) to the high-field turning point g_{zz} (green) of the EPR spectrum. Experimental parameters: $T = 20\text{ K}$; MW $\pi/2$ pulse, 48 ns; τ for ^1H , 172 ns (b), 200 ns (d), 200 ns (a), 600 ns (c). RF pulse, 20 μs for ^1H and 35 μs for ^2H . The spectra are normalized relative to the EPR spectral intensity at their field position B_{ENDOR} .

with this additional broadening, the low-field flank of the simulated spectra never reaches the experimental spectrum. Better results are obtained by simulation of two species with different g_{xx} value (with the other parameters identical). This could be indicative of the existence of some FS NO-groups, which participate in hydrogen-bonded structures, as the g_{xx} value is known to be sensitive to the formation of hydrogen bonds. At this point we refrain from a more detailed analysis of this observation and show the simulated spectrum in Figure 1b (red) that was calculated with a single species.

Notably, the line widths in completely deuterated solvent and in completely protonated solvent differ only slightly from each other, indicating that the broadening due to unresolved ^1H hyperfine couplings to solvent hydrogens is negligible in low-temperature ESE-detected EPR spectra. No difference in the A_{zz} value was observed between the deuterated and protonated sample mixture with a solvent ratio of $v/v = 50:50$ ($\epsilon = 65$). Comparing the solvent mixtures with higher (70 vol %, $\epsilon = 53$) and lower (30 vol %, $\epsilon = 77$) amounts of methanol, no variation of A_{zz} with solvent polarity is observed either. The low-field region of the ESE spectrum of the water-rich solvent mixture (70 vol % H_2O) is broadened, and a slightly higher g_{xx} -value (increased by 5×10^{-5}) is found. The best simulation for this sample is given after introduction of a second species with pronounced higher g_{xx} -value (4×10^{-4}). No differences for the g_{xx} -values of the mixtures with 50 vol % and 70 vol % methanol are observed, which indicates that the hydrogen bonding to NO is similar in these two solvent mixtures.

Mims ENDOR Measurements. The following color code is used in all figures and for all spectra: black marks the x -, red the y -, and green the z -direction in the nitroxide reference frame (Figure 1a). In Mims ENDOR, the intensity is modulated by a periodic dependence of the interpulse spacing τ , given by I_{ENDOR}

$\sim 1 - \cos(2\pi A\tau)$,⁴⁵ where τ denotes the pulse spacing between the last two $\pi/2$ pulses. An increased value for τ led to a symmetric narrowing of the spectra from both sides affecting mostly the width of the broadest coupling. This was most pronounced in ^2H measurements since large τ -values have been used for their detection (600 ns). Attempts to measure ^2H ENDOR with shorter τ values suffered from poor signal-to-noise (S/N) ratio. Hence, analysis of ^2H Mims ENDOR spectra is only given in a qualitative way.

In all Mims ENDOR spectra an intense peak is observed centered around the larmor frequency of the respective nucleus. Such matrix lines in ENDOR spectra are due to very weak hyperfine interactions of the unpaired electron with distant matrix nuclei and originate from simultaneous inversion of a large number of nuclear spins by the rf pulse.⁵⁶ The analysis of weakly coupled protons in the solvation shell is complicated, as these resonances overlap with the matrix peak. The largest hyperfine splitting observed in Mims-ENDOR spectra is $\sim 4.2\text{ MHz}$ (at $\pm 2.1\text{ MHz}$) for ^1H and $\sim 0.84\text{ MHz}$ (at $\pm 0.42\text{ MHz}$) for ^2H , both of which are still quite small (in particular, when compared to the Davies ENDOR results presented later). No further splittings with larger hf couplings were observed in spectra recorded with wider radio frequency sweep ranges.

For the solvent mixture $\text{CH}_3\text{OD}/\text{D}_2\text{O}$, other volume ratios with higher methanol (70 vol %, $\epsilon = 53$) and lower (30 vol %, $\epsilon = 77$) content were prepared. Their ^1H -Mims ENDOR spectra exhibit identical line shapes and only slight intensity variations for the different positions x , y , and z as compared to the sample with 50 vol % methanol in Figure 2 (data not shown). The mixture with low methanol content gave only poor S/N ratio in the ENDOR experiments but shows also the same trend upon variation of the observer field position.

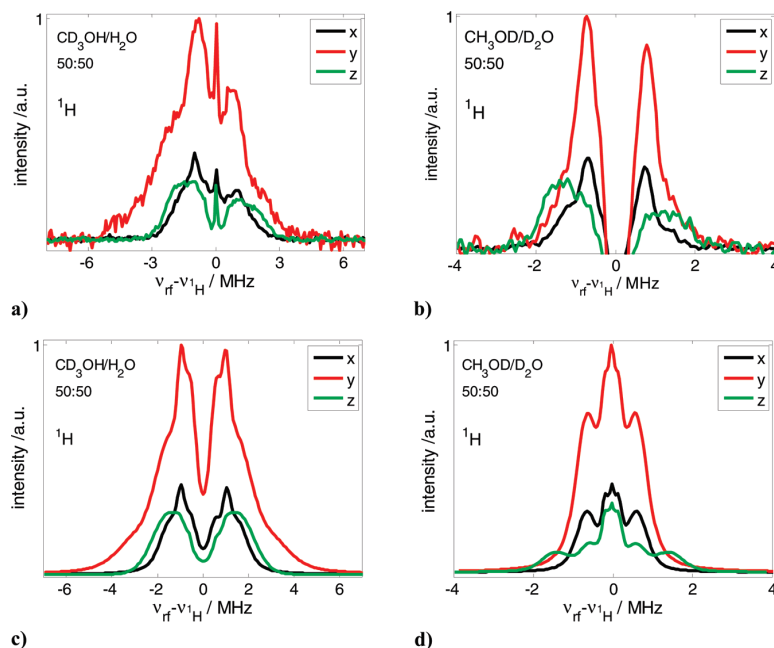


Figure 3. W-Band ^1H Davies ENDOR spectra of 2.5 mM Fremy's salt in frozen solution for the solvent mixture (a) $\text{CD}_3\text{OH}/\text{H}_2\text{O}$ and (b) $\text{CH}_3\text{OD}/\text{D}_2\text{O}$. Both mixtures contain 50 vol % methanol. The spectra were recorded at field positions corresponding to the canonical values of the \mathbf{g} -tensor g_{xx} (black), g_{yy} (red), and g_{zz} (green), as defined in Figure 1a. Experimental parameters: $T = 20$ K; MW inversion pulse, $t_{\pi} = 200$ ns; RF, $t_{\pi} = 20$ μs ; MW detection pulse, $t_{\pi/2} = 200$ ns; $\tau = 548$ ns. (c) ^1H ENDOR simulation of exchangeable protons in the sample mixture $\text{CD}_3\text{OH}/\text{H}_2\text{O}$. (d) Simulation of methyl protons in the mixture $\text{CH}_3\text{OD}/\text{D}_2\text{O}$. The spectra are normalized relative to the EPR spectral intensity at their field position B_{ENDOR} .

Davies ENDOR Measurements. Davies ENDOR spectra were only recorded for the ^1H isotope and shown in Figure 3 for the solvent mixtures with equal volume ratios $v/v = 50:50$ of methanol and water. Due to the weaker signal intensity (as compared to Mims ENDOR), it was impossible to record ^2H Davies ENDOR spectra within reasonable measurement time.

In Figure 3a, the orientation-dependent ^1H -Davies ENDOR spectra for the solvent mixture $\text{CD}_3\text{OH}/\text{H}_2\text{O}$ are shown. Along the molecular x -axis (black), the peaks at ± 1.1 MHz (splitting = 2.2 MHz) are the most prominent features in the spectrum. When changing the field position B_{ENDOR} to the molecular y -axis (red), this coupling is still observed, but a second one at ± 2.5 MHz (splitting = 5 MHz) and a very broad flank that extends out to ± 6 MHz appear, too. When changing the field B_{ENDOR} to match the molecular z -orientation, the broad flank disappears again, and the peaks at ± 2.5 MHz grow in intensity to now match the intensity of the peaks from the smallest splitting.

Indications of the larger couplings of exchangeable hydrogens found along the molecular y -position in Davies ENDOR spectra are already found in the ^2H Mims ENDOR spectrum of the mixture $\text{CH}_3\text{OD}/\text{D}_2\text{O}$ (Figure 2a, red line), but the poor S/N ratio does not allow as precise an assignment as in the Davies ENDOR case.

The situation is clearly different for the methyl protons. In this case (Figure 3b), the proton hyperfine couplings along the molecular x - and y -directions are almost identical (a coupling of less than 2 MHz with peaks at ± 1 MHz), while a larger, relatively broad hf coupling grows in intensity when measuring along the molecular z -direction (splitting range of 2.5–4 MHz, the broad peaks are centered at ± 1.5 MHz). The spectra in Figure 3b suffer from a blind spot around the Larmor frequency, which makes it impossible to analyze small hf couplings. Note

that this blind spot cannot fully explain the signal in Figure 3b turning negative. At this point, we refrain from interpreting which other effects may contribute to this observation that hampers analysis of small hf couplings in these Davies ENDOR spectra. In fact, the ^1H Davies ENDOR spectra (Figure 3b) of the solvent mixture $\text{CH}_3\text{OD}/\text{D}_2\text{O}$ qualitatively show the same features as the corresponding Mims ENDOR spectra (Figure 2b); however, Davies ENDOR spectra suffer from a “central” blind spot, while Mims ENDOR spectra suffer from an “outer” blind spot that scales down the largest hf coupling.

This can be seen best at the molecular z -direction (green lines): in the Mims ENDOR spectrum, the outer flank reaches the baseline at ± 2.0 MHz, while the Davies ENDOR spectra extend to ± 2.4 MHz. This has direct consequences for the chosen simulation parameters, which are explained in the next section.

ENDOR Simulation. The chemically distinct methyl protons and exchangeable protons could be measured and also simulated individually. Since the ^1H Davies ENDOR spectra for *exchangeable protons* $\text{CD}_3\text{OH}/\text{H}_2\text{O}$ (Figure 3a) show more distinct features than the respective Mims ENDOR spectra (Figure 2d), the former was chosen for the simulations. A set of couplings with independent line widths were defined, and the \mathbf{g} -tensor principal values were taken from the simulated EPR spectrum. For simulation of the ^1H ENDOR spectra (Figure 3c), three proton couplings had to be employed to fit the experimental results for the x - and z -position. The matrix peak was neglected (for clarity) but can be included with an isotropic hfc of 10^{-4} MHz. The pronounced feature in the experimental spectrum at the x -orientation is assigned to an hf coupling of $a_{\text{iso}}(1) = 1.13$ MHz. The hf couplings $a_{\text{iso}}(2) = 2.04$ MHz and $a_{\text{iso}}(3) = 3.04$ MHz together describe the flank of the spectra. These couplings were found to be present in all three orientations with

different weighting factors. Only the y -position could not be simulated successfully with these three hf couplings. As can be seen in the red spectrum in Figure 2a, the very broad shoulder on the left wing requires an additional hf coupling. This was found to be $a_{\text{iso}}(6) = 6.20$ MHz. This is by far the strongest coupling found in our measurements and simulations and is only present in this sample mixture and at the molecular y -position. This coupling cannot be found in the corresponding ^1H Mims ENDOR spectra for the following reason: Assuming the maximum detectable hf coupling in Mims ENDOR to be $A_{\text{max}} \sim 1/(2\tau)$,⁴⁵ with $\tau = 172$ ns, one gets an approximate maximum detectable hf coupling of $A_{\text{max}} \sim 2.9$ MHz for this experiment. Hence, this spectrum suffers from a blind spot region at this value.

The blind spots in the Mims ENDOR spectra mostly affect the outer flank, while the blind spots in the Davies ENDOR spectra affect the central region around the Larmor frequency. Therefore, the simulation of *methyl protons* $\text{CH}_3\text{OD}/\text{D}_2\text{O}$ was performed by combining both spectral features from Davies and Mims ENDOR spectra that do not suffer from the blind spot behavior. This means that the small hf couplings (along the x - and y -molecular direction) were derived from the ^1H Mims ENDOR spectra (Figure 2b, black and red line) and the large hfc that becomes apparent at the molecular z -position from the corresponding ^1H Davies ENDOR spectrum (Figure 3b, green line). The small hf couplings were found to be nearly isotropic with $a_{\text{iso}}(1) = 0.33$ MHz and $a_{\text{iso}}(2) = 1.22$ MHz. The larger hf coupling was simulated with a purely anisotropic hfc $\mathbf{A} = \mathbf{T} = [-T, -T, 2T] = [-1.6, -1.6, 3.2]$ MHz ± 0.2 MHz. In a very simplified picture, from the component $T = 1.6$ MHz, a distance of $r = 3.5 \pm 0.1$ Å can be calculated within the point-dipole approximation according to eq 3.⁴⁵

In the ENDOR simulations, it was found that convolution with a Gaussian and a Lorentzian function (Voigtian) with a larger Gaussian fwhm gives the best fits to the experimental spectra, indicating inhomogeneous broadening at all positions. Note that the asymmetry observed in the high-field ENDOR spectra may well stem from the cross- and/or nuclear-relaxation times being longer than the repetition times used in the experiments,⁵⁷ which was not considered in the simulation.

Molecular Dynamics Simulation. The solvation of the FS dianion by water and methanol was modeled computationally by means of molecular dynamics simulations using classical force fields. A trajectory of 10 ns duration was generated at a temperature of 300 K to extensively sample the available phase space for this binary solvent mixture. The low-temperature solvation configurations corresponding to the experimental situation were obtained by repeatedly annealing snapshots (200 in total) which were extracted from the 300 K-trajectory at regular intervals.

In the optimized geometry of the FS dianion (Figure 5), a small deviation from a planar hybridization geometry at the nitrogen atom is found with a N–O bond length of 1.283 Å. This is in excellent agreement with the 1.284 Å found by X-ray diffraction.⁵⁸

For ionic solutes, the question of ion pairing in a given solvent is often a matter of concern. Thus, we have monitored the distances between the K^+ ions and the dianion in our simulations. In the initial configuration of the system, the dianionic salt was set up as a tight ion pair with the two potassium cations. Within 400 ps, both cations diffused away to a distance of 9 Å from the salt. Only four times during the whole trajectory of 10 ns, a potassium ion diffused back to the dianion. The lifetime of this ion pair never exceeded 100 ps. Thus, ion pairing is

TABLE 2: Calculated Coordination Numbers for the Different Oxygen Species Present in Fremy's Salt

	H_2O	$\text{HO}-\text{CH}_3$
sulfonate–oxygen	1.55	0.47
nitroxide–oxygen	0.62	0.13

unlikely to be a significant issue in this system, especially when considering that our simulated concentration of 25 mM is about 10-fold higher than in experiment. Interestingly, this corresponds well with hyperfine sublevel correlation (HYSCORE) spectroscopy (see Supporting Information) in which hyperfine interaction between the radical and ^{39}K was only observed with larger volume ratios of methanol.

Three distinct types of protons can be analyzed with respect to their interactions with FS: the water protons, the methanol hydroxyl (or alcohol) protons, and the nonexchangeable protons of the hydrophobic methyl group. In principle, all sulfonate oxygens and the nitroxide oxygens in FS can interact as hydrogen bond acceptors with the solvent. Table 2 lists the coordination numbers of the acceptor oxygens of the solvated dianion obtained by integrating the corresponding radial distribution functions (RDF) $g_{\text{OH}}(r)$ up to the first minimum. Each of the electron-rich sulfonate oxygens is fully solvated with two hydrogen bonds. In contrast to this, the nitroxide oxygen has a coordination number of only 0.75. This reflects the fact that this oxygen is sterically almost inaccessible, being flanked from both sides with sulfonate groups. This effect is also observable directly from the RDFs (data not shown).

The coordination of the nitroxide oxygen by water protons is almost five times larger than that by methanol, which approximately equals the statistical proton ratio in our simulation box (4.49). The slight preference for water solvation relative to the statistical ratio is probably due to the smaller size of the water molecules, in combination with the mentioned sterical hindrance by the sulfonate groups.

To gain further insight into the solvent structure, we have plotted the angular distribution functions of the different proton species relative to the NO bond in Figure 4. The angle θ is measured between the NO bond axis and the vector pointing from the NO bond center to the solvating proton. For the calculation of these angular distribution functions, solvent protons up to a certain radial cutoff value were considered. The plots in Figure 4 show distribution functions for four different cutoff values.

Regarding the methyl protons, there is a clear preference for $\theta = 90^\circ$ at short distances (up to 3 Å), which corresponds to the direction directly above the molecular plane. There is virtually no density in the direction of the NO bond ($\theta = 0^\circ$) because the size of the methyl group results in a strong sterical hindrance. At 3.5 Å, the angular distribution has reached an almost uniform shape.

Regarding the water protons, only little differences in the amplitudes of the distribution functions at small angles $\theta < 50^\circ$ between cutoff values of 2.5–3.0 Å are observed. This indicates that most of the hydrogen-bonded protons are located at distances shorter than 2.5 Å relative to the NO bond center. At a cutoff of 3.0 Å, a strong peak at $\theta = 60^\circ$ appears, which can be attributed to the solvation of the sulfonate groups. Both these features are also found for the alcoholic hydrogen, except that the distribution function vanishes for very small angles $\theta < 15^\circ$. This again illustrates the sterical hindrance caused by the bulky sulfonates and possibly also the methyl group of methanol.

The picture described above was obtained from analyzing the solvation structure at low temperature. Qualitatively, the

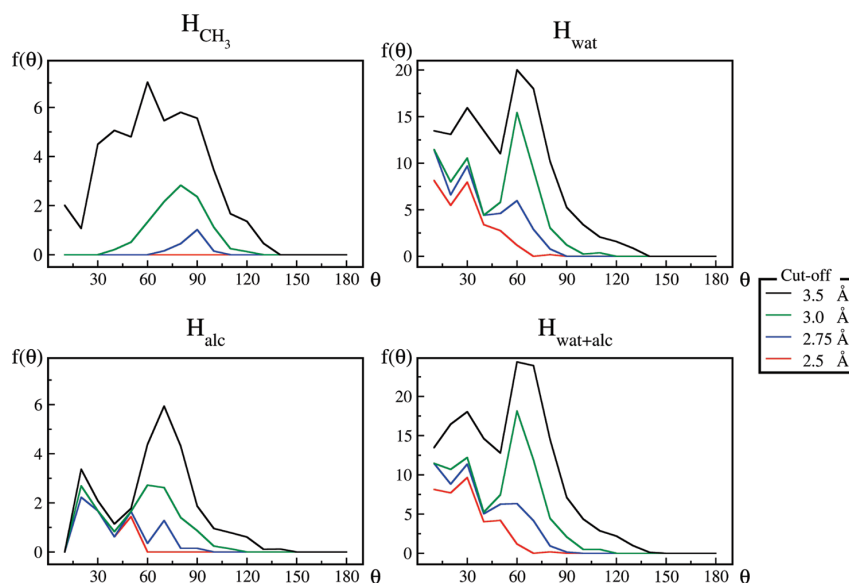


Figure 4. Angular distribution functions of the different proton species relative to the NO bond (water proton, H_{wat} ; alcoholic protons, H_{alc} ; methyl protons, H_{met} ; exchangeable protons, $H_{\text{wat}} + H_{\text{alc}}$). The angle θ is measured between the NO bond axis and the vector pointing from the NO bond center to the solvating proton. In each plot, protons up to a four different radial cutoff value were considered. Note that up to 3.5 Å, an approach from $\theta = 180$ is sterically impossible for all solvent protons.

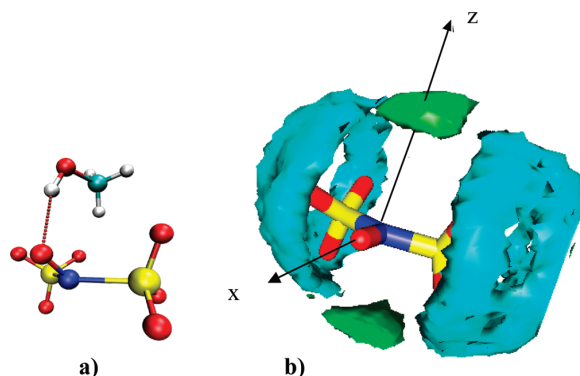


Figure 5. Solvated Frey's salt. Nitrogen atoms are shown in blue, sulfur atoms in yellow, and oxygen atoms in red. (a) Simulation snapshot from the MD run showing a situation in which one methanol-OH group is hydrogen-bonded to the NO group. (b) Isosurface of the spatial distribution function of the exchangeable protons (cyan) and hydrophobic methyl protons (green) in $\text{CH}_3\text{OH}/\text{H}_2\text{O}$ ($v/v = 50:50$). Along the z -axis of the molecular frame, methyl protons are accumulated, whereas the charged sulfonate groups are strongly hydrogen bonded. A cutoff of 3 Å was used for this picture.

same pattern of solvation exists also at room temperature, and the trend observed in Figure 5—as expected—is slightly more pronounced at low temperature.

The prediction of the actual ENDOR line shape from the simulation data would require the statistical distribution of the A-tensors of all protons in proximity of the salt for a large number of annealed snapshots. While this calculation is in principle possible,⁵⁹ it requires an extensive additional sampling of our trajectories with quantum-chemical methods, which is beyond the scope of the present work. Here, we restrict ourselves to the geometric distribution of the solvent protons around FS, which is directly available from the MD trajectory. In analogy to this, we do not consider nuclear quantum effects, i.e., the broadening of the proton probability density with respect to the

point particle representation. While there is an ongoing discussion on whether these effects lead to a somewhat more or somewhat less structured hydrogen bonding network,^{60–64} we believe that the consequences on the final solvation structure in a complex liquid will not be dramatic.

4. Discussion

Solvation Shell around Frey's Salt Dianions. When discussing the combined ENDOR and MD results, one should always be aware that the ENDOR measurements depict a complete ensemble of $\sim 10^{15}$ Frey's salt ions and their solvation shells in the solvent mixtures. Since it is highly unlikely that all FS molecules have the exact same solvation shell, the observable splittings shown in Figures 2 and 3 and their respective simulations only represent a part of the ensemble. Hence, one main source of spectroscopic information is the interpretation of differences between the exchangeable and methyl protons in the ENDOR and MD data.

When a solute ion such as FS is added to a methanol/water mixture, it is reasonable to assume distortion of the hydrogen-bonded network as a response to the existence of the solute ion. Water is a two H-bond donor and two H-bond acceptor, whereas methanol with its single hydroxyl H-atom is only a single H-bond donor and (theoretically) a two H-bond acceptor. When dissolving Frey's salt, the two sulfonate groups mainly act as hydrogen-bond acceptors, which force some molecules of water into close contact also with the N–O. This can be seen in the ^1H Davies ENDOR spectra for the y -orientation (Figure 3a, red spectrum). Thus, the strongest proton hf coupling with $a_{\text{iso}}(6) = 6.20$ MHz can be assigned to hydrogen-bonded water at the sulfonate groups since hydrogen bonding to one of the adjacent sulfonate groups allows protons to approach the NO group closest. The ENDOR measurements are in agreement with the MD simulation that found a coordination number of two for the sulfonate oxygen atoms and the closest approach (down to 2.2 Å) by water and methanol-OH protons to the NO group at small angles (Figure 4a and b). Interestingly, results

from Mims and Davies ENDOR measurements along the x -position suggest that the N–O bond is not involved in too many hydrogen bonds. EPR spectral simulations indicate that there potentially is g -strain in the x -direction (Figure 1b), indicating that statistically seen there will be some molecules that are hydrogen bonded along N–O \cdots H–OH, but by summation over the small amount of selected orientations, this small number of H-bonded molecules is not enough to notably contribute to an ENDOR signal. This result also manifests itself in the MD simulations. The coordination number for the nitroxide group is much smaller than for the sulfonate groups, showing less hydrogen bonds along the molecular x -axis. When inspecting the low-field region of the ESE-detected EPR spectra of the different samples, we only observed a shift of the g_{xx} -value in the water-rich solvent mixture with 70 vol % water. Due to the smaller size of water compared to methanol, it may approach the NO group closer, and the hydrogen-bonding capability is much higher for water. The other two solvent compositions (50 and 70 vol % MeOH) show no shifts, which indicates that the hydrogen bonding to NO is similar in both.

The respective methyl proton splittings in the solvent mixtures show the same features for Mims (Figure 3a) and Davies (Figure 4b) ENDOR measurements. Here, two smaller hfc's are found at each molecular orientation and are assigned to more distant methanol molecules for which we cannot get distance orientation information. From the largest hfc, which arises along the molecular z -axis (parallel to the SOMO) and can be simulated as being purely anisotropic, a distance of 3.5 ± 0.1 Å can be extracted. Thus, methyl protons approach closest from “bottom” and “top” of the FS molecule's (approximate) plane spanned by O–N–(S)₂.

Using a sum of the proton “densities” from an ensemble of snapshots from the MD simulations, one can not only visualize but also understand the results of the MD simulations and the ENDOR experiments (Figure 5a) and draw a molecular picture of the solvation around FS. Figure 5b shows the chemically different types of protons around the probe molecule (hydrophobic methyl protons, green; exchangeable protons from water and the hydroxyl groups, cyan). The shortest distance for methyl protons is found to be 2.8 Å along the long axis of the SOMO (Figure 1a). The ENDOR experiments were performed at 20 K, where methyl group rotation is still active⁶⁵ and the three equivalent protons contribute to a (hypothetical) averaged ¹H signal. Taking a CH bond length of 1.093 Å and a HCH angle of 109.3°,⁶⁶ one can calculate that the distance from the center of the NO group to the “averaged” proton is 1.03 Å longer than the distance to the closest proton (assuming that this closest proton is pointing toward the NO group). Since in pulse ENDOR experiments at 20 K one measures an averaged proton–electron distance and setting the closest proton–electron distance to 2.8 Å, as found by MD simulation, one gets an averaged distance of 3.8 ± 0.1 Å for the experiments, which is—considering the broad ensemble of solvation situations—in good agreement with the 3.5 Å found from the simplified calculation from the ENDOR experiments. We refrain from assigning a “true” proton–electron distance since the underlying one has the complicated situation that there is a distribution of hf couplings that are weighted by $1/r^3$ and these hyperfine responses are further weighted by either the Mims or Davies ENDOR response functions.

The preferential arrangement of the methyl groups above and below the NO bond is due to two forces: First, in this way the strong H-bonded network around the two sulfonate groups (as seen in the MD simulations) is less disturbed. Methanol can

act as one H-bond donor, and if the methanol–OH group is H-bonded to one of the highly hydrophilic sulfonate groups, placing the methyl group at the sulfonate group (and hence reducing the number of H-bonds) would be energetically unfavorable. The second argument is of steric nature. The largest “free” space for the (in relation to any other components in the solvent mixtures) bulky methyl groups is simply given at these positions of the molecule due to the sulfonate groups. Thus, this specific solvation situation is found to be due to an interplay between electrostatic, hydrogen-bonding, and steric effects.

The microheterogeneity of the binary solvent structure without solute molecules can be assumed to be highly similar in all our cases, as proposed by Zhao et al.⁶⁷ All our tested methanol molar ratios are in a composition region, in which methanol–water associates of one molecule of methanol with two molecules of water have been observed by IR.⁶⁷ When considering our experimental findings, this indicates that also in the case with solute molecules the same solvation characteristics are found for all volume ratios studied here. This, in turn, suggests that in a broad range of compositions the solute molecules FS (or many of them, at least) “force” the water and methanol molecules into a solvation shell that resembles the one found in our study and depicted in Figure 5b.

5. Conclusions and Outlook

The molecular picture of the solvation around Fremy's salt in a 50:50 (v/v) mixture of methanol and water, which is derived from the MD simulations, is in full agreement with our ENDOR results and is summarized in Figure 5b. Both exchangeable species (water and hydroxyl protons) are able to establish hydrogen bonds to the FS dianion with an angular distribution that reflects the sterical hindrance of the NO hydrogen-bond acceptor site by the sulfonate groups. Hence, exchangeable protons come in closest contact with the NO moiety along the molecular y -axis of the probe molecule. If the methanol–OH group (instead of water) is hydrogen bonded to the sulfonate groups, it is energetically favorable to *not* place the methyl group at the sulfonate group, as this would disturb the existing H-bond network and reduce the number of H-bonds. It is thus favorable to place the methyl groups on the “top” and “bottom” of the (approximate) plane spanned by O–N–(S)₂. Also, the largest “free” space for the methyl groups is given at these positions of the molecule due to the sulfonate groups. Thus, the preferential arrangement of methyl groups along the molecular z -direction of the nitroxide can be explained by the interplay of *electrostatic and hydrogen-bonding* (H-bonds around sulfonate groups) and *steric* (bulky methyl group) effects.

The elucidation of the microscopic solvation of a small probe molecule in binary solvent mixtures represents the first step for understanding the interactions in more complex biochemical systems. In particular, this includes the potential perturbation of the H-bond network due to the presence of a spin probe.

Further work on variable mixing time (VMT) ENDOR^{68,69} is in progress to get information about the sign of the hyperfine coupling, which is important for the unambiguous determination of the isotropic and anisotropic parts of the interaction, and the approach will be extended to other solvents and solute molecules.

Acknowledgment. We thank Christian Bauer for technical support, Matthias Junk for his help in spectral simulations, and Hans W. Spiess for helpful discussions. This work was financially supported by the Deutsche Forschungsgemeinschaft (DFG) under grants number HI 1094/2-1, Se 1008/5, and Se 1008/6. Support from a RISE fellowship of the German

Academic Exchange Service (DAAD) is gratefully acknowledged (B.Z.).

Supporting Information Available: Details of the HYSORE experiments for the detection of ^{39}K hyperfine couplings. This material is available free of charge via the Internet at <http://pubs.acs.org>.

References and Notes

- Reichardt, C. *Solvents and Solvent Effects in Organic Chemistry*, 2nd ed.; VCH: Weinheim, 1988.
- Bagotsky, S. *Fundamentals of Electrochemistry*, 2nd ed.; Wiley-Interscience: NJ, 2006.
- Marcus, Y. *Solvent Mixtures Properties and Selective Solvation*; Marcel Dekker: Basel, 2002.
- Ben-Naim, A. *J. Phys. Chem.* **1989**, 93, 3809–3813.
- Wahab, A.; Mahiuddin, S. *J. Solution Chem.* **2005**, 34, 537–560.
- Chatterjee, P.; Bagchi, S. *J. Chem. Soc., Faraday Trans.* **1990**, 86, 1785–1789.
- Hefter, G. *Pure Appl. Chem.* **2005**, 77, 605–617.
- Hawlicka, E.; Swiatla-Wojcik, D. *Chem. Phys.* **1995**, 195, 221–233.
- Bujnicka, K.; Hawlicka, E. *J. Mol. Liq.* **2006**, 125, 151–157.
- Sakurai, M.; Yoshimori, A. *Chem. Phys. Lett.* **2003**, 371, 23–28.
- Tongraar, A.; Rode, B. M. *Phys. Chem. Chem. Phys.* **2004**, 6, 411–416.
- Attanasio, D. *J. Phys. Chem.* **1986**, 90, 4952–4957.
- Mustafi, D.; Makinen, M. W. *Inorg. Chem.* **1988**, 27, 3360–3368.
- van Willigen, H. *Chem. Phys. Lett.* **1979**, 65, 490–493.
- van Willigen, H. *J. Magn. Reson.* **1980**, 39, 37–46.
- Feher, G. *Phys. Rev.* **1956**, 103, 834.
- Steinhoff, H.-J.; Savitsky, A.; Wegener, C.; et al. *Biochim. Biophys. Acta, Bioenerg.* **2000**, 1457, 253–262.
- Steinhoff, H.-J. *Biol. Chem.* **2005**, 385, 913–920.
- Weil, J. A.; Bolton, J. R.; Wertz, J. E. *Electron Paramagnetic Resonance*; Wiley: New York, 1994.
- Bales, B. L.; Wajnberg, E.; Nascimento, O. R. *J. Magn. Reson., Ser. A* **1996**, 118, 227–233.
- Zielonka, J.; Zhao, H.; Xu, Y.; et al. *Free Radical Biol. Med.* **2005**, 39, 853–863.
- Liu, Z.-L.; Han, Z.-X.; Chen, P.; et al. *Chem. Phys. Lipids* **1990**, 56, 73–80.
- Hinderberger, D.; Spiess, H. W.; Jeschke, G. *Europhys. Lett.* **2005**, 70, 102–108.
- Hinderberger, D.; Spiess, H. W.; Jeschke, G. *J. Phys. Chem. B* **2004**, 108, 3698–3704.
- Hinderberger, D.; Schmelz, O.; Rehahn, M.; et al. *Angew. Chem.* **2004**, 116, 4716–4721.
- Prandolini, M. J.; Denysenkov, V. P.; Gafurov, M.; et al. *J. Am. Chem. Soc.* **2009**, 131, 6090–6092.
- Nayak, S. P.; Gowda, B. T. *J. Phys. Org. Chem.* **1992**, 5, 755–763.
- Mims, W. B. *Proc. R. Soc. (London), Ser. A* **1965**, 283, 452–457.
- Davies, E. R. *Phys. Lett. A* **1974**, 47, 1–2.
- Kuharski, R. A.; Rossky, P. J. *J. Chem. Phys.* **1985**, 82, 5164–5177.
- Tomberli, B.; Egelstaff, P. A.; Benmore, C. J.; et al. *J. Phys. Condens. Matter* **2001**, 13, 11421–11434.
- Moser, W.; Howie, R. A. *J. Chem. Soc. A* **1986**, 3039–3043.
- Wilson, B. J.; Ritter, D. M. *Inorg. Chem.* **1963**, 2, 974–978.
- Wilson, B. J.; Hayes, J. M.; Durbin, J. A. *Inorg. Chem.* **1976**, 15, 1702–1704.
- Goldman, S. A.; Bruno, G. V.; Freed, J. H. *J. Chem. Phys.* **1973**, 59, 3071–3091.
- Goldman, S. A.; Bruno, G. V.; Polnaszek, C. F.; et al. *J. Chem. Phys.* **1972**, 56, 716–735.
- Atherton, N. M.; Brustolon, M. *Mol. Phys.* **1976**, 32, 23–31.
- Mikhail, S. Z.; Kimel, W. R. *J. Chem. Eng. Data* **1961**, 6, 533–537.
- Static Dielectric Constants of Pure Liquids and Binary Liquid Mixtures. In *Landolt-Börnstein - Group IV Physical Chemistry Numerical Data and Functional Relationships in Science and Technology*; Landolt-Börnstein, Ed.; Springer: Berlin Heidelberg; Vol. 17, 2008.
- Smirnova, T. I.; Smirnov, A. I. High-Field ESR Spectroscopy in Membrane and Protein Biophysics. In *Biological Magnetic Resonance*; Hemminga, M. A.; Berliner, L. J., Eds.; Springer: New York, 2007; Vol. 27, pp 165–251.
- Makinen, M. W. *Spectrochim. Acta, Part A* **1998**, 54, 2269–2281.
- Rist, G. H.; Hyde, J. S. *J. Chem. Phys.* **1970**, 52, 4633–4643.
- Hoffman, B. M.; Ronald, A. V.; Martinsen, J. *J. Magn. Reson.* **1985**, 62, 537–542.
- Hoffman, B. M.; Ronald, A. V.; Martinsen, J. *J. Magn. Reson.* **1984**, 59, 110–123.
- Schweiger, A.; Jeschke, G. *Principles of Pulse Electron Paramagnetic Resonance*; Oxford University Press: New York, 2001.
- Stoll, S.; Schweiger, A. *J. Magn. Reson.* **2006**, 178, 42–55.
- Hess, B.; Kutzner, C.; van der Spoel, D.; et al. *J. Chem. Theory Comput.* **2008**, 4, 435.
- Nosé, S. *Mol. Phys.* **1984**, 52, 255.
- Hoover, W. G. *Phys. Rev. A* **1985**, 31, 1695.
- Darden, T.; York, D.; Pedersen, L. *J. Chem. Phys.* **1993**, 98, 10089.
- Essmann, U.; Perera, L.; Berkowitz, M. L.; et al. *J. Chem. Phys.* **1995**, 103, 8577.
- Jorgensen, W. L.; Maxwell, D. S.; Tirado-Rives, J. *J. Am. Chem. Soc.* **1996**, 118, 11225.
- Jorgensen, W. L.; Chandrasekhar, J.; Madura, J. D. *J. Chem. Phys.* **1983**, 79, 926.
- Frisch, M. J.; Trucks, G. W.; Schlegel, H. B.; Scuseria, G. E.; Robb, M. A.; Cheeseman, J. R.; Montgomery, J. A., Jr.; Vreven, T.; Kudin, K. N.; Burant, J. C.; Millam, J. M.; Iyengar, S. S.; Tomasi, J.; Barone, V.; Mennucci, B.; Cossi, M.; Scalmani, G.; Rega, N.; Petersson, G. A.; Nakatsuji, H.; Hada, M.; Ehara, M.; Toyota, K.; Fukuda, R.; Hasegawa, J.; Ishida, M.; Nakajima, T.; Honda, Y.; Kitao, O.; Nakai, H.; Klene, M.; Li, X.; Knox, J. E.; Hratchian, H. P.; Cross, J. B.; Bakken, V.; Adamo, C.; Jaramillo, J.; Gomperts, R.; Stratmann, R. E.; Yazyev, O.; Austin, A. J.; Cammi, R.; Pomelli, C.; Ochterski, J. W.; Ayala, P. Y.; Morokuma, K.; Voth, G. A.; Salvador, P.; Dannenberg, J. J.; Zakrzewski, V. G.; Dapprich, S.; Daniels, A. D.; Strain, M. C.; Farkas, O.; Malick, D. K.; Rabuck, A. D.; Raghavachari, K.; Foresman, J. B.; Ortiz, J. V.; Cui, Q.; Baboul, A. G.; Clifford, S.; Cioslowski, J.; Stefanov, B. B.; Liu, G.; Liashenko, A.; Piskorz, P.; Komaromi, I.; Martin, R. L.; Fox, D. J.; Keith, T.; Al-Laham, M. A.; Peng, C. Y.; Nanayakkara, A.; Challacombe, M.; Gill, P. M. W.; Johnson, B.; Chen, W.; Wong, M. W.; Gonzalez, C.; Pople, J. A. *Gaussian 03*, revision C.02; Gaussian, Inc.: Wallingford, CT, 2004.
- Bayly, C. I.; Cieplak, P.; Cornell, W.; et al. *J. Phys. Chem.* **1993**, 97, 10269–10280.
- Astashkin, A. V.; Kawamori, A. *J. Magn. Reson.* **1998**, 135, 406–417.
- Epel, B.; Pöpl, A.; Manikandan, P.; et al. *J. Magn. Reson.* **2001**, 148, 388–397.
- Howie, R. A.; Glasser, L. S. D.; Moser, W. *J. Chem. Soc. A* **1986**, 3043–3047.
- Erickson, R. *J. Chem. Phys.* **1996**, 202, 263–275.
- Morrone, J. A.; Car, R. *Phys. Rev. Lett.* **2008**, 101, 017801.
- Chen, B.; Ivanov, I.; Klein, M. L.; et al. *Phys. Rev. Lett.* **2003**, 91, 215503.
- Marx, D.; Tuckerman, M. E.; Parrinello, M. *J. Phys. Condens. Matter* **2000**, 12, A153–A159.
- Morrone, J. A.; Srinivasan, V.; Sebastiani, D.; et al. *J. Chem. Phys.* **2007**, 126, 234504–9.
- Hayes, R. L.; Paddison, S. J.; Tuckerman, M. E. *J. Phys. Chem. B* **2009**, 113, 16574–16589.
- McBrierty, V. J. *Polymer* **1974**, 15, 503–520.
- Ivash, E. V.; Dennison, D. M. *J. Chem. Phys.* **1953**, 21, 1804–1816.
- Zhao, Z.; Malinowski, E. R. *Anal. Chem.* **1998**, 71, 602–608.
- Bennebroek, M. T.; Schmidt, J. *J. Magn. Reson.* **1997**, 128, 199–206.
- Epel, B.; Manikandan, P.; Kroneck, P.; et al. *Appl. Magn. Reson.* **2001**, 21, 287–297.

JP910335T

Chapter 5

Paper II

First principles calculation of inhomogeneous broadening in solid-state cw-EPR spectroscopy

Hossam Elgabarty, Milian Wolff, Adrian Glaubitz, Dariush Hinderberger, and Daniel Sebastiani

Phys. Chem. Chem. Phys., 2013.

Reproduced by permission of the PCCP Owner Societies.

<http://dx.doi.org/10.1039/C3CP51938D>

First principles calculation of inhomogeneous broadening in solid-state cw-EPR spectroscopy

Hossam Elgabarty,^{ac} Milian Wolff,^a Adrian Glaubitz,^a Dariush Hinderberger,^d and Daniel Sebastiani^{*b}

Received Xth XXXXXXXXXX 20XX, Accepted Xth XXXXXXXXXX 20XX

First published on the web Xth XXXXXXXXXX 200X

DOI: 10.1039/b000000x

We present a scheme for the first-principles calculation of lineshapes for continuous-wave-EPR spectroscopy (cw-EPR) of spin centers in complex chemical environments. We specifically focus on poorly-characterized systems, e.g. powders and frozen glasses with variable microsolvation structures. Our approach is based on ab-initio molecular dynamics simulations and ab-initio calculations of the ensemble of g- and A-tensors along the trajectory. The method incorporates temperature effects as well as the full anharmonicity of the intra- and intermolecular degrees of freedom of the system. We apply this scheme to compute the lineshape of a prototypical spin probe, the nitrosodisulfonate dianionic radical (Fremy's salt), dissolved in a 50:50 mixture of water and methanol. We are able to determine the specific effect of variations of local solvent composition and microsolvation structure on the cw-EPR lineshape. Our molecular dynamics reveal a highly anisotropic solvation structure with distinct spatial preferences for water and methanol around Fremy's salt that can be traced back to a combination of steric and polar influences. The overall solvation structure and conformational preferences of Fremy's salt as found in our MD simulations agree very well with the results obtained from EPR and orientation-selective ENDOR spectroscopy performed on the frozen glass. The simulated EPR lineshapes show good agreement with the experimental spectra. When combined with our MD results, they characterize the lineshape dependence on local morphological fluctuations.

1 Introduction

The determination of the detailed microscopic structure and dynamics of complex aqueous solutions is still a challenge for modern physics and chemistry. Unlike the situation in crystalline systems, where scattering experiments can provide very accurate atomic coordinates, aqueous systems lack the required long-range order, which limits the applicability of these scattering techniques. Electron paramagnetic resonance (EPR) is able to probe the local structure around an open shell system without the need for long-range order, and at the same time with high sensitivity to the local chemical environment. The two observables from an EPR experiment — the **A-tensor** and the **g-tensor** — are well known to be highly sensitive to local environmental changes like solvent polarity and fluctuations in the hydrogen bonding network.^{1,2} However, the interpretation of the rich and detailed information presented by

EPR spectroscopy has always been challenging and EPR spectroscopists are always looking for more elaborate tools to interpret their spectra, which basically comes down to assignment and interpretation of spin Hamiltonian parameters and of spectral lineshapes. The effective spin Hamiltonian represents the common grounds where results from theory and experiment converge. In this regard, the introduction of DFT was a turning point for the calculations of the spin Hamiltonian parameters, for it has been shown to provide remarkably accurate values at reasonable computational costs.^{3–10}

In a previous publication we have characterized the complex solvation environment and hydrogen bonding network around Fremy's salt (FS, see Fig. 1) in frozen water-methanol binary solvent by means of EPR/ENDOR spectroscopy and forcefield molecular dynamics simulations.¹¹ Like other nitroxide free radicals, FS is a chemically stable free radical, and its spectroscopic signatures are strongly sensitive to the chemical surroundings,¹² which makes it a suitable probe to study ionic solvation by EPR spectroscopy. In that work we had used classical MD simulations to help explain the experimental results. In particular, the solvation structure revealed by MD simulations was found to qualitatively agree with evidence coming from orientation-selective ENDOR.

Here, we present a more quantitative description of the solvation environment by means of ab initio MD simulations combined with first principles calculations of the spin Hamiltonian parameters. We also focus on how local disorder in the solvation structure in such a

^a Dahlem Center for Complex Quantum Systems (DCCQS), Physics Department, Freie Universität Berlin, Arnimallee 14, 14195 Berlin, Germany

^b Institute of Chemistry, Martin Luther University Halle-Wittenberg, Von-Danckelmann-Platz 4, 06120 Halle (Saale)

^c Johannes Gutenberg University Mainz, Institute of Physical Chemistry and Center for Computational Sciences, Staudinger Weg 7 D-55128 Mainz, Germany.

^d The Max Planck Institute for Polymer Research (MPIP), Ackermannweg 10, 55128 Mainz, Germany.

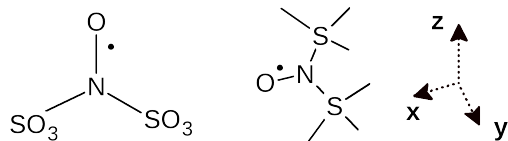


Fig. 1 Fremy's salt (FS). The axis system we use is depicted on the right side.

heterogenous frozen glass gives rise to the overall inhomogeneously broadened spectral envelope observed in continuous wave EPR spectroscopy (cw-EPR). To this end, we examine and correlate the variation in spin Hamiltonian parameters with both intermolecular (solvation) parameters as well as intramolecular ones (the geometry of FS itself).

Solid-state spectra are generally *inhomogeneously broadened*, which in the context of EPR refers to the situation where the ensemble of spins in the sample has a distribution of resonance frequencies and widths, with the individual widths being much less than the total width of the frequency distribution i.e. the distribution of the effective field at different spins is broader than the natural linewidth. This happens when the surrounding lattice dynamics is much slower than the resonance phenomenon, as exactly is in our case.^{13,14} In this situation the overall spectral line consists of many lines merged under one envelope. Although inhomogeneities of the static field and unresolved hyperfine coupling to solvent protons do play role in the line broadening, however, the two major non-relaxational sources of broadening in this case are g tensor and nitrogen A-tensor anisotropies.^{15,16} At each spin center, the values of the g and A-tensors are a complicated function of both intramolecular as well as intermolecular (solvation) factors, and it is usually the task of the spectroscopist to infer useful insight about the (possibly heterogenous) solvation structure and the geometry of the free radical from the average lineshape. Furthermore, in the case of a powder spectrum, the lineshape is an average over all the possible orientations of the tensors relative to the applied magnetic field.

A number of studies that combine ab initio MD simulations and theoretical EPR spectroscopy have come out.^{10,17,18} These studies indeed demonstrate the strength and utility of this approach. The previous studies were either focused on aqueous solutions or crystalline solids. Thus they either dealt with a system in the "motionally narrowed" limit or a system embedded a regular periodic lattice. To the best of our knowledge this is the first ab initio MD/EPR study of a heterogenous system in a frozen glassy state. Although methanol-water is probably one of the most simple binary solvents, the current general consensus is that it is far from being homogeneous. Experimental evidence and theoretical modeling suggest that these solutions are microheterogeneous, separating into methanol-rich regions and water-rich regions.¹⁹ When frozen, the mixture forms a glass which can be thought of as containing fixed randomly oriented spin centers lacking any spatial or orientational correlation. In such a heterogenous frozen glass, not only the relative orientation or distance between solvent molecules and FS may vary from site to site, but also the local numbers of water or methanol molecules also vary.

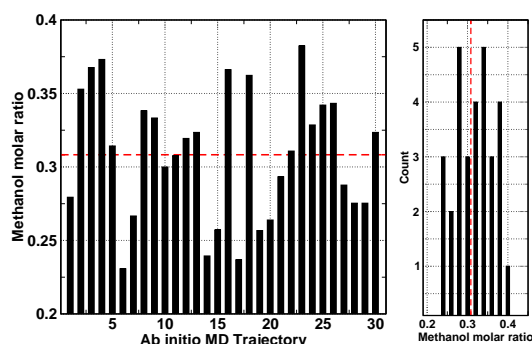


Fig. 3 Methanol molar ratio in each of the thirty ab initio MD trajectories. The dotted line marks the experimental (and classical MD) molar ratio.

Such poorly characterized systems present special challenges in EPR spectroscopy.²⁰ In order to capture such heterogeneity, and its effects on the inhomogeneously broadened EPR lineshape we have designed a simulation scheme as depicted in Fig. 2. 30 ab initio MD trajectories were started at regular time points from a classical MD trajectory. Each ab initio MD trajectory was run at a constant temperature of 300 K for 3.5 ps, followed by annealing down to 200 K in 3 ps, and a final rapid annealing down to 20 K in 1 ps. The final configuration from each of the annealed trajectories was used to compute spin Hamiltonian parameters (g and A-tensors, chemical shifts, quadrupolar couplings), and then finally used to construct an EPR lineshape. EPR lineshapes were computed via exact diagonalization of the spin Hamiltonian as described in the Computational Details.

2 Computational details

MD Simulations. From a 10 ns classical MD trajectory,¹¹ 30 snapshots were extracted by uniform sampling. From each of them, a sub-cell containing FS and the first two solvation shells was extracted and used for subsequent ab initio MD simulations (Fig. 2). In the large simulation cell the methanol molar ratio (0.308) corresponds to a 50:50 volume ratio at room temperature. In the 30 sub-cells the methanol molar ratio was found to vary between 0.23 to 0.38, with an average of 0.309 (Fig. 3).

Ab initio MD simulations were performed with CP2K²¹ using the Gaussian and plane waves (GPW) method with a DZ-MOLOPT-SR basis set²² and a planewave density cutoff of 320 Ry. The PBE functional²³ was used together with the Grimme D2 dispersion correction²⁴. After an initial isothermal relaxation period of 3.5 ps (300 K, CSV thermostat²⁵, $\tau = 500$ fs), the system was annealed in two steps: A slow annealing down to 220 K during 3 ps, followed by a faster annealing down to 20 K in 1 ps. Thus each of the 30 ab initio MD trajectories had a total length of 7.5 ps.

EPR Simulations. For calculations of EPR spectroscopic parameters, only FS and the first solvation shell were considered. The first solvation shell here is defined as any solvent molecule with at least one atom within three Angstroms from any FS atom. This choice

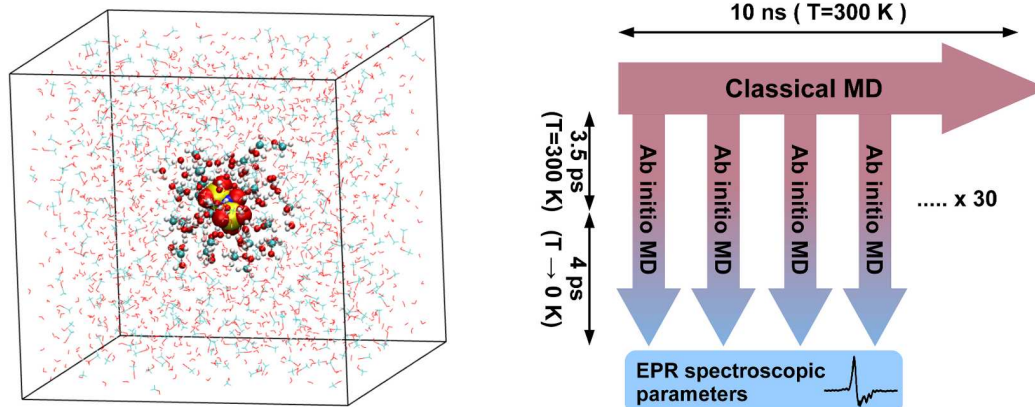


Fig. 2 Left: A snapshot of FS solvated in methanol and water taken from a classical (force field) trajectory. The central part depicted in spheres represent the sub-system that is extracted for ab initio MD. Right: Simulation scheme.

was based on an explicit calculation of the target quantities at various cluster sizes up to full periodic boundary conditions. Three different setups were used for the calculation of EPR g-tensors (Table 1), all of them using the IGLO-III basis set²⁶. The setup employing CP2K used the all-electron GAPW method^{27,28}, and the Wavelet Poisson solver was used to decouple from periodic images.²⁹ A-tensors were computed in Orca^{9,30} using the PBE0 functional and the EPR-III basis set³¹. The validity of these setups, particularly regarding the choice of the exchange correlation functional and the basis set, has been validated in different previous studies.^{7–10,32} Additional core STO-basis functions were added to the Nitrogen atom of FS (CORE_DZ_ADF basis set in Orca). The inclusion of these was found to have a relatively weak (–3 MHz) but statistically significant influence on the value of the isotopic part of the hyperfine coupling. Statistical analyses were done using R,^{33–35} all the results reported as statistically significant have a p-values less than 0.001.

EPR spectral line shapes were simulated using a frequency domain approach via exact diagonalization of the spin Hamiltonian using our own C++ code. The Spin Hamiltonian included the following terms:

$$\mathcal{H} = \mu_B \mathbf{B}_0 \cdot \mathbf{g} \cdot \mathbf{S} + \sum_i \mathbf{S} \cdot \mathbf{A}_i \cdot \mathbf{I}_i - \mu_N \sum_i g_N \mathbf{I}_i \cdot \mathbf{B}_0 + \mathbf{I} \cdot \mathbf{Q} \cdot \mathbf{I}$$

Where the terms from left to right are the electron Zeeman term, the hyperfine coupling, the nuclear Zeeman terms, and the quadrupolar coupling (only for nitrogen). Only the five most strongly coupled solvent hydrogens were included in the simulation. Chemical shift anisotropy was ignored. Adaptive segmentation of the field values was implemented³⁷, and powder averaging was performed on a Lebdev 101 hemispherical grid^{38,39} (MPI-parallelized). We do not include an explicit relaxation term in the spin Hamiltonian, instead we account for the damping of the spin coherences (transverse relaxation) phenomenologically by convoluting the frequency domain spectrum with a decaying exponential.⁴⁰ The decision to include only the five most strongly coupled protons was based on lineshape

Coordinate	MD-Average (300 K)	Annealed
N - O	$1.275 \pm 0.024 \text{ \AA}$	1.272 Å
N - S	$1.858 \pm 0.063 \text{ \AA}$	1.843 Å
S - N - S	$121.4 \pm 4.1^\circ$	121.3°
N - O _N - S - S	$12.3 \pm 7.3^\circ$	13.2°

Table 2 MD-averaged internal coordinates of FS. The values for the improper angle are unsigned averages. The averages at 300 K were obtained by averaging over all the 300 K trajectories, while the annealed averages were obtained only from the configurations that were used to compute the spectroscopic parameters (i.e. last configuration from each trajectory).

simulations including up to 12 solvent protons, as inclusion of further protons did not have any impact on the lineshape when the phenomenological covolution width was set to 1 Gauss.

3 Results and Discussion

3.1 Solvation Dynamics of Fremy's Salt

Table 2 gives averaged internal coordinates of the solvated FS at 300 K and 20 K. The most interesting point here is possibly the improper torsional angle between FS nitrogen, the two sulfurs, and the nitroxy oxygen, which we find to be slightly off-planar. This agrees with the results previously reported by Hinderberger et al based on rotational diffusion tensors from the simulation of cw-EPR spectra.⁴¹

Regarding solvent distribution around FS, Fig. 4 shows the radial distribution function of the polar hydrogens around FS nitroxy oxygen at 300 K and at 20 K. At 300 K sulfonyl oxygens have a tighter and stronger solvation shell compared to the nitroxy oxygen (coordi-

	XC-functional	Gauge origin
Setup 1: Gaussian 09 ³⁶	PBE0	GIAO
Setup 2: Orca 2.9 ^{9,30}	PBE0	Center of electronic charge
Setup 3: CP2K (GAPW) ²⁸	PBE	CSGT

Table 1 The three setups used to compute the g-tensor

nation numbers 1.40 and 0.73 respectively). At 20 K, the solvation structure gets more ordered, with the coordination at the sulfonyl oxygens remaining exactly the same. In contrast, the coordination number at the nitroso oxygen increases to 1. Close inspection reveals that the first solvation shell in the latter case is in fact composed of two gaussians, centered at 1.83 Å and 2.05 Å (See inset of Fig. 4). This matches our previous findings from cw-EPR spectra for this system, where two different g_{xx} values were required to fit the low-field end of the experimental spectrum to an empirical spin Hamiltonian.

Fig. 5 shows the spatial distribution of methyl hydrogens around FS, upto a cutoff distance of 3.5 Å. The RDF and the SDF combined give a concrete picture which closely matches previous theoretical and experimental EPR and orientation-selective ENDOR findings.¹¹ To summarize, the anisotropy of solvent configuration around the salt can be attributed to a combination of polar and steric factors, whence polar factors manifest themselves in the different strengths of the sulfonyl oxygens and the nitroso oxygen as hydrogen bond acceptors, while the steric factor is clearly seen in the hindrance caused by the sulfonyl groups and their solvation shell, which interferes with solvent accessibility to the nitroso oxygen. Fig. 6 depicts a typical solvation pattern around FS.

3.2 EPR spectral parameters

3.2.1 Hyperfine coupling to nitrogen. At the W-band, the hyperfine coupling to FS nitrogen atom is the second strongest term in the spin Hamiltonian after the electron Zeeman term. Fig. 7 shows annealed the MD-averaged principal values of the total nitrogen hyperfine coupling tensor, which shows excellent agreement with experiment.

It turns out that the value of A_{iso} is strongly correlated with the improper torsional angle of FS (Fig. 8 left), which alone accounts for 75% of the variation in A_{iso} . We have also tested regression models relating A_{iso} to other FS geometric parameters. In addition, we included two parameters related to the solvation of the nitroso group: the shortest hydrogen bond length, and the shortest distance to a methyl hydrogen. We found that in addition to the improper torsion, the inclusion of the nitroso N-O distance and the hydrogen bond length to NO gives a model with an adjusted R^2 of 0.88. Thus we find that almost 90% of the variation in A_{iso} is related to three simple geometric parameters: The cosine of FS improper torsion, the N-O bond length, and the hydrogen bond length to NO.

We now turn to the three principal components of the anisotropic HFC tensor. They only show a significant (but weak) correlation with the $\text{NO} \cdots \text{H}$ -bond length ($R^2 = 0.55 - 0.6$). In our opinion, the more interesting quantity for this system is the rhombicity of the A-tensor ($\delta A = A_X - A_Y$), which already shows a stronger correlation with the $\text{NO} \cdots \text{H}$ length ($R^2 = 0.70$, Fig. 8 right).

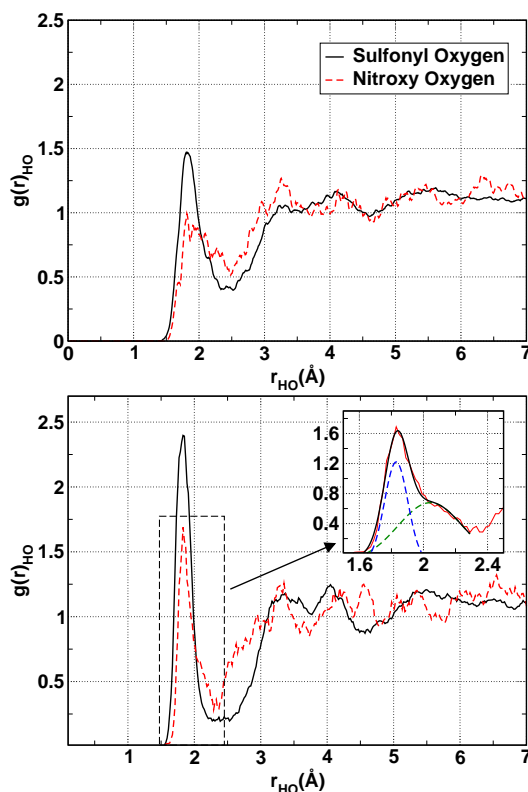


Fig. 4 RDF of the polar hydrogens around FS nitroso oxygen. Top: 300 K, bottom: 20 K.

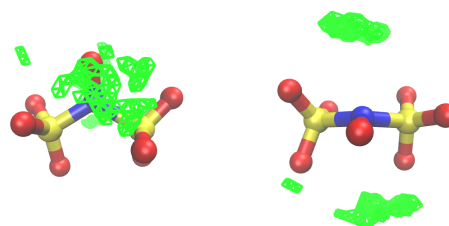


Fig. 5 Spatial distribution of the non-polar (methyl) hydrogens around the Frey's salt

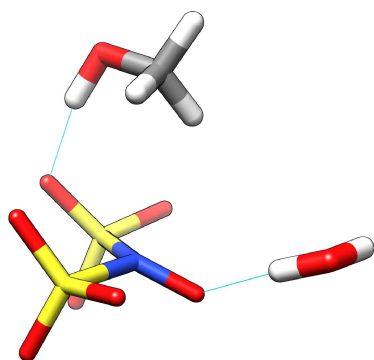


Fig. 6 Typical solvation pattern of Frey's salt.

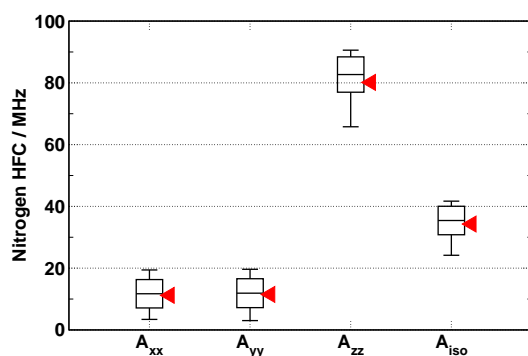


Fig. 7 Averaged principal values of the computed total nitrogen hyperfine coupling tensor (Center bar of each rectangle), their standard deviation (upper/lower border of rectangle), and minimum/maximum values from the sampling (error bars). The triangles mark the experimental values

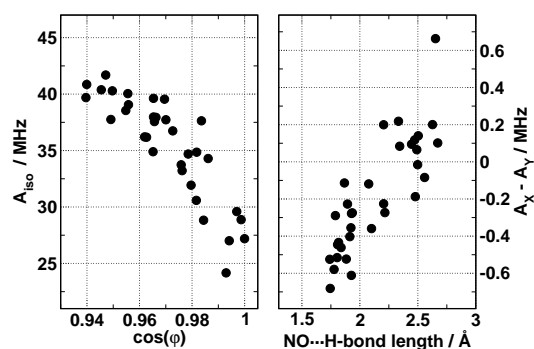


Fig. 8 Scatterplots of nitrogen A_{iso} against FS improper torsion (Left) and of the nitrogen A-tensor rhombicity (δA) against the $\text{NO}\cdots\text{H}$ -bond length (right).

g-tensor component	Setup 1	Setup 2	Setup 3
g_{xx}	-1326	-1713	-1649
g_{yy}	-363	-513	-272
g_{zz}	-681	-597	-53
g_{iso}	-793	-944	-661

Table 3 Error in g-shifts $\Delta\Delta g$ (ppm) relative to experimental values.¹¹

To summarize, we found that different components of the hyperfine coupling tensor of FS nitrogen atom carry different pieces of geometric information. A_{iso} is highly sensitive to the S-N-S-O improper torsion, and since this relation is surprisingly stable and almost insensitive to solvation effects, it can indeed be exploited to measure the degree of “planarity” of FS in different environments. On the other hand, the rhombicity of the A-tensor can be used as a probe for the hydrogen-bonding to the nitroxy oxygen.

3.2.2 Hyperfine coupling to solvent hydrogens. Fig. 9 depicts A_{iso} and the Frobenius norm of A_{aniso} as related to the distance between the hydrogen and the center of the N-O bond. The value of A_{iso} is mostly very close to zero, reflecting the absence of any significant spin density at the solvent hydrogens. The only exception is the hydrogens that are strongly hydrogen bonded to FS nitroxy, these acquire a slightly negative A_{iso} due to spin polarization. Regarding the anisotropic part of the hyperfine coupling tensor, its Frobenius norm shows the expected r^{-3} distance dependence (Fig. 9).

3.2.3 g-tensor. Fig. 10 shows the average g-tensor components obtained from the three setups (Table 1) and Table 3 summarizes the errors compared to experiment. Despite of the underlying implementation differences, the three setups give very close results. All the tensor components are underestimated, especially the g_{xx} component. However, errors of the order of 1000 ppm are not uncommon in g-tensors computed from DFT, and the quality of these results is generally consistent with previous studies.^{9,10,30,32,42,43}

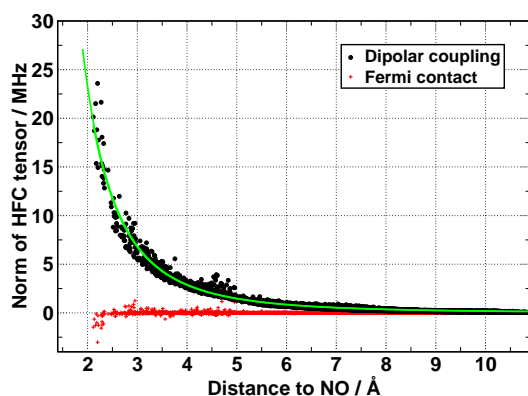


Fig. 9 Hydrogen HFC as related to distance between the hydrogen and the center of the N-O bond. The green curve is a r^{-3} decay starting from a linear fit of the first 20 points. Black: Frobenius norm of the anisotropic A-tensor. Red: A_{iso} .

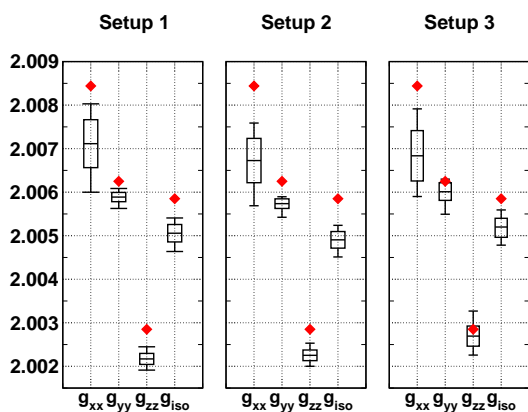


Fig. 10 Left: Distribution of the principal g-tensor components. Diamonds mark the experimental values.

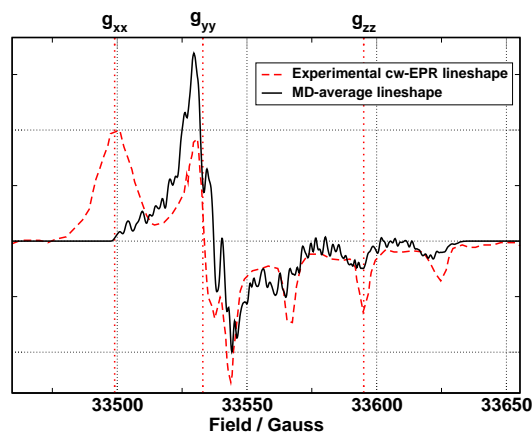


Fig. 11 Annealed MD-averaged cw-EPR lineshape. The three dotted lines mark the experimental principal components of the g-tensor.

3.3 Ensemble-averaged EPR line shapes

Fig. 11 depicts the annealed MD-averaged cw-EPR first-derivative lineshape. The lineshape which shows reasonable agreement with the experimental line, reproducing all the features except for the broad peak at the low-field end of the spectrum, corresponding to g_{xx} . The loss of detail in the low-field part of the spectrum is due to the inherent theoretical approximations which result in a somewhat larger numerical error for g_{xx} , but also partly attributed to the broad distribution of hydrogen bonding to NO. Fig. 12 shows two MD-averaged lineshapes, one taken from snapshots that have a strong hydrogen bond to NO (hydrogen bond length maximum 1.8 Å), and another one from snapshots that are non-hydrogen bonded (closed hydrogen at least 2.4 Å away). With this decomposition of the theoretical lineshape, we clearly see a small peak in the lineshape taken from the strongly solvated FS configurations. To summarize, the difficulty in obtaining a better match for the low-field end of the spectrum is mainly due to the accuracy limit of density functional theory regarding the calculation of the g_{xx} component. This problem can in principle be fixed by increasing the level of theory for the g-tensor calculation, or applying a suitable a-posteriori correction scheme. Nevertheless, the qualitative agreement of the lineshape in Fig. 11 and Fig. 12 is reasonable and illustrates the utility of first-principles molecular dynamics simulations combined with theoretical spectroscopy.

4 Conclusions

We have performed ab initio MD simulations of Frey's salt in a frozen glass of water/methanol binary solvent. Such systems are often poorly characterized and present special challenges in EPR spectroscopy, in contrast to e.g. isotropic liquids or periodic solids.²⁰ Specifically, we have explicitly sampled the local strain effects, so called "g-strain" and A-tensor anisotropy by first principles calculations of these quantities from 30 different annealed ab initio MD

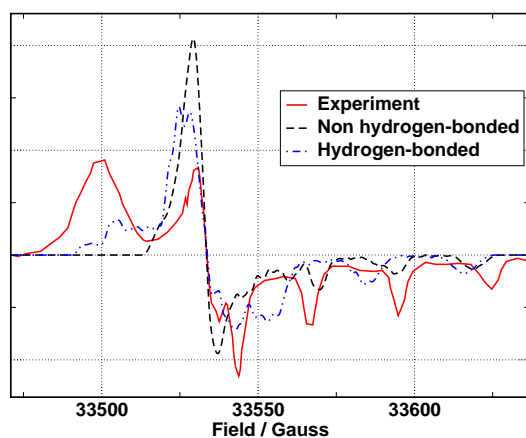


Fig. 12 Decomposing the total annealed MD-averaged lineshapes into different lineshapes according to solvation of NO. Black lineshape: NO strongly hydrogen bonded, Red lineshape: NO not hydrogen bonded.

trajectories. The latter were derived from conventional force-field MD simulations, which yielded a specific distribution of local water:methanol molar ratios around FS. We have also simulated the cw-EPR lineshapes by explicit numerical diagonalization of the spin Hamiltonian.

Examination of the ab initio MD trajectories provides detailed insight into the structure of the solvation shell, which is found to be highly anisotropic with clear and distinct spatial preferences for water and for methanol. MD also provide details about hydrogen bonding networks, and the conformational preferences of the solvated salt, which all agree very well with evidence from EPR and ENDOR spectroscopy.^{11,41}

We have also established a number of correlations between A and g-tensor components and inter/intra molecular geometric parameters. Generally, both tensors are most sensitive to the geometry of FS itself, followed by solvation effects. Specifically, we found that A_{iso} is particularly sensitive to the S-N-O-S improper torsion of FS, and that this relation is insensitive to solvation effects, and thus can serve as an experimental measure of the planarity of FS. We also found that the rhombicity of the A-tensor is related to the hydrogen bond between the nitroxy group and solvent. The simulated MD-averaged lineshape shows good agreement with experiment, reproducing all the experimental lineshape features except for the low-field peak corresponding to g_{xx} , which is attributed to the relatively large error in the corresponding computed quantity, and strong variation in this particular g-tensor component with the (highly variable) hydrogen bond strength to the NO. Decomposing the total computed lineshape into two limiting situations: the strongly hydrogen bonded limit, and the non-solvated limit reveals the g-tensor strain corresponding to this variability in the NO solvation. It is worth noting here that the low-field peak of the experimental spectrum was not very-well reproduced also by the empirical spin Hamiltonian based on least-squares fitting, which was also attributed previously to g-tensor strain. Thus,

even though this particular part of the experimental spectrum is not well-reproduced by our theoretical lineshape, we were still able to explicitly show how variation in the solvation structure is directly reflected in the lineshape.

acknowledgement

Financial support is gratefully acknowledged from the DFG under grant Se 1008/6 and from the NanoScale initiative of the FU Berlin. Supercomputer time was provided by the Jülich supercomputing center under grant 4781. Molecular graphics images were produced using VMD⁴⁴. Numerical diagonalization of the spin Hamiltonian was performed using the Eigen C++ template library⁴⁵ and parallelized using Open MPI.⁴⁶

References

- 1 M. Pavone, P. Cimino, F. De Angelis and V. Barone, *J. Am. Chem. Soc.*, 2006, **128**, 4338–47.
- 2 M. Pavone, P. Cimino, O. Crescenzi, A. Sillanpää and V. Barone, *J. Phys. Chem. B*, 2007, **111**, 8928–39.
- 3 A. R. Al Derzi, S. Fau and R. J. Bartlett, *J. Phys. Chem. A*, 2003, **107**, 6656–6667.
- 4 V. Barone, M. Brustolon, P. Cimino, A. Polimeno, M. Zerbetto and A. Zoleo, *J. Am. Chem. Soc.*, 2006, **128**, 15865–73.
- 5 A. Lund, L. D. Macomber, M. Danilczuk, J. E. Stevens and S. Schlick, *J. Phys. Chem. B*, 2007, **111**, 9484–91.
- 6 V. Barone and P. Cimino, *J. Chem. Theory Comput.*, 2009, **5**, 192–199.
- 7 J. Gauss, M. Kállay and F. Neese, *J. Phys. Chem. A*, 2009, **113**, 11541–9.
- 8 A. V. Arbuznikov, M. Kaupp, V. G. Malkin, R. Reviakine and O. L. Malkina, *Phys. Chem. Chem. Phys.*, 2002, **4**, 5467–5474.
- 9 F. Neese, *J. chem. Phys.*, 2001, **115**, 11080.
- 10 E. Pauwels, J. Asher, M. Kaupp and M. Waroquier, *Phys. Chem. Chem. Phys.*, 2011, **13**, 18638–46.
- 11 J. Heller, H. Elgabarty, B. Zhuang, D. Sebastiani and D. Hinderberger, *J. Phys. Chem. B*, 2010, **114**, 7429–38.
- 12 R. Improta and V. Barone, *Chem. Rev.*, 2004, **104**, 1231–54.
- 13 A. Nitzan, *Chemical Dynamics in Condensed Phases: Relaxation, Transfer, and Reactions in Condensed Molecular Systems*, Oxford University Press, 2006.
- 14 J. Simons and J. Nichols, *Quantum Mechanics in Chemistry*, Oxford University Press, USA, 1997.
- 15 C. P. Poole and H. A. Farach, *Relaxation in magnetic resonance: dielectric and mössbauer applications*, Academic Press, 1971.
- 16 A. M. Stoneham, *Rev. Mod. Phys.*, 1969, **41**, 82–108.
- 17 J. R. Asher, N. L. Doltsinis and M. Kaupp, *J. Am. Chem. Soc.*, 2004, **126**, 9854–61.
- 18 J. R. Asher and M. Kaupp, *ChemPhysChem*, 2007, **8**, 69–79.
- 19 S. Dixit, J. Crain, W. C. K. Poon, J. L. Finney and a. K. Soper, *Nature*, 2002, **416**, 829–32.
- 20 J. R. Pilbrow, *Appl. Magn. Reson.*, 1994, **6**, 161–181.
- 21 J. VandeVondele, M. Krack, F. Mohamed, M. Parrinello, T. Chassaing and J. Hutter, *Comput. Phys. Commun.*, 2005, **167**, 103–128.
- 22 J. VandeVondele and J. Hutter, *Chem. Phys.*, 2007, **127**, 114105.
- 23 J. Perdew, K. Burke and M. Ernzerhof, *Phys. Rev. Lett.*, 1996, **77**, 3865–3868.
- 24 S. Grimme, *J. Comput. Chem.*, 2006, **27**, 1787–99.
- 25 G. Bussi, D. Donadio and M. Parrinello, *Chem. Phys.*, 2007, **126**, 014101.
- 26 W. Kutzelnigg, U. Fleischer and M. Schindler, *Deutereum and Shift Calculation*, Springer: Heidelberg, 1990, vol. 23, pp. 165–262.

- 27 G. Lippert, J. Hutter and M. Parrinello, *Theor. Chem. Acc.*, 1999, **103**, 124–140.
- 28 V. Weber, M. Iannuzzi, S. Giani, J. Hutter, R. Declerck and M. Waroquier, *Chem. Phys.*, 2009, **131**, 014106.
- 29 L. Genovese, T. Deutsch, A. Neelov, S. Goedecker and G. Beylkin, *Chem. Phys.*, 2006, **125**, 074105.
- 30 F. Neese, *Chem. Phys.*, 2005, **122**, 34107.
- 31 V. Barone, *Recent Advances In Density Functional Methods*, World Scientific Publishing Co. Pte. Ltd., 1995, vol. 1, ch. 8, pp. 287–334.
- 32 A. Van Yperen-De Deyne, E. Pauwels, V. Van Speybroeck and M. Waroquier, *Phys. Chem. Chem. Phys.*, 2012, **14**, 10690–10704.
- 33 R Core Team, *R: A Language and Environment for Statistical Computing*, R Foundation for Statistical Computing, Vienna, Austria, 2012.
- 34 T. L. using Fortran code by Alan Miller, *leaps: regression subset selection*, 2009.
- 35 W. N. Venables and B. D. Ripley, *Modern Applied Statistics with S*, Springer, New York, 4th edn, 2002.
- 36 M. J. Frisch, G. W. Trucks, H. B. Schlegel, G. E. Scuseria, M. A. Robb, J. R. Cheeseman, G. Scalmani, V. Barone, B. Mennucci, G. A. Petersson, H. Nakatsuji, M. Caricato, X. Li, H. P. Hratchian, A. F. Izmaylov, J. Bloino, G. Zheng, J. L. Sonnenberg, M. Hada, M. Ehara, K. Toyota, R. Fukuda, J. Hasegawa, M. Ishida, T. Nakajima, Y. Honda, O. Kitao, H. Nakai, T. Vreven, J. A. Montgomery, Jr., J. E. Peralta, F. Ogliaro, M. Bearpark, J. J. Heyd, E. Brothers, K. N. Kudin, V. N. Staroverov, R. Kobayashi, J. Normand, K. Raghavachari, A. Rendell, J. C. Burant, S. S. Iyengar, J. Tomasi, M. Cossi, N. Rega, J. M. Millam, M. Klene, J. E. Knox, J. B. Cross, V. Bakken, C. Adamo, J. Jaramillo, R. Gomperts, R. E. Stratmann, O. Yazyev, A. J. Austin, R. Cammi, C. Pomelli, J. W. Ochterski, R. L. Martin, K. Morokuma, V. G. Zakrzewski, G. A. Voth, P. Salvador, J. J. Dannenberg, S. Dapprich, A. D. Daniels, J. B. Foresman, J. V. Ortiz, J. Cioslowski and D. J. Fox, *Gaussian 09 Revision A.02*, Gaussian Inc. Wallingford CT 2009.
- 37 S. Stoll and A. Schweiger, *Chem. Phys. Lett.*, 2003, **380**, 464–470.
- 38 V. I. Lebedev and D. Laikov, *Dokl. Math.*, 1999, pp. 477–481.
- 39 B. Stevensson and M. Edén, *J. Magn. Reson.*, 2006, **181**, 162–76.
- 40 M. Edén, *Concept. Magn. Reson.*, 2003, **18A**, 24–55.
- 41 D. Hinderberger, H. W. Spiess and G. Jeschke, *J. Phys. Chem. B*, 2004, **108**, 3698–3704.
- 42 R. Declerck, V. Van Speybroeck and M. Waroquier, *Phys. Rev. B*, 2006, **73**, 1–8.
- 43 O. L. Malkina, J. Vaara, B. Schimmelpfennig, M. Munzarova, V. G. Malkin and M. Kaupp, *J. Am. Chem. Soc.*, 2000, **122**, 9206–9218.
- 44 W. Humphrey, A. Dalke and K. Schulten, *J. Mol. Graphics*, 1996, **14**, 33–38.
- 45 G. Guennebaud and B. Jacob, *Eigen v3*, 2012.
- 46 E. Gabriel, G. E. Fagg, G. Bosilca, T. Angskun, J. J. Dongarra, J. M. Squyres, V. Sahay, P. Kambadur, B. Barrett, A. Lumsdaine, R. H. Castain, D. J. Daniel, R. L. Graham and T. S. Woodall, *Proceedings, 11th European PVM/MPI Users' Group Meeting*, Springer, Budapest, Hungary, 2004, pp. 97–104.

Chapter 6

Paper III

Unraveling the existence of dynamic water channels in light-harvesting proteins: alpha-C-phyocyanobilin in vitro

Hossam Elgabarty, Peter Schmieder, and Daniel Sebastiani

Chem. Sci., 2013, 4, 755-763.

Reproduced by permission of The Royal Society of Chemistry.

<http://dx.doi.org/10.1039/c2sc21145a>

Unraveling the existence of dynamic water channels in light-harvesting proteins: α -C-phycoerythrin *in vitro*[†]

Cite this: DOI: 10.1039/c2sc21145a

Hossam Elgabarty,^{ac} Peter Schmieder^d and Daniel Sebastiani^{*abc}

We present hybrid *ab initio* QM/MM MD simulations and theoretical NMR chemical shift calculations of the bilin chromophore phycoerythrin (PCB) in the binding pocket of the α -subunit of C-phycoerythrin (α -C-PC). The good overall agreement between the computed NMR chemical shifts and the experimental values confirm the overall structural picture. A particular discrepancy is observed for the pyrrole nitrogen and hydrogen on ring A, which points to a disagreement between the reported X-ray structure and the experimental solution-state NMR spectrum. Our results suggest that in the solution-state, the binding pocket of α -C-PC slightly opens up allowing one water molecule to form a stable bridge between ring A in PCB and the protein backbone at the ASN73 residue. With this modified solution-state structure, the computed NMR chemical shifts are in excellent agreement with experimental values. For proteins still lacking a fully-resolved solution-state NMR-based structure, this approach of combining *ab initio* MD/NMR provides a very sensitive probe for local geometries at the sub-Ångström range that can be utilized to compare/reconcile simple experimental one- and two-dimensional NMR data with X-ray structures.

Received 1st August 2012
Accepted 19th November 2012

DOI: 10.1039/c2sc21145a

www.rsc.org/chemicalscience

Introduction

X-Ray crystallography and NMR spectroscopy are the main experimental techniques that provide protein structures at atomic resolution.¹ Each of the two methods has its well-known advantages and technical limitations.² According to the statistics posted on the PDB website as of April 2012, the protein databank has a total of 74 603 deposited protein structures. Approximately 10% of these were obtained using NMR, the absolute majority coming from X-ray crystallography. Soon after the introduction of X-ray crystallography, it was accepted that it gives the correct picture of protein folding in spite of the non-physiological environment of a single crystal. However, some differences between solution-state and crystal structures of proteins are expected—and indeed known—to exist. For instance, in single crystals the protein molecules are densely packed, which may immobilise surface side-chains or even

backbone segments that exhibit high mobility in the isolated protein.³

Comparisons between protein structures obtained by both methods have always been highly interesting.⁴ Such comparisons necessarily require the availability of coordinates from both NMR and from X-ray crystallography for the same protein. This excludes proteins from different species, cases where one structure is for the free protein and the other for a complexed form, or where protein fragments do not have the same length.³ Fortunately, with the exponential growth in the number of entries in the PDB, statistically significant comparisons are becoming more and more accessible.^{5,6} These large scale comparisons show that in many cases the core heavy atoms are located at statistically different positions, which is attributed to crystal packing effects, the presence of interactions (steric interactions, salt bridges, hydrogen bonds) in the crystalline state that are otherwise missing for the single protein, and the different refinement methods of both approaches.^{3,7,8} In addition to such static structural differences, deviations in the dynamics of NMR and X-ray protein structures are also known to exist. As one might expect, the large-amplitude motions sampled in solution are restricted in protein crystals. Using data on 159 proteins, it was shown that the majority of proteins with high-quality NMR data suitable for 3D structure determination, do not rapidly and readily yield diffraction quality crystals, and *vice versa*, hence “X-ray crystallography and NMR often provide complementary sources of structural data and both methods

^aDahlem Center for Complex Quantum Systems (DCCQS), Physics Department, Freie Universität Berlin, Arnimallee 14, 14195 Berlin, Germany. E-mail: daniel.sebastiani@fu-berlin.de; Fax: +49 30 838 56046; Tel: +49 30 838 56149

^bInstitute of Chemistry, Martin Luther University Halle-Wittenberg, Von-Danckelmann-Platz 4, 06120 Halle (Saale), Germany

^cThe Max Planck Institute for Polymer Research (MPIP), Ackermannweg 10, 55128 Mainz, Germany

^dLeibniz-Institut für Molekulare Pharmakologie (FMP), Robert Rössle-Str. 10, 13125 Berlin, Germany

[†]Electronic supplementary information (ESI) available. See DOI: 10.1039/c2sc21145a

are required in order to optimize success for as many targets as possible in large-scale structural proteomics efforts".¹

Here we present a study of the α -subunit of C-phycocyanin, with focus on its bilin chromophore, phycocyanobilin (PCB), and its binding pocket. We exploit the high sensitivity of *ab initio* NMR calculations as an extremely sensitive local probe at the sub-Ångström range, to reveal structural differences between the crystal structure and the solution state structure. More generally, we propose an *ab initio* approach that can accurately account for local geometric differences between the X-ray structure of a protein and its solution structure, requiring only a minimal set of experimental NMR measurements.

C-Phycocyanin (C-PC) is one of the major biliproteins in phycobilisomes, and one of the earliest to be studied.⁹ Besides its role as a photoreceptor, C-PC has attracted much biomedical attention with the numerous reports of its therapeutic and nutritional values.¹⁰ C-PC exists in solution as a complex of trimers ($\alpha_3\beta_3$), hexamers ($\alpha_6\beta_6$), and other oligomers, where each α -subunit has one bilin chromophore known as phycocyanobilin (PCB) (Fig. 1) and each β -subunit has two PCBs.¹¹ Of significance to our work here is the observation that the α -subunit does not form aggregates in solution at the typical concentrations used for NMR measurements.¹² This triggers the question of whether the isolated α -subunit in solution retains the same structure as found in X-ray crystal structures or not.

Like other bilins, PCB is composed of four pyrrole rings linearly attached together with ring A being the one attached to the apoprotein, and ring D the furthest. Since we will be frequently referring to the pyrrole nitrogen atoms and the hydrogens bonded to them, we will refer to them in the remainder of this article as **NA**, **NB**, ..., **HC**, **HD**. The conformation of a bilin chromophore is conventionally described with respect to the three double (*cis/trans*) and three single (*syn/anti*) bonds comprising the methine bridges between the pyrrole rings (Fig. 1).

The structure and function of C-PC and PCB have been investigated by numerous methods, both experimental and theoretical. Through these studies, a fairly reliable picture of the structure of C-PC has been formulated and several high-

resolution X-ray crystal structures are now available (e.g. PDB entries: 3KVS, 3L0F, 3O18 and 3O2C).^{13–17} A two-dimensional projection of PCB in the binding pocket is depicted in Fig. 2. From these X-ray structures,^{16,17} it can be seen that PCB adopts a ZZZasa conformation. PCB is tightly held in place *via* its numerous interactions with the binding site. Ring A is the only one buried in the binding pocket without any access to solvent. Its carbonyl oxygen atom possibly makes a hydrogen bond with the backbone amide of ALA75 (distance 2.10 Å). The closest hydrogen bond acceptor to **HA** is the backbone carbonyl of ASN73, which is 2.65 Å away and makes an angle of 133 degree with the **NA–HA** bond. This length/angle combination is outside the usual range for a medium-strength hydrogen bond.¹⁸ Rings B, C and D are all positioned such that they have one edge exposed to the solvent. The two nitrogen atoms of ring B and C each donates a hydrogen bond to the same carboxylate oxygen atom in the ASP87 side chain. The two propionate side chains of rings B and C are oriented outside the binding site and towards the solvent. One of the carboxylate oxygens of ring B propionate forms a salt bridge with the positive ARG79 side chain and the other oxygen is solvated by water, while ring C propionate is twisted back so that both oxygens are involved in salt bridges with the positive LYS83 and ARG86 side chains. Ring D seems to be the most solvent-accessible one, both the carbonyl oxygen and **HD** are fully exposed to the solvent.

NMR has also been used to investigate the mobility of the chromophore in the binding site,¹⁹ solution state ¹⁵N NMR of the α -subunit of C-PC was used to deduce the protonation state of PCB in the binding pocket and to infer a structural picture of PCB in the cyanobacterial phytochrome Cph1,²⁰ QM/MM calculation of Raman spectra were performed and showed good agreement with experimental spectra.²¹ Through the accumulated results of all these studies one can say with confidence that the conformation of PCB in α -C-PC is indeed ZZZasa. NMR also provides convincing evidence that all the four pyrrole nitrogens of PCB are protonated in C-PC, this seems to be also true for other biliproteins.^{20,22,23} The significance of these results is not only restricted to C-PC and its chromophore, PCB. Since the availability of the first X-ray structures of C-PC they have served as models for understanding the structure and function of other biliproteins, in particular phytochromes as their tertiary structures have begun to come out only recently.

In a relatively recent study, the ¹⁵N NMR spectrum of α -C-PC from *Mastigocladus laminosus* has been compared to that of the cyanobacterial phytochrome Cph1, providing insight into the structure and dynamics of the binding pocket of the latter.²⁰ In that study, the ¹H, ¹⁵N HMQC NMR spectrum of labeled α -C-PC revealed five coherences with a nitrogen chemical shift of >130 ppm (Fig. 3). Of these five signals, two showed an interaction in the NOESY spectrum and were thus identified as **HB** and **HC** due to their proximity. In the original published assignment a peak was observed showing an interaction with two protons in the 7.0–7.5 ppm range, and was identified as **HA** due to its proximity to the backbone amine protons of Ala75 and Tyr74. Proton **HD** did not show any interactions, possibly due to its location at the edge of the binding pocket facing the bulk

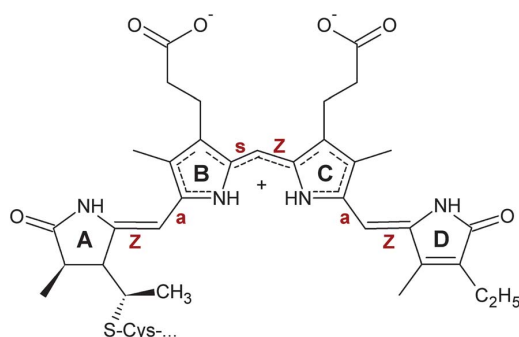


Fig. 1 Left: the structure of phycocyanobilin (PCB). Ring A is attached *via* a thioether link to a conserved cysteine residue in the apoprotein. This two-dimensional structure corresponds to a ZZZasa conformation.

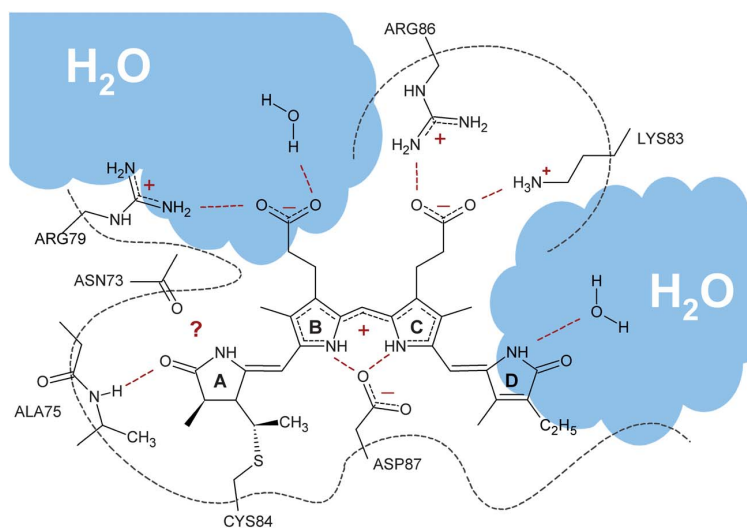


Fig. 2 A two-dimensional projection of PCB in the α -C-PC binding pocket showing the various interactions with the binding site.

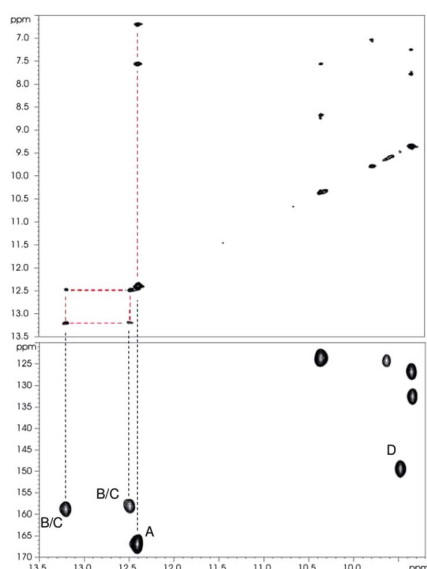


Fig. 3 The initial assignment of the four nitrogen bound protons of PCB in α -C-PC from *Mastigocladus laminosus*.²⁰ (Top) NOESY spectrum. The two protons that show an interaction with each other are **HB** and **HC**. (Bottom) Region from the ^1H , ^{15}N HMQC spectrum.

solvent, and the correlation at 149.4/9.5 ppm was assigned to it. Such assignment seemed to be the most plausible initially, however, based on more recent NMR work on isolated PCB in HMPT,²⁴ and from solid-state NMR of cyanobacterial phytochrome (Cph1),²³ we tend to believe that the initial assignment of ring D, might not be correct. In both of these publications, ring D gave a resonance close to 130 ppm, and we believe that PCB ring D in α -C-PC is actually the resonance showing at 133/9.3, close to the protein backbone resonances.

With the current availability of high-resolution structures of biliproteins, it is now possible to utilize molecular dynamics simulations based on these structures to study the mobility and dynamics of the chromophore and the atomistic details of its interactions with the apoprotein. This is particularly important in order to facilitate an explanation of the various differences in the behavior of different classes of phytochromes that cannot be explained based on the static X-ray structural pictures alone. In this particular case of PCB bound to α -C-PC, it is also useful to exploit the availability of both an X-ray structure of the system and the NMR spectrum. One is tempted to utilize the sensitivity of NMR shifts to examine any possible differences between *ab initio* H and N chemical shifts computed from the crystal structure, and the solution-state HMQC NMR spectrum.

Here, we present first-principles QM/MM MD simulations and theoretical calculations of NMR chemical shifts of PCB in the α -C-PC binding pocket. One goal of this work is to gain insight into the (mainly) non-bonded interactions between PCB and its binding pocket, and how these influence the conformation and dynamical behavior of PCB. Experimental NMR chemical shifts of PCB bound to proteins with a resolved X-ray structure have been used in attempts to deduce the geometry of PCB and other related chromophores in proteins with unavailable tertiary structures. It is an interesting question to see whether theoretical calculations of NMR chemical shifts combined with the insight obtained from MD simulations can help push forward these attempts, and to draw conclusions on other related chromophores. Finally, for such large systems, previous studies have demonstrated that the computed NMR shifts are highly sensitive to the size of the QM region and to the level of treatment of the surroundings,^{25–28} and hence another goal here is to test the convergence of the computed chemical shifts in such a complicated system with regards to the size of the QM region and the embedding scheme, *i.e.* how the

computed values respond to the level of sophistication in treating the surroundings of the chromophore.

Computational details

Structure preparation and classical MD simulations

As a starting point we used the X-ray structure of the C-phyco-cyanin trimer from *Mastigocladus laminosus* (resolution: 2.1 Å, *R*-factor: 0.217).^{16,17} The α -subunit was extracted from the structure, missing hydrogens were added and the structure was solvated in a water box with dimensions $70 \times 90 \times 60$ Ångstroms. Based on the experimental NMR evidence discussed in the introduction, all the four pyrrole rings of PCB were protonated, while the propionate side chains were left ionized so that PCB had a total charge of -1 . The system was equilibrated for 50 ns at 300 K with classical MD using the CHARMM22 forcefield^{29,30} in the NAMD program.³¹ CHARMM22-compatible force field parameters for PCB are already available and were used here.³²

Ab initio QM/MM MD simulations

QM/MM MD simulations were performed in CP2K.^{33–35} The QM region consisted of the PCB chromophore, the attached CYS84 side chain, and the ASP87 side chain. The QM/MM bond interfaces in CYS84 and ASP87 were handled using an optimized capping potential^{36,37} introduced between the alpha and beta carbon atoms (*i.e.* the alpha carbon is replaced by a capping atom). The rest of the system was treated with the CHARMM22 forcefield. The size of the QM box was set to $30 \times 30 \times 30$ Ångstroms. The BLYP functional was employed together with the Grimme D2 correction³⁸ using the GPW method and a planewave density cutoff of 280 Ry and a triple zeta gaussian basis set. 20 ps of MD were run for equilibration under massive thermostating, then finally a production run of 20 ps was performed using a Nose–Hoover thermostat at 330 K using a coupling constant of 500 fs. Each of the QM and the MM subsystems was coupled to a separate thermostat.

Nuclear shieldings

NMR calculations were also done using a QM/MM setup. To determine the appropriate size for the QM region to be used here, we have performed a series of calculations at different sizes of the QM region, using both an all-electron level and a pseudo-potential level (Fig. S1 in ESI†). Based on these calculations, the QM region for NMR calculations was extended such that besides the one used for the MD simulations (PCB + CYS84 + ASP87), we included any water molecules hydrogen-bonded to ring D or A, and the backbone segment between ASN73 and ALA75. For the latter segment, additional capping atoms had to be introduced as depicted in (Fig. 4). This choice for the QM region corresponds to a cutoff distance of 3 Å around PCB (Fig. S1 in ESI†). All the atoms in the QM region were treated at an all-electron level.

100 snapshots were extracted at regular intervals from the production phase of the simulation (*i.e.* one snapshot every 200 fs). For each of the snapshots extracted from the MD

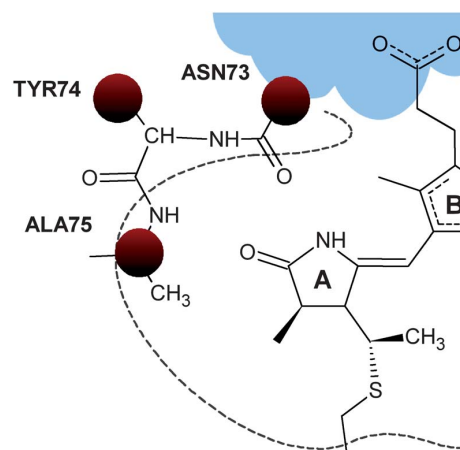


Fig. 4 QM/MM partitioning used for the NMR calculations. Additional capping atoms were introduced to encompass the backbone segment between ASN73 and ALA75 in the QM region.³⁷

trajectory, all-electron isotropic magnetic shieldings were computed for the four pyrrole nitrogens and hydrogens. CP2K was used to perform the calculations using the Gaussian and augmented-planewaves (GAPW) method³⁹ with the pcS-2 basis set (pcS-3 on the pyrrole nitrogens and hydrogens).⁴⁰ Gauge origin was treated using the IGAIM⁴¹ method as implemented in CP2K.³⁹ Proton chemical shifts were referenced to TMS at the same level of theory, while nitrogen chemical shifts were referenced to ammonia and then shifted slightly (+1.4 ppm) so that the center of the computed shifts matched that of the experimental ones. Fig. S2 in the ESI† shows the convergence of the computed NMR chemical shifts *vs.* simulation time.

Results and discussion

Dynamics of the protein and PCB

Fig. 5 left shows the X-ray structure of one C-PC monomer. Each has eight α -helices arranged in a globin-like fold.^{16,17} The first two helices in the α -subunit (residues 1–33, depicted in light-blue color) are packed against the β -subunit in the trimeric X-ray structure. In our classical MD simulations, we found that these two helices, free in water, undergo a swinging motion around a hinge at residues ARG33-ALA34, between the second and third alpha-helix (Fig. 5 middle). The classical MD-time evolution of backbone atoms RMSD relative to the X-ray structure is shown on the right in Fig. 5. Two plots are shown, one for the entire protein chain, and the other excluding the first two helices. The RMSD excluding the first two helices is very stable with an average of 1.28 Å. On the other hand, the RMSD of the entire α -subunit shows significant deviation from the X-ray structure, with an average of 3.15 Å, which is attributed to the swinging movement we just described.

Regarding the QM/MM trajectory, the average backbone RMSD is 3.08 Å and 1.65 Å, for the full subunit and excluding the first 33 residues, respectively, while the RMSD for PCB non-hydrogen atoms compared to the X-ray structure was 0.97 Å.



Fig. 5 Left: X-ray structure of a C-PC monomer showing the α (blue) and β (orange) subunits. Each subunit has an eight α -helical globin-like fold. The two light-blue helices in the α -chain (residues 1–33) are packed against the β -subunit. Middle: X-ray structure of the α -subunit (cyan) aligned to the average structure⁴² (yellow) from the last 10 ns of the classical MD trajectory. Right: backbone RMSD relative to the X-ray structure along the classical MD trajectory. The red trace is for the whole protein backbone, and the black one is obtained when residues 1–33 are excluded.

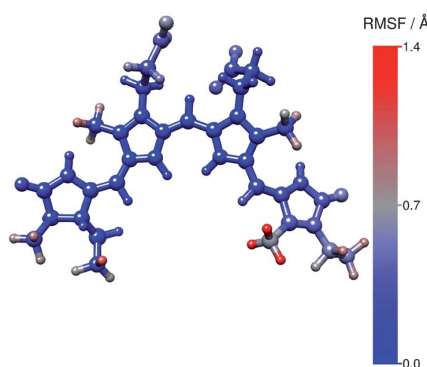


Fig. 6 RMSF of PCB atoms in the QM/MM MD trajectory. Except for ring D, PCB atoms show very little mobility.

Fig. 6 depicts the root-mean-square fluctuation (RMSF) of PCB non-hydrogen atoms during the production phase of the QM/MM trajectory. The positions of the PCB ring atoms show little fluctuations, with the exception of ring D and its ethyl side chain. Fig. 7 shows the statistical distribution of the six dihedral angles in PCB defined as in Fig. 1. The distributions indicate that the single/double bond pattern depicted in Fig. 1 is correct, with the bond resonance in rings B and C giving a partial double bond character to the two central bonds connecting them. Overall, PCB shows very little mobility in its binding pocket. The lack of mobility of ring A can be attributed to its attachment to the protein, while that of rings B and C can be attributed to them being firmly sandwiched between the hydrogen bonds to ASP87 on one side, and the ion pairing between their propionate groups and ARG79, LYS83 and ARG86 on the other side (Fig. 2).

Another interesting point is the protonation state of rings B and C. Fig. 8 shows that both **HB** and **HC** protons remain firmly attached to their nitrogens, in agreement with NMR spectra which show that the protons remain attached to the pyrrole nitrogens even on a much larger time scale. *Ab initio* thermochemical predictions provide a similar picture, where the activation energy to transfer one proton from the ASP87 to PCB was calculated to be

$0.76 \text{ kcal mol}^{-1}$, and the reverse barrier was found to be $5.57 \text{ kcal mol}^{-1}$ at the level of B3LYP/6-31+G*/HF/6-31G.⁴³

NMR signatures of hydrogen bonding

Fig. 9 shows the NMR chemical shifts of PCB pyrrole nitrogens and hydrogens computed from first principles as an ensemble average over the configurations delivered by the MD trajectory. The corresponding experimental values are also shown for comparison. The points corresponding to the experimental spectrum are labeled according to the initial assignment,²⁰ while the point labeled as \bar{D} is what we believe to be the correct assignment of ring D. Overall, rings B and C show very good agreement, and interestingly, the *ab initio* value for ring D at 137.6 ppm strongly suggests that D at 133 ppm is indeed the corresponding experimental signal, rather than the originally-assigned signal at 149.4 ppm. The predicted nitrogen chemical shift for ring A at 169 ppm is very close to the experimental signal for the point experimentally assigned as A

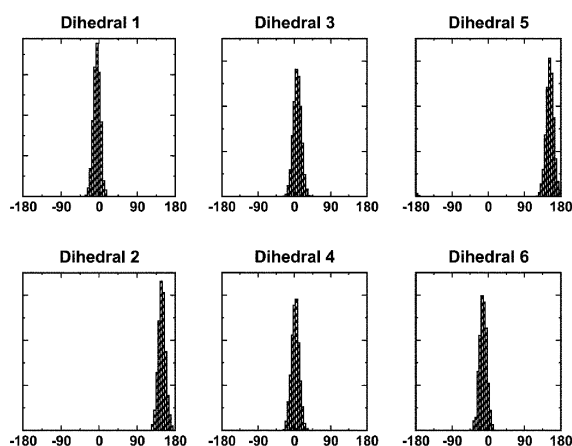


Fig. 7 Histogram of the six dihedral angles along the six bonds connecting the pyrrole rings in PCB (Fig. 1) from 20 ps QMMM MD trajectory. The six dihedrals are numbered in order going from ring A to B to C to D. The ordinate is in arbitrary units.

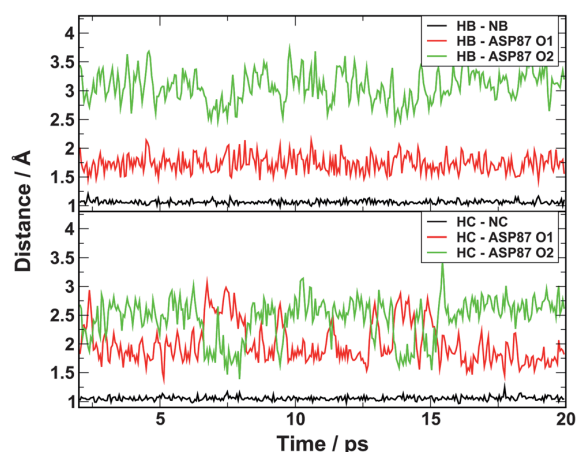


Fig. 8 Top: distances between NB and: (1) HB, (2) the two carboxylate oxygens of the ASP87 side chain. Bottom: Corresponding distances for NC.

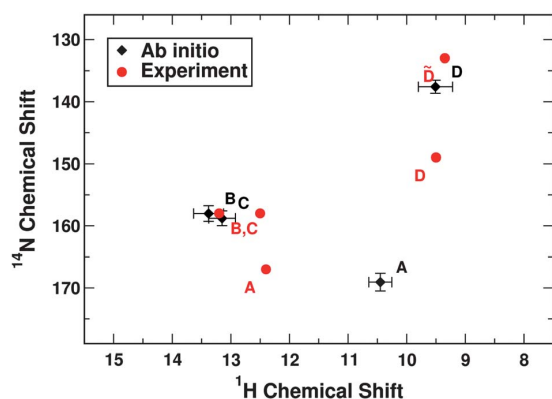


Fig. 9 Experimental vs. MD-averaged *ab initio* NMR chemical shifts of the pyrrole nitrogens and hydrogens in PCB. Here, the overall geometry of PCB and its binding pocket correspond closely to that depicted in Fig. 2 and 5. The point labelled as D is what we believe to be the actual experimental NMR signal of ring D. Error bars indicate the standard error.

(167 ppm), while it is significantly off for the hydrogen chemical shift.

Further insight into the correlation between binding pocket geometry and the NMR signature is obtained by examining the correlations depicted in Fig. 10. The plots show the calculated dependence of instantaneous proton chemical shifts on the length of the corresponding hydrogen bond. In the region of strong hydrogen bonding ($d_{\text{H-D}} < 2.2$) the relation is approximately linear, followed by an asymptotic decay for longer distances towards the chemical shift of the non-hydrogen-bonded situation. From the plot corresponding to HA, we can see that its chemical shift corresponds to a hydrogen bond length averaged around 1.8 Å. Looking at the slopes of the linear regressions considering only lengths up to 2.0 Å, we find that all the plots exhibit a proportionality in the range -9.5 to -10.5 ppm Å $^{-1}$, except for ring A which a lower slope

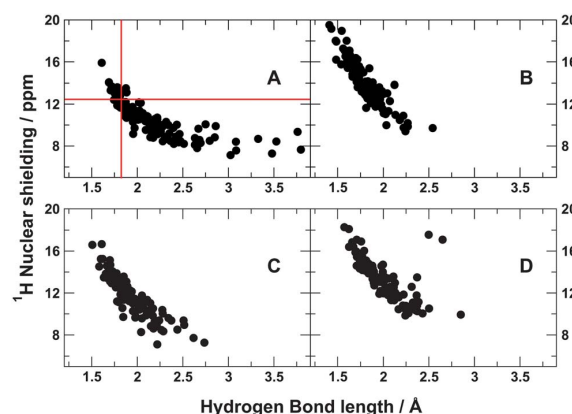


Fig. 10 Correlation between hydrogen bond length and the chemical shift of the pyrrole hydrogens.

of -8.0 ppm Å $^{-1}$. These large values for the slope are the very reason why NMR is such a good probe of local geometries: We have a change in the observed ^1H chemical shift of 1 ppm (a value easily within the accuracy of both experiment and *ab initio* methods) per 0.1 Å change in the hydrogen bond length. One can even go further and use such a plot as a “calibration curve” to correlate the observed chemical shifts to local geometries at the sub-Ångstrom range, a range that is inaccessible for most other spectroscopic techniques.

Going back to our trajectories, we depict in Fig. 11 the time-evolution of the distances between ring A and the nearest possible hydrogen bonding groups, from both the QM/MM and the CHARMM22 MD trajectory. We can see that these distances are too long to influence the chemical shift of HA, they are within the asymptotic part in Fig. 10, not to mention to explain the strong shift seen in the experimental NMR spectrum. These results point in the same direction as our arguments in the introduction, the X-ray structure and the solution-state NMR spectrum do not match for ring A.

Our first attempt to reconcile the X-ray structure and the solution-state NMR results was running another CHARMM22 MD simulation, this time constraining the distance between HA and the backbone oxygen of ASN73 to 1.8 Å. In this way, a strong hydrogen bond is enforced for HA. After equilibration, the system was left to evolve for 40 ns under this constraint before releasing it and allowing the system to evolve freely for 60 ns. As Fig. 12 shows, the protein backbone starts gradually recoiling away from HA once the constrain is gone, and within 10 ns, all memory of the constraint is lost. In conclusion, this attempt did not succeed to “convince” the chromophore to attain a hydrogen-bonding configuration which would presumably yield a computed NMR chemical shift pattern compatible with experiment.

Another interesting possibility arises by careful examination of our initial, unconstrained CHARMM22 trajectory. Fig. 13 depicts two representative configurations of the binding pocket where water wires are forming between PCB, ALA75, ASN73 and bulk water. The initial event for formation

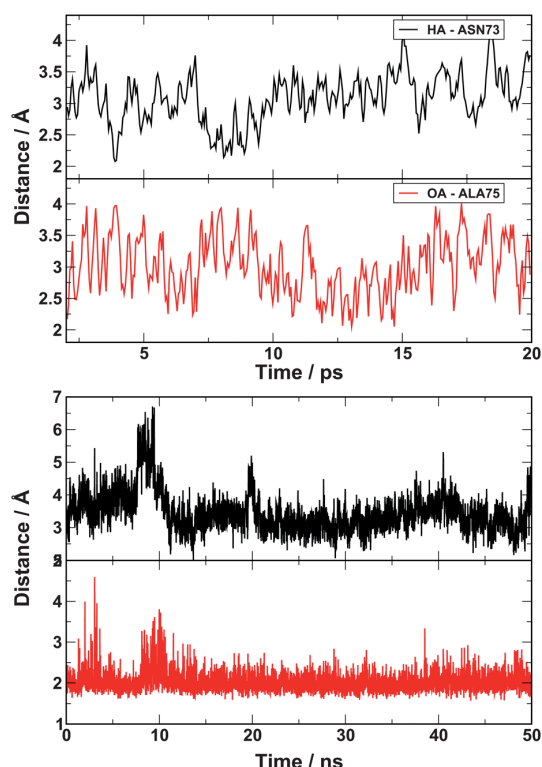


Fig. 11 Top: time evolution of the hydrogen bond length between **HA** to ASN73 backbone oxygen (top), and between ALA75 backbone hydrogen to ring A carbonyl oxygen (bottom). Bottom: same distances taken from the CHARMM22 trajectory.

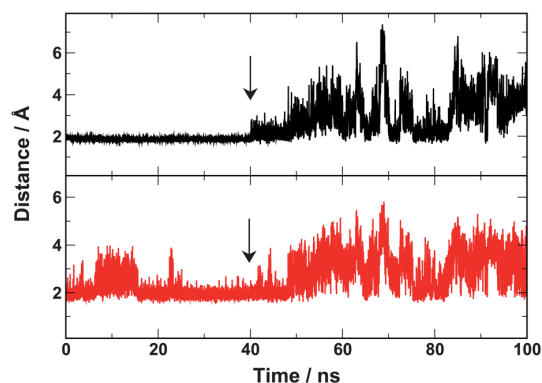


Fig. 12 Time evolution of the **HA**–ASN73 (top), and ring A oxygen–ALA75 distances (bottom). The arrows mark the time when the distance constraint was removed.

of such water wires is the opening up of the “binding pocket gate” near ring A: A movement of the side chain ASN73 away from PHE122 backbone, exchanging the lost hydrogen bond by another stable one to the propionate side chain of ring B. Such an arrangement can be seen in Fig. 13 (bottom), once the gate is open, bulk water starts pouring inside the pocket, resulting

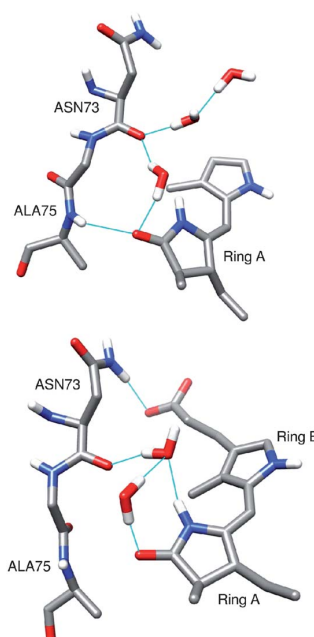


Fig. 13 Examples of the water wires that form inside the PCB binding pocket, bridging ring A to ASN73.

in a water wire. The backbone amino group of ALA75 can be seen switching between two situations: in one it is hydrogen-bonded to the oxygen atom of ring A (Fig. 13 left, *anti*-conformation relative to ASN73), and in the other it is forming a hydrogen bond to LEU66O (Fig. 13 right, *clinal*-conformation), which is part of an alpha-helix on the solvent-exposed protein surface. Indeed, such configurations can also be seen forming in the last few picoseconds in the *ab initio* MD trajectory. In fact, if these configurations are excluded from the NMR sampling, the **HA** chemical shift further moves by 0.5 ppm upfield.

Based on this evidence, we started another QM/MM trajectory from such a configuration with water wires, using the same computational setup as before for both the MD and the NMR calculations. The MD reveals that once a water molecule is trapped between **HA** and the ASN73 backbone, it forms a very stable bridge, with an average distance of 1.85 Å between the water oxygen and **HA**. In fact, such a configuration agrees with the experimental NMR signature, as it represents a stable hydrogen bond to ring A at the required distance. Fig. 14 shows the MD-averaged NMR chemical shifts (20 ps) from the new setup compared to experimental results. The agreement between computed and experimental NMR signatures is far better in this case, with **HA** showing a shift of 12.15 ppm, close to the experimental shift at 12.4 ppm, and confirming that the inclusion of the water wire at ring A yields an NMR chemical shift pattern that matches the experimental counterpart very well. In this case, the shift of **ND** moves downfield to 139.3 ppm, but still closer to point **D** at 133 ppm than to the originally assigned point **D** at 149.4 ppm.

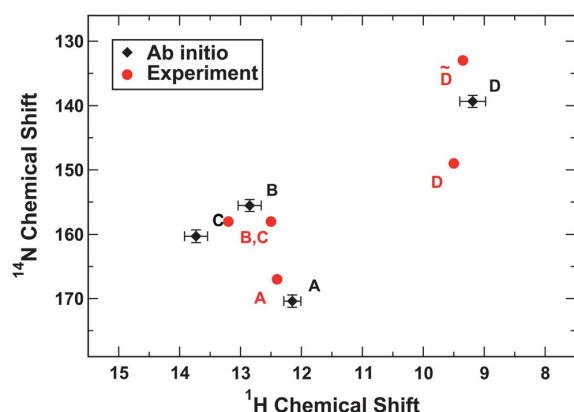


Fig. 14 MD-averaged NMR chemical shifts taken from the QM/MM trajectory in which a water wire bridges ring A to ASN73 and connects to bulk water (Fig. 13). Error bars indicate the standard error.

As for the correct assignment of the originally mislabeled NMR resonance at D, we believe that it might have originated from a protein histidine. However at the present state, we do not have sufficient experimental/computational evidence to claim that this is a certain assignment.

Conclusions

We have presented an analysis of the accessibility of the bilin chromophore embedded in the α -subunit of C-phycocyanin with respect to water molecules from within the protein. We have used first-principles molecular dynamics simulations and *ab initio* calculations of NMR chemical shift patterns to interpret the corresponding experimental data. The comparison of computational and experimental data leads to considerable structural differences between the solution-state and the crystalline conformations, in particular in view of the micro-solvation of ring A of the bilin chromophore. The loop in the PCB binding site, which is packed against the crystal packing surface, has more freedom in solution which leads to its movement away from PCB. This allows one water molecule to pour inside in the binding pocket, bridging ring A to the ASN73 backbone, and eventually forming a stable water wire that connects to bulk solvent.

Our approach of computing ensemble averages of NMR chemical shift patterns from first principles molecular dynamics simulations provides a working method to reconcile X-ray crystal structures and solution state structures using a minimal set of experimental NMR data. The speed with which NMR chemical shifts can be computed on modern computers makes the method quite affordable, even with the extensive sampling required to converge the NMR shifts towards the experimental results. Another possible application of this approach is for membrane proteins with poorly resolved structures. If one is particularly interested in one region, then our method provides a microscopic probe that can look at distances at the sub-Ångström range provided that

experimental NMR/EPR signatures are available. The argument applies equally well to protein structures that cannot be investigated by NMR (large proteins). One has to keep in mind that the choice of the size of the QM region and the capping method in the MD/NMR calculations is very critical. The quality of the capping method becomes particularly critical when the capping atom is close to an atom where NMR chemical shift is to be computed.

We view this work as a continuation of the efforts that utilize *ab initio* QM methods in structural biology, from assessing the quality of X-ray structures by *ab initio* ^{13}C NMR,⁴⁴ to the use of *ab initio* methods in optimizing and refining X-ray structures.^{45,46} We go here one step further by combining MD and NMR calculations to provide results directly comparable to a highly sensitive experimental observable. Our calculations show that a fully consistent first-principles treatment, from molecular dynamics simulations to ensemble averages of spectroscopic observables, can elucidate subtle differences between crystal structures and solution structures of proteins. In our case, the local mobility of a particular building block of the chromophore is considerably increased under solvated conditions at ambient temperatures, which is connected to an opening of the binding pocket towards a neighboring water channel.

As detailed in the introduction, isolated C-PC serves as a model in a very large number of experimental and theoretical investigations to probe the function and properties of light-harvesting systems,⁴⁷ and indeed these studies have significantly advanced our understanding of such systems.⁴⁸ However, one has to keep in mind that *in vivo*, C-phycocyanin is part of a large light-harvesting complex. In fact, it has been recently questioned whether the rods that phycocyanin structures form in crystals as seen by X-rays are equivalent to those found in phycobilisomes when *in vivo* as visualized by transmission electron microscopy.¹⁵ Thus, at this point it is not clear to us whether this finding is relevant regarding the biological function of C-PC as a light-harvesting protein or its various pharmacological effects.

Acknowledgements

Financial support is gratefully acknowledged from the DFG under grant Se 1008/6 and from the NanoScale initiative of the FU Berlin. Supercomputer time was provided by the Jülich supercomputing center under grant 4781. Molecular graphics images were produced using VMD⁴⁹ and the UCSF-Chimera package.⁵⁰

References

- 1 D. a. Snyder, Y. Chen, N. G. Denissova, T. Acton, J. M. Aramini, M. Ciano, R. Karlin, J. Liu, P. Manor, P. a. Rajan, P. Rossi, G. V. T. Swapna, R. Xiao, B. Rost, J. Hunt and G. T. Montelione, *J. Am. Chem. Soc.*, 2005, **127**, 16505–16511.
- 2 J. Kirchmair, P. Markt, S. Distinto, D. Schuster, G. M. Spitzer, K. R. Liedl, T. Langer and G. Wolber, *J. Med. Chem.*, 2008, **51**, 7021–7040.

- 3 M. Billeter, J. Vendrell, G. Wider, F. X. Avilés, M. Coll, A. Guasch, R. Huber and K. Wüthrich, *J. Biomol. NMR*, 1992, **2**, 1–10.
- 4 M. Praissman, *J. Am. Chem. Soc.*, 1964, **86**, 3584–3585.
- 5 M. Andrec, D. A. Snyder, Z. Zhou, J. Young, G. T. Montelione and R. M. Levy, *Proteins: Struct., Funct., Bioinf.*, 2007, **69**, 449–465.
- 6 L.-W. Yang, E. Eyal, C. Chennubhotla, J. Jee, A. M. Gronenborn and I. Bahar, *Structure*, 2007, **15**, 741–749.
- 7 I. Bertini, P. Kursula, C. Luchinat, G. Parigi, J. Vahokoski, M. Wilmanns and J. Yuan, *J. Am. Chem. Soc.*, 2009, **131**, 5134–5144.
- 8 P. R. Kuser, L. Franzoni, E. Ferrari, A. Spisni and I. Polikarpov, *Acta Crystallogr., Sect. D: Biol. Crystallogr.*, 2001, **57**, 1863–1869.
- 9 D. S. Berns, H. L. Crespi and J. J. Katz, *J. Am. Chem. Soc.*, 1963, **85**, 8–14.
- 10 C. Romy, R. Gonzalez, N. Ledon, D. Ramirez and V. Rimbau, *Curr. Protein Pept. Sci.*, 2003, **4**, 207–216.
- 11 Y. Ren, J. Wan, X. Xu, Q. Zhang and G. Yang, *J. Phys. Chem. B*, 2006, **110**, 18665–18669.
- 12 B. J. Homoele and W. F. Beck, *Biochemistry*, 1997, **36**, 12970–12975.
- 13 N. Adir, *Photosynth. Res.*, 2005, **85**, 15–32.
- 14 A. a. Arteni, L.-N. Liu, T. J. Aartsma, Y.-Z. Zhang, B.-C. Zhou and E. J. Boekema, *Photosynth. Res.*, 2007, **95**, 169–174.
- 15 L. David, A. Marx and N. Adir, *J. Mol. Biol.*, 2011, **405**, 201–213.
- 16 T. Schirmer, W. Bode and R. Huber, *J. Mol. Biol.*, 1987, **196**, 677–695.
- 17 M. Duerring, R. Huber and W. Bode, *FEBS Lett.*, 1988, **236**, 167–170.
- 18 S. J. Grabowski, *Chem. Rev.*, 2011, **111**, 2597–2625.
- 19 M. Röben, J. Hahn, E. Klein, T. Lamparter, G. Psakis, J. Hughes and P. Schmieder, *ChemPhysChem*, 2010, **11**, 1248–1257.
- 20 J. Hahn, R. Kühne and P. Schmieder, *ChemBioChem*, 2007, **8**, 2249–2255.
- 21 M. A. Mroginiski, F. Mark, W. Thiel and P. Hildebrandt, *Biophys. J.*, 2007, **93**, 1885–1894.
- 22 H. M. Strauss, J. Hughes and P. Schmieder, *Biochemistry*, 2005, **44**, 8244–8250.
- 23 T. Rohmer, C. Lang, J. Hughes, L.-o. Essen, W. Gärtner and J. Matysik, *Proc. Natl. Acad. Sci. U. S. A.*, 2008, **105**, 15229–15234.
- 24 M. Röben and P. Schmieder, *Magn. Reson. Chem.*, 2011, 543–548.
- 25 D. Sebastiani and U. Röthlisberger, *J. Phys. Chem. B*, 2004, **108**, 2807.
- 26 D. Flaig, M. Beer and C. Ochsenfeld, *J. Chem. Theory Comput.*, 2012, **8**, 2260–2271.
- 27 A. Frank, I. Onila, H. M. Möller and T. E. Exner, *Proteins: Struct., Funct., Bioinf.*, 2011, **79**, 2189–2202.
- 28 A. Frank, H. M. Möller and T. E. Exner, *J. Chem. Theory Comput.*, 2012, **8**, 1480–1492.
- 29 A. D. MacKerell, D. Bashford, R. L. Dunbrack, J. D. Evanseck, M. J. Field, S. Fischer, J. Gao, H. Guo, S. Ha, D. Joseph-McCarthy, L. Kuchnir, K. Kuczera, F. T. K. Lau, C. Mattos, S. Michnick, T. Ngo, D. T. Nguyen, B. Prodhom, W. E. Reiher, B. Roux, M. Schlenkrich, J. C. Smith, R. Stote, J. Straub, M. Watanabe, J. Wiórkiewicz-Kuczera, D. Yin and M. Karplus, *J. Phys. Chem. B*, 1998, **102**, 3586–3616.
- 30 A. D. Mackerell, M. Feig and C. L. Brooks, *J. Comput. Chem.*, 2004, **25**, 1400–1415.
- 31 J. C. Phillips, R. Braun, W. Wang, J. Gumbart, E. Tajkhorshid, E. Villa, C. Chipot, R. D. Skeel, L. Kalé and K. Schulten, *J. Comput. Chem.*, 2005, **26**, 1781–1802.
- 32 S. Kaminski and M. A. Mroginiski, *J. Phys. Chem. B*, 2010, **114**, 16677–16686.
- 33 J. VandeVondele, M. Krack, F. Mohamedb, M. Parrinello, T. Chassaing and J. Hutter, *Comput. Phys. Commun.*, 2005, **167**, 103–128.
- 34 T. Laino, F. Mohamed, A. Laio and M. Parrinello, *J. Chem. Theory Comput.*, 2005, **1**, 1176–1184.
- 35 T. Laino, F. Mohamed, A. Laio and M. Parrinello, *J. Chem. Theory Comput.*, 2006, **2**, 1370–1378.
- 36 C. Schiffmann and D. Sebastiani, *J. Chem. Theory Comput.*, 2011, **7**, 1307–1315.
- 37 A. C. Ihrig, C. Schiffmann and D. Sebastiani, *J. Chem. Phys.*, 2011, **135**, 214107.
- 38 S. Grimme, *J. Comput. Chem.*, 2006, **27**, 1787–1799.
- 39 V. Weber, M. Iannuzzi, S. Giani, J. Hutter, R. Declerck and M. Waroquier, *J. Chem. Phys.*, 2009, **131**, 014106.
- 40 F. Jensen, *J. Chem. Theory Comput.*, 2008, **4**, 719–727.
- 41 T. Keith and R. Bader, *Chem. Phys. Lett.*, 1992, **194**, 1–8.
- 42 L. a. Kelley, S. P. Gardner and M. J. Sutcliffe, *Protein Eng., Des. Sel.*, 1996, **9**, 1063–1065.
- 43 J. Wan, X. Xu, Y. Ren and G. Yang, *J. Phys. Chem. B*, 2005, **109**, 11088–11090.
- 44 J. a. Vila and H. a. Scheraga, *Acc. Chem. Res.*, 2009, **42**, 1545–1553.
- 45 U. Ryde and K. Nilsson, *J. Am. Chem. Soc.*, 2003, **125**, 14232–14233.
- 46 Y.-W. Hsiao, E. Sanchez-Garcia, M. Doerr and W. Thiel, *J. Phys. Chem. B*, 2010, **114**, 15413–15423.
- 47 A. Marin, A. B. Doust, G. D. Scholes, K. E. Wilk, P. M. G. Curmi, I. H. M. van Stokkum and R. van Grondelle, *Biophys. J.*, 2011, **101**, 1004–1013.
- 48 A. B. Doust, K. E. Wilk, P. M. Curmi and G. D. Scholes, *J. Photochem. Photobiol., A*, 2006, **184**, 1–17.
- 49 W. Humphrey, A. Dalke and K. Schulten, *J. Mol. Graphics*, 1996, **14**, 33–38.
- 50 E. F. Pettersen, T. D. Goddard, C. C. Huang, G. S. Couch, D. M. Greenblatt, E. C. Meng and T. E. Ferrin, *J. Comput. Chem.*, 2004, **25**, 1605–1612.

Chapter 7

Conclusion

In this doctoral research, a number of studies have been performed that all share the common theme of combining the techniques of classical, *ab initio*, and hybrid QM/MM MD simulations with the *ab initio* calculation of magnetic resonance parameters (NMR and EPR) to study condensed disordered systems under realistic thermodynamic conditions. In all cases the work was performed in collaboration with experimental laboratories (the Max Planck Institute for Polymer research and the Leibniz-Institut für Molekulare Pharmakologie), and the results of theory and experiment could be closely compared. Two very different systems in terms of size and dynamics were the focus of this work. The first system was an inorganic free radical, Fremy's salt, dissolved in a mixture of water and methanol and experimentally probed using EPR and ENDOR spectroscopy both in the liquid state and as a frozen glass. Our simulations gave detailed insights about the structure of the anisotropic solvation structure that very closely matched the one inferred from experiments. Computed EPR spectroscopic parameters showed good agreement with experiment, and the simulated cw-EPR lineshapes gave further insights about local solvation effects. The second system studied was the alpha chain of the photoreceptor protein C-phycocyanin in aqueous solution. Here experimental data comprised the X-ray structure and two-dimensional (NOESY and HMQC) solution NMR spectra. In this case, our study revealed some significant structural differences between the crystal structure and the solution structure of the protein, in particular regarding the solvation of the chromophore. Ensemble-averaged *ab initio* NMR chemical shifts based on this modified structural picture show very good agreement with experiment.

These studies show that a fully consistent first-principles treatment, from molecular dynamics simulations to *ab initio* ensemble-averaged spectroscopic observables, leads to significant improvements in the agreement between theory and experiment, and also leads to insights not directly available from consideration of the experimental results only. There is a number of interesting directions that can be pursued in the future. In the field of structural biology, our approach can be extended to membrane proteins with poorly resolved structures, and to protein structures that cannot be fully elucidated by solution NMR (*e.g.* large proteins). In the direction of heterogeneous solvent mixtures, one can for example compute a full MD-averaged pulsed-ENDOR lineshape, giving further insights into how the solvation structure is reflected in this – currently mainstream – double resonance technique in EPR spectroscopy.

English Summary

In this doctoral research, a number of studies have been performed that all share the common theme of combining the techniques of (classical, *ab initio*, and hybrid QM/MM) MD simulations with the *ab initio* calculation of magnetic resonance parameters (NMR and EPR) to study condensed disordered systems under realistic thermodynamic conditions. In all cases the work was performed in collaboration with experimental laboratories (the Max Planck Institute for Polymer research and the Leibniz-Institut für Molekulare Pharmakologie), and the results of theory and experiment could be closely compared.

The first system studied was an inorganic free radical, Fremy's salt, dissolved in a mixture of water and methanol and experimentally probed using EPR/ENDOR spectroscopy both in the liquid state and as a frozen glass. This solvent system has been shown to be microheterogeneous, and when frozen gives a spectroscopically "poorly characterized" system where heterogeneous broadening of the spectral lineshape has additional contributions from variations in local solvation structure and unresolved hyperfine couplings to solvent. In a first study, the focus was the development of force field parameters for Fremy's salt and the simulation of the solvated salt in binary water/methanol solvent using empirical potentials (classical force-field-based MD). MD results not only revealed an anisotropic solvation picture that closely matched the one inferred from EPR and ENDOR spectroscopy, but also provided a clear and intuitive explanation of the solvation shell structure relating to the polar/steric properties of the solvent molecules.

In the second study, the same system, Fremy's salt dissolved in water/methanol, was also the focus. This time the target was a more quantitative characterization of the solvation structure, calculation of the EPR spectroscopic parameters, and the study of their dependence on local solvation environment. To the best of our knowledge, this is the first work to attempt such a task for frozen glasses with inhomogeneously broadened lineshapes, where the broadening is not only due to the anisotropies in the magnetic resonance parameters, but also due to the variations in the local solvation environment at the different spin systems (so-called "strain" in literature), and also unresolved hyperfine couplings to solvent protons. Via exact diagonalization of the spin Hamiltonian, we were able to simulate the full spectral lineshape taking account of inhomogeneous broadening due to g-tensor and nitrogen A tensor strain and anisotropy, and also taking account of unresolved hyperfine couplings to the solvent protons. The simulated lineshape showed good agreement with experiment, and its decomposition based on the strength of the hydrogen bonding to Fremy's salt nitroxy oxygen gave results that closely matched experimental findings. The data was also analyzed in terms of dependence of the EPR parameters on molecular geometry, which gave valuable information useful for future studies using Fremy's salt.

In the third study, a system that is totally different in terms of size and dynamics was studied: The alpha chain of the photoreceptor protein C-phycocyanin in aqueous solution. Here the experimental data comprised the X-ray structure and two-dimensional (NOESY and HMQC)

solution NMR spectra. In this case, the comparison of computational and experimental data lead to considerable structural differences between the solution-state structure and the crystalline conformation, particularly in view of the microsolvation of ring A of the bilin chromophore. A loop in the phycocyanobilin (PCB) binding site which is packed against the crystal packing surface, has more freedom in solution which leads to its movement away from PCB. This allows one water molecule to pour inside the binding pocket, eventually forming a stable water wire that connects to bulk solvent. Ensemble-averaged *ab initio* NMR chemical shifts based on this modified structural picture show very good agreement with experiment. Generally, this approach can elucidate subtle differences between crystal structures and solution structures of proteins, and provides a working method to reconcile both structural pictures using a minimal set of experimental NMR data. The approach can also be applied equally to membrane proteins with poorly resolved structures, and to protein structures that cannot be fully elucidated by solution NMR (*e.g.* large proteins).

These studies show that a fully consistent first-principles treatment, from molecular dynamics simulations to *ab initio* ensemble-averaged spectroscopic observables, leads to significant improvements in the agreement between theory and experiment, and also leads to insights not directly available from consideration of the experimental results only.

German Summary

In dieser Doktorarbeit wurden eine Reihe von Studien durchgeführt, welche alle ein gemeinsames Thema haben: es ist die Kombination von (ab initio) MD Simulationen mit ab initio Berechnungen von magnetischen Resonanzparametern (sowohl NMR als auch EPR) um kondensierte ungeordnete Systeme unter realistischen thermodynamischen Bedingungen zu untersuchen. In allen Fällen wurde mit experimentell arbeitenden Einrichtungen (dem Max Planck Institut für Polymerforschung und dem Leibniz-Institut für Molekulare Pharmakologie) zusammen gearbeitet, so dass die Ergebnisse aus Theorie und Experiment sehr gut miteinander verglichen werden können.

Das erste betrachtete System ist ein anorganisches freies Radikal, Fremys Salz, welches in einer Mischung aus Wasser und Methanol gelöst und experimentell durch EPR/ENDOR Spektroskopie sowohl im flüssigen Zustand als auch als gefrorenes Glas erforscht wurde. Es wurde gezeigt, dass dieses System in Lösung mikroheterogen ist. Im gefrorenen Zustand liefert es ein spektroskopisch "schlecht charakterisiertes" System, bei dem heterogene Verbreiterung der Form der Spektrallinie zusätzlich Beiträge aus den Variationen in der lokalen Lösungsstruktur und ungelösten hyperfeinen Kopplungen mit dem Lösungsmittel mit sich bringt. In der ersten Untersuchung lag der Fokus auf der Entwicklung von Kraftfeld-Parametern für Fremys Salz sowie der Simulation des gelösten Salzes in Wasser-Methanol-Lösung. Dazu wurden empirische Potentiale (klassische Kraftfeld-basierte MD) verwendet. Die MD Ergebnisse lieferten nicht nur eine anisotrope Lösungsstruktur, die jener aus der EPR und ENDOR Spektroskopie sehr ähnlich ist, sondern auch eine eindeutige und intuitive Erklärung für die Solvathülle bezüglich den polaren und sterischen Eigenschaften der Lösungsmoleküle.

In der zweiten Untersuchung wurde das gleiche System, in Wasser und Methanol gelöstes Fremysches Salz, betrachtet. Dieses Mal wurde sich eine quantitativere Charakterisierung der Lösungsstruktur, die Berechnung von EPR spektroskopischen Parametern und deren Untersuchung bezüglich der Abhängigkeit von der lokalen Lösungsumgebung zum Ziel gesetzt. Soweit es uns bekannt ist, ist dies die erste Arbeit, die so eine Untersuchung an gefrorenem Glas mit inhomogen verbreiterten Spektrallinienformen in Angriff nimmt. Zu beachten ist, dass hierbei die Verbreiterung nicht nur aufgrund von Anisotropien in den magnetischen Resonanzparametern auftritt, sondern auch durch Variationen in der lokalen Lösungsumgebung der unterschiedlichen Spinsysteme (in der Literatur "strain" genannt) und nicht gelösten hyperfeinen Kopplungen mit den Protonen des Lösungsmittels hervorgerufen wird. Durch exakte Diagonalisierung des Spin-Hamiltonians sind wir in der Lage die gesamte spektrale Linienform zu simulieren und dabei die inhomogene Verbreiterung, hervorgerufen durch g-Tensor und Stickstoff A tensor "strain" und Anisotropie, einzubeziehen. Desweiteren haben wir die nicht gelösten hyperfeinen Kopplungen mit den Protonen des Lösungsmittels berücksichtigt. Die simulierte Linienform zeigt eine gute Übereinstimmung mit dem Experiment und ihre Zerlegung basierend auf der Stärke der Wasserstoffbrückenbindungen mit jenem Sauerstoffatom, welches in Fremys Salz mit dem Stickstoffatom verbunden ist, liefert Ergebnisse, die sehr nah an den experimentellen Beobachtungen sind. Die Daten wurden auch in Bezug

auf die Abhängigkeit der EPR Parameter von der Geometrie des Moleküls analysiert. Dies erbrachte wertvolle Informationen, die in zukünftigen Untersuchungen von Fremys Salz von Nutzen sein können.

In der dritten Untersuchung wurde ein System betrachtet, welches in Bezug auf Größe und Dynamik komplett verschieden ist: Die alpha-Kette des Photorezeptor-Proteins C-Phycocyanin in wässriger Lösung. In diesem Fall beinhalten die experimentellen Ergebnisse die Röntgenstruktur und die zweidimensionalen (NOESY und HMQC) NMR Lösungsspektren. Hierbei führt der Vergleich von rechnerischen und experimentellen Daten zu beachtlichen strukturellen Unterschieden zwischen der Struktur des Lösungszustands und der kristallinen Konformation, insbesondere in Bezug auf die Mikrosolvatation des Rings A des Bilin-Chromophors. In Lösung gelangt ein Wassermolekül in die Bindungstasche und bildet schließlich eine stabile water wire, die mit dem bulk Lösungsmittel verbunden ist. Basierend auf dem modifizierten strukturellen Bild wurden über das Ensemble gemittelte ab initio NMR chemische Verschiebungen betrachtet. Diese zeigen eine ausgezeichnete Übereinstimmung mit dem Experiment. Im Allgemeinen kann dieser Ansatz subtile Unterschiede zwischen Kristallstrukturen und Lösungsstrukturen von Proteinen aufzeigen und liefert eine Methode um beide Strukturen miteinander in Einklang zu bringen. Dabei wird nur ein minimaler Satz an experimentellen NMR Daten benötigt. Dieser Ansatz kann auf die gleiche Weise bei Membranproteinen mit schlecht aufgelösten Strukturen sowie bei Proteinstrukturen, die nicht vollständig durch Lösungs-NMR erklärt werden können (z.B. große Proteine), verwendet werden.

Diese Untersuchungen zeigen, dass eine völlig konsistente, von ersten Prinzipien ausgehende Betrachtung, von Molekulardynamik bis hin zu spektroskopischen ab initio Observablen, deren Ensemble-Mittelwert gebildet wurde, zu signifikanten Verbesserungen in der Übereinstimmung zwischen Theorie und Experiment führt. Außerdem ermöglicht dies Einblicke, die nicht direkt aus der Betrachtung der experimentellen Ergebnisse zu bekommen sind.

Bibliography

- Abragam, A. and Bleaney, B. [1970], *Electron Paramagnetic Resonance of Transition Ions*, Monographs on Physics, Oxford University Press.
- Al Derzi, A. R., Fau, S. and Bartlett, R. J. [2003], 'Benchmark study of isotropic hyperfine coupling constants for hydrogen: Influence of geometry, correlation method, and basis set', *J. Phys. Chem. A* **107**(34), 6656–6667.
- Andrec, M., Snyder, D. A., Zhou, Z., Young, J., Montelione, G. T. and Levy, R. M. [2007], 'A large data set comparison of protein structures determined by crystallography and NMR: statistical test for structural differences and the effect of crystal packing.', *Proteins* **69**(3), 449–65.
- Angstl, R. [1989], 'Contribution of the relativistic mass correction to the g tensor of molecules', *Chem. Phys.* **132**(3), 435–442.
- Arbuznikov, A. V., Kaupp, M., Malkin, V. G., Reviakine, R. and Malkina, O. L. [2002], 'Validation study of meta-GGA functionals and of a model exchange–correlation potential in density functional calculations of EPR parameters', *Phys. Chem. Chem. Phys.* **4**(22), 5467–5474.
- Asenbaum, A., Pruner, C., Wilhelm, E., Mijakovic, M., Zoranic, L., Sokolic, F., Kezic, B. and Perera, A. [2012], 'Structural changes in ethanol–water mixtures: Ultrasonics, Brillouin scattering and molecular dynamics studies', *Vib. Spectrosc.* **60**, 102–106.
- Asher, J. R., Doltsinis, N. L. and Kaupp, M. [2004], 'Ab initio molecular dynamics simulations and g-tensor calculations of aqueous benzosemiquinone radical anion: effects of regular and "T-stacked" hydrogen bonds.', *J. Am. Chem. Soc.* **126**(31), 9854–61.
- Asher, J. R. and Kaupp, M. [2007], 'Hyperfine coupling tensors of the benzosemiquinone radical anion from Car-Parrinello molecular dynamics.', *ChemPhysChem* **8**(1), 69–79.
- Bagotsky, V. S. [2005], *Fundamentals of Electrochemistry*, Vol. 44, Wiley-Interscience.
- Barone, V., Brustolon, M., Cimino, P., Polimeno, A., Zerbetto, M. and Zoleo, A. [2006], 'Development and validation of an integrated computational approach for the modeling of cw-ESR spectra of free radicals in solution: p-(methylthio)phenyl nitronyl nitroxide in toluene as a case study.', *J. Am. Chem. Soc.* **128**(49), 15865–73.
- Barone, V. and Cimino, P. [2009], 'Validation of the B3LYP/N07D and PBE0/N07D computational models for the calculation of electronic g-tensors', *J. Chem. Theory Comput.* **5**(1), 192–199.
- Beier, T., Lindgren, I., Persson, H., Salomonson, S., Sunnergren, P., Häffner, H. and Hermanspahn, N. [2000], ' g_j factor of an electron bound in a hydrogenlike ion', *Phys. Rev. A* **62**(3), 032510.
- Bennett, J. and Ingram, D. [1955], 'Paramagnetic resonance in copper phthalocyanine', *Nature* **175**, 130–131.

- Bertini, I., Kursula, P., Luchinat, C., Parigi, G., Vahokoski, J., Wilmanns, M. and Yuan, J. [2009], 'Accurate solution structures of proteins from X-ray data and a minimal set of NMR data: calmodulin-peptide complexes as examples.', *J. Am. Chem. Soc.* **131**(14), 5134–44.
- Billeter, M., Vendrell, J., Wider, G., Avilés, F. X., Coll, M., Guasch, A., Huber, R. and Wüthrich, K. [1992], 'Comparison of the NMR solution structure with the X-ray crystal structure of the activation domain from procarboxypeptidase B', *J. Biomol. NMR* **2**(1), 1–10.
- Breit, G. [1929], 'The effect of retardation on the interaction of two electrons', *Phys. Rev.* **34**(4), 553–573.
- Breit, G. [1932], 'Dirac's equation and the spin-spin interactions of two electrons', *Phys. Rev.* **39**(4), 616–624.
- Callaghan, P. T. [2011], *Translational Dynamics and Magnetic Resonance : Principles of Pulsed Gradient Spin Echo NMR*, Oxford University Press.
- Car, R. and Parrinello, M. [1985], 'Unified approach for molecular dynamics and density-functional theory', *Phys. Rev. Lett.* **55**(22), 2471–2474.
- Carrington, A. and McLachlan, A. D. [1967], *Introduction to magnetic resonance with applications to chemistry and chemical physics*, Harper & Row.
- Chesnut, D. B. [1996], The ab initio computation of nuclear magnetic resonance chemical shielding, in K. B. Lipkowitz and D. B. Boyd, eds, 'Reviews in Computational Chemistry', Vol. 8, Wiley-VCH, pp. 245–297.
- Corsaro, C., Maisano, R., Mallamace, D. and Dugo, G. [2013], '1H NMR study of water/methanol solutions as a function of temperature and concentration', *Physica A* **392**(4), 596–601.
- Declerck, R. [2008], The Calculation of EPR parameters in periodic systems, PhD thesis, Universiteit Gent.
- Declerck, R., Van Speybroeck, V. and Waroquier, M. [2006], 'First-principles calculation of the EPR g tensor in extended periodic systems', *Phys. Rev. B* **73**(11), 1–8.
- Dirac, P. A. [1928], 'The quantum theory of the electron', *Proc. R. Soc. A* **117**(778), 610–624.
- Dixit, S., Crain, J., Poon, W. C. K., Finney, J. L. and Soper, a. K. [2002], 'Molecular segregation observed in a concentrated alcohol-water solution.', *Nature* **416**(6883), 829–32.
- Duerring, M., Huber, R. and Bode, W. [1988], 'The structure of γ -N-methylasparagine in C-phycocyanin from *Mastigocladus laminosus* and *Agmenellum quadruplicatum*', *FEBS Lett.* **236**(1), 167–170.
- Elgabarty, H., Schmieder, P. and Sebastiani, D. [2013], 'Unraveling the existence of dynamic water channels in light-harvesting proteins: alpha-C-phycocyanobilin in vitro', *Chem. Sci.* **4**, 755–763.
- Essmann, U., Perera, L., Berkowitz, M. L., Darden, T., Lee, H. and Pedersen, L. G. [1995], 'A smooth particle mesh Ewald method', *J. Chem. Phys.* **103**(19), 8577.
- Ewald, P. P. [1921], 'Die Berechnung optischer und elektrostatischer Gitterpotentiale', *Ann. Phys.* **369**(3), 253–287.
- Frémy, E. [1845], 'Sur une nouvelle série d'acides formés d'oxygène, de soufre, d'hydrogène et d'azote', *Ann. Chim. Phys.* **15**, 408–488.

- Frenkel, D. and Smit, B. [2001], *Understanding Molecular Simulation: From Algorithms to Applications*, Vol. 1 of *Computational Science Series*, 2 edn, Academic Press.
- Frisch, M. J., Trucks, G. W., Schlegel, H. B., Scuseria, G. E., Robb, M. A., Cheeseman, J. R., Scalmani, G., Barone, V., Mennucci, B., Petersson, G. A., Nakatsuji, H., Caricato, M., Li, X., Hratchian, H. P., Izmaylov, A. E., Bloino, J., Zheng, G., Sonnenberg, J. L., Hada, M., Ehara, M., Toyota, K., Fukuda, R., Hasegawa, J., Ishida, M., Nakajima, T., Honda, Y., Kitao, O., Nakai, H., Vreven, T., Montgomery, Jr., J. A., Peralta, J. E., Ogliaro, F., Bearpark, M., Heyd, J. J., Brothers, E., Kudin, K. N., Staroverov, V. N., Kobayashi, R., Normand, J., Raghavachari, K., Rendell, A., Burant, J. C., Iyengar, S. S., Tomasi, J., Cossi, M., Rega, N., Millam, J. M., Klene, M., Knox, J. E., Cross, J. B., Bakken, V., Adamo, C., Jaramillo, J., Gomperts, R., Stratmann, R. E., Yazyev, O., Austin, A. J., Cammi, R., Pomelli, C., Ochterski, J. W., Martin, R. L., Morokuma, K., Zakrzewski, V. G., Voth, G. A., Salvador, P., Dannenberg, J. J., Dapprich, S., Daniels, A. D., Farkas, O., Foresman, J. B., Ortiz, J. V., Cioslowski, J. and Fox, D. J. [2009], 'Gaussian 09 Revision A.02'. Gaussian Inc. Wallingford CT 2009.
- Gauss, J. and Cremer, D. [1992], 'Analytical energy gradients in Möller-Plesset perturbation and quadratic configuration interaction methods: Theory and application', *Adv. Quantum Chem.* **23**, 205–299.
- Gauss, J., Kállay, M. and Neese, F. [2009], 'Calculation of electronic g-tensors using coupled cluster theory', *J. Phys. Chem. A* **113**(43), 11541–9.
- Gauss, J. and Stanton, J. F. [1995a], 'Coupled-cluster calculations of nuclear magnetic resonance chemical shifts', *J. Chem. Phys.* **103**(9), 3561.
- Gauss, J. and Stanton, J. F. [1995b], 'Gauge-invariant calculation of nuclear magnetic shielding constants at the coupled-cluster singles and doubles level', *J. Chem. Phys.* **102**(1), 251.
- Gauss, J. and Stanton, J. F. [1996], 'Perturbative treatment of triple excitations in coupled-cluster calculations of nuclear magnetic shielding constants', *J. Chem. Phys.* **104**(7), 2574.
- Goedecker, S., Teter, M. and Hutter, J. [1996], 'Separable dual-space Gaussian pseudopotentials', *Phys. Rev. B* **54**(3), 1703–1710.
- Griffith, J. S. [1960], 'Some investigations in the theory of open-shell ions', *Mol. Phys.* **3**(1), 79–89.
- Griffith, J. S. [1964], *The Theory of Transition-metal Ions*, Cambridge University Press.
- Grimmer, A. [1993], Shielding tensor data and structure: the bond-related chemical shift concept, in J. Tossell, ed., 'Nuclear magnetic shieldings and molecular structure', Vol. 386, Kluwer Academic Publishers, Dordrecht, pp. 191–201.
- Guennebaud, G., Jacob, B. et al. [2010], 'Eigen v3', <http://eigen.tuxfamily.org>.
- Guo, J.-H., Luo, Y., Augustsson, A., Kashtanov, S., Rubensson, J.-E., Shuh, D. K., Ågren, H. and Nordgren, J. [2003], 'Molecular structure of alcohol-water mixtures', *Phys. Rev. Lett.* **91**(15), 157401.
- Hahn, J., Kühne, R. and Schmieder, P. [2007], 'Solution-state (15)N NMR spectroscopic study of alpha-C-phycocyanin: implications for the structure of the chromophore-binding pocket of the cyanobacterial phytochrome Cph1.', *Chembiochem* **8**(18), 2249–55.
- Haile, J. M. [1992], *Molecular Dynamics Simulation: Elementary Methods*, John Wiley & Sons, Inc.
- Halgren, T. a. [1996], 'Merck molecular force field. I. Basis, form, scope, parameterization, and performance of MMFF94', *J. Comput. Chem.* **17**(5-6), 490–519.

- Harriman, J. E. [1978], *Theoretical foundations of electron spin resonance*, Academic Press.
- Hartwigsen, C., Goedecker, S. and Hutter, J. [1998], 'Relativistic separable dual-space Gaussian pseudopotentials from H to Rn', *Phys. Rev. B* **58**(7), 3641.
- Heller, J., Elgabarty, H., Zhuang, B., Sebastiani, D. and Hinderberger, D. [2010], 'Solvation of small disulfonate anions in water/methanol mixtures characterized by high-field pulse electron nuclear double resonance and molecular dynamics simulations.', *J. Phys. Chem. B* **114**(22), 7429–38.
- Hinchliffe, A. and Munn, R. W. [1985], *Molecular Electromagnetism*, Wiley.
- Hinderberger, D., Spiess, H. W. and Jeschke, G. [2004], 'Dynamics, site binding, and distribution of counterions in polyelectrolyte solutions studied by electron paramagnetic resonance spectroscopy', *J. Phys. Chem. B* **108**(12), 3698–3704.
- Hohenberg, P. and Kohn, W. [1964], 'Inhomogeneous electron gas', *Phys. Rev. B* **136**(3B), B864.
- Hoover, W. [1985], 'Canonical dynamics: Equilibrium phase-space distributions', *Phys. Rev. A* **31**(3), 1695–1697.
- Hsiao, Y.-W., Sanchez-Garcia, E., Doerr, M. and Thiel, W. [2010], 'Quantum refinement of protein structures: implementation and application to the red fluorescent protein DsRed.M1.', *J. Phys. Chem. B* **114**(46), 15413–23.
- Ihrig, A. C., Schiffmann, C. and Sebastiani, D. [2011], 'Specific quantum mechanical/molecular mechanical capping-potentials for biomolecular functional groups.', *Chem. Phys.* **135**(21), 214107.
- Ingram, D. and Bennett, J. [1954], 'Paramagnetic resonance in phthalocyanine, chlorophyll, and haemoglobin derivatives', *J. Chem. Phys.* **22**(6), 1136–1137.
- Jeschke, G. [2013], 'Conformational dynamics and distribution of nitroxide spin labels', *Prog. Nucl. Magn. Reson. Spectrosc.* **72**, 42–60.
- Kaupp, M., Bühl, M. and Malkin, V. G., eds [2006], *Calculation of NMR and EPR Parameters*, Wiley-VCH.
- Kirchmair, J., Markt, P., Distinto, S., Schuster, D., Spitzer, G. M., Liedl, K. R., Langer, T. and Wolber, G. [2008], 'The Protein Data Bank (PDB), its related services and software tools as key components for in silico guided drug discovery.', *J. Med. Chem.* **51**(22), 7021–40.
- Koch, W. and Holthausen, M. C. [2000], *A chemist's guide to density functional theory*, Wiley-VCH.
- Kohn, W. and Sham, L. J. [1965], 'Self-consistent equations including exchange and correlation effects', *Phys. Rev.* **140**(4A), A1133–A1138.
- Kutzelnigg, W. [2004], Fundamentals of nonrelativistic and relativistic theory of NMR and EPR parameters, in M. Kaupp, M. Bühl and V. G. Malkin, eds, 'Calculation of NMR and EPR Parameters: Theory and Applications', Wiley-VCH Verlag GmbH & Co. KGaA, Weinheim, FRG., chapter 5, pp. 43–82.
- Lebedev, V. I. and Laikov, D. [1999], A quadrature formula for the sphere of the 131st algebraic order of accuracy, in 'Dokl. Math.', Vol. 59, MAIK Nauka/Interperiodica, pp. 477–481.
- Lennard-Jones, J. E. [1924], 'On the determination of molecular fields-II. from the equation of state of a gas', *Proc. R. Soc. A* **106**(738), 463–477.

- Lin, K., Hu, N., Zhou, X., Liu, S. and Luo, Y. [2012], 'Reorientation dynamics in liquid alcohols from Raman spectroscopy', *J. Raman Spectrosc.* **43**(1), 82–88.
- Lippert, G., Hutter, J. and Parrinello, M. [1997], 'A hybrid Gaussian and plane wave density functional scheme', *Mol. Phys.* **92**(3), 477–488.
- Lippert, G., Hutter, J. and Parrinello, M. [1999], 'The Gaussian and augmented-plane-wave density functional method for ab initio molecular dynamics simulations', *Theor. Chem. Acc.* **103**(2), 124–140.
- Löwdin, P.-O. [1951], 'A note on the quantum-mechanical perturbation theory', *J. Chem. Phys.* **19**(11), 1396.
- Löwdin, P.-O. [1959], 'Correlation problem in many-electron quantum mechanics. I. Review of different approaches and discussion of some current ideas', *Adv. Chem. Phys.* **2**, 207–322.
- Löwdin, P.-O. [1963], 'Studies in perturbation theory Part I. An elementary iteration-variation procedure for solving the Schrödinger equation by partitioning technique', *J. Mol. Spectrosc.* **10**(1-6), 12–33.
- Lund, A., Macomber, L. D., Danilczuk, M., Stevens, J. E. and Schlick, S. [2007], 'Determining the geometry and magnetic parameters of fluorinated radicals by simulation of powder ESR spectra and DFT calculations: the case of the radical RCF₂CF₂* in nafion perfluorinated ionomers.', *J. Phys. Chem. B* **111**(32), 9484–91.
- MacKerell, A. D., Bashford, D., Dunbrack, R. L., Evanseck, J. D., Field, M. J., Fischer, S., Gao, J., Guo, H., Ha, S., Joseph-McCarthy, D., Kuchnir, L., Kuczera, K., Lau, F. T. K., Mattos, C., Michnick, S., Ngo, T., Nguyen, D. T., Prodhom, B., Reiher, W. E., Roux, B., Schlenkrich, M., Smith, J. C., Stote, R., Straub, J., Watanabe, M., Wiórkiewicz-Kuczera, J., Yin, D. and Karplus, M. [1998], 'All-Atom Empirical Potential for Molecular Modeling and Dynamics Studies of Proteins', *J. Phys. Chem. B* **102**(18), 3586–3616.
- Mackerell, A. D., Feig, M. and Brooks, C. L. [2004], 'Extending the treatment of backbone energetics in protein force fields: limitations of gas-phase quantum mechanics in reproducing protein conformational distributions in molecular dynamics simulations.', *J. Comput. Chem.* **25**(11), 1400–15.
- Malkin, V. G., Malkina, O. L., Eriksson, L. A. and Salahub, D. R. [1995], The Calculation of NMR and ESR Spectroscopy Parameters Using Density Functional Theory, in J. Seminario and P. Politzer, eds, 'Modern Density Functional Theory A Tool for Chemistry', Vol. 2, Elsevier, pp. 273–347.
- Malkina, O. L., Vaara, J., Schimmelpfennig, B., Munzarova, M., Malkin, V. G. and Kaupp, M. [2000], 'Density functional calculations of electronic g-tensors using spin-orbit pseudopotentials and mean-field all-electron spin-orbit operators', *J. Am. Chem. Soc.* **122**, 9206–9218.
- Marcus, Y. [2002], *Solvent mixtures: properties and selective solvation*, 1 edn, CRC Press.
- Martin, M. G. and Siepmann, J. I. [1998], 'Transferable potentials for phase equilibria. 1. United-atom description of n-alkanes', *J. Phys. Chem. B* **102**(14), 2569–2577.
- Martin, R. M. [2004], *Electronic Structure: Basic Theory and Practical Methods*, Cambridge University Press.
- Martyna, G. J., Klein, M. L. and Tuckerman, M. [1992], 'Nosé-Hoover chains: the canonical ensemble via continuous dynamics', *J. Chem. Phys.* **97**, 2635.
- McWeeny, R. [1959], 'The density matrix in many-electron quantum mechanics. I. generalized

- product functions. factorization and physical interpretation of the density matrices', *Proc. R. Soc. A* **253**(1273), 242–259.
- McWeeny, R. [1965], 'On the origin of spin-Hamiltonian parameters', *J. Chem. Phys.* **42**(5), 1717.
- McWeeny, R. [1989], *Methods of Molecular Quantum Mechanics*, Theoretical Chemistry; A Series of Monographs, second edn, Academic Press.
- McWeeny, R. [2004], *Spins in Chemistry*, Dover Publications.
- Moser, W. and Howie, R. A. [1968], 'Nitrosodisulphonates. Part I. Fremy's salt (potassium nitrosodisulphonate)', *J. Chem. Soc. A* p. 3039.
- Moss, R. E. [1973], *Advanced molecular quantum mechanics. An introduction to relativistic quantum mechanics and the quantum theory of radiation*, John Wiley and Sons, Inc., New York.
- Murakhtina, T., Heuft, J., Meijer, E. J. and Sebastiani, D. [2006], 'First principles and experimental ^1H NMR signatures of solvated ions: The case of HCl(aq) .', *ChemPhysChem* **7**(12), 2578–84.
- Neese, F. [2001], 'Prediction of electron paramagnetic resonance g values using coupled perturbed Hartree–Fock and Kohn–Sham theory', *J. Chem. Phys.* **115**(24), 11080.
- Neese, F. [2004], 'Sum-over-states based multireference ab initio calculation of EPR spin Hamiltonian parameters for transition metal complexes. A case study.', *Magn. Reson. Chem.* **42 Spec no**, S187–98.
- Neese, F. [2005], 'Efficient and accurate approximations to the molecular spin-orbit coupling operator and their use in molecular g-tensor calculations.', *Chem. Phys.* **122**(3), 34107.
- Neese, F. [2007], Quantum chemical approaches to spin-Hamiltonian parameters, in B. G. Gilbert, M. B. Davies and D. M. Murphy, eds, 'Electron Paramagnetic Resonance', Vol. 20, The Royal Society of Chemistry, chapter 4, pp. 73–95.
- Neese, F. and Munzarova, M. L. [2004], Historical aspects of EPR parameter calculations, in M. Kaupp, M. Bühl and V. G. Malkin, eds, 'Calculation of NMR and EPR Parameters: Theory and Applications', Wiley-VCH Verlag GmbH & Co. KGaA, Weinheim, FRG., chapter 3, pp. 21–32.
- Nitzan, A. [2006], *Chemical Dynamics in Condensed Phases: Relaxation, Transfer, and Reactions in Condensed Molecular Systems*, Oxford University Press.
- Nosé, S. [1984a], 'A molecular dynamics method for simulations in the canonical ensemble', *Mol. Phys.* **52**(2), 255–268.
- Nosé, S. [1984b], 'A unified formulation of the constant temperature molecular dynamics methods', *J. Chem. Phys.* **81**(1), 511.
- Patra, M., Karttunen, M., Hyvönen, M. T., Falck, E., Lindqvist, P. and Vattulainen, I. [2003], 'Molecular dynamics simulations of lipid bilayers: major artifacts due to truncating electrostatic interactions', *Biophys. J.* **84**(6), 3636.
- Pauwels, E., Asher, J., Kaupp, M. and Waroquier, M. [2011], 'Cluster or periodic, static or dynamic—the challenge of calculating the g tensor of the solid-state glycine radical.', *Phys. Chem. Chem. Phys.* **13**(41), 18638–46.

- Pavone, M., Benzi, C., De Angelis, F. and Barone, V. [2004], 'Hyperfine coupling constants of dimethyl nitroxide in aqueous solution: Car-Parrinello molecular dynamics and discrete-continuum approaches', *Chem. Phys. Lett.* **395**(1-3), 120–126.
- Pavone, M., Cimino, P., Crescenzi, O., Sillanpää, A. and Barone, V. [2007], 'Interplay of intrinsic, environmental, and dynamic effects in tuning the EPR parameters of nitroxides: further insights from an integrated computational approach.', *J. Phys. Chem. B* **111**(30), 8928–39.
- Pavone, M., Cimino, P., De Angelis, F. and Barone, V. [2006], 'Interplay of stereoelectronic and environmental effects in tuning the structural and magnetic properties of a prototypical spin probe: further insights from a first principle dynamical approach.', *J. Am. Chem. Soc.* **128**(13), 4338–47.
- Pavone, M., Sillanpää, A., Cimino, P., Crescenzi, O. and Barone, V. [2006], 'Evidence of variable H-bond network for nitroxide radicals in protic solvents.', *J. Phys. Chem. B* **110**(33), 16189–92.
- Perdew, J. P. and Schmidt, K. [2001], Jacob's ladder of density functional approximations for the exchange-correlation energy, in 'AIP Conference Proceedings', Vol. 577, AIP, pp. 1–20.
- Pilbrow, J. R. [1994], 'EPR spectroscopy of poorly characterized systems: A historical and current view', *Appl. Magn. Reson.* **6**(1-2), 161–181.
- Poole, C. P. and Farach, H. A. [1971], *Relaxation in magnetic resonance: dielectric and Mössbauer applications*, Academic Press.
- Praissman, M. [1964], 'The comparison of protein structure in the crystal and in solution using tritium-hydrogen exchange', *J. Am. Chem. Soc.* **86**(17), 3584–3585.
- Pryce, M. H. L. [1950], 'A modified perturbation procedure for a problem in paramagnetism', *Proc. R. Soc. A* **63**(1), 25–29.
- Pyykkö, P. [2004], Theory of NMR parameters. From Ramsey to relativity, 1953 to 1983, in M. Kaupp, M. Bühl and V. G. Malkin, eds, 'Calculation of NMR and EPR Parameters: Theory and Applications', Wiley-VCH Verlag GmbH & Co. KGaA, Weinheim, FRG., chapter 3, pp. 7–19.
- Rapaport, D. C. [2004], *The art of molecular dynamics simulation*, Cambridge university press.
- Rappe, A. K., Casewit, C. J., Colwell, K., Goddard Iii, W. and Skiff, W. [1992], 'UFF, a full periodic table force field for molecular mechanics and molecular dynamics simulations', *J. Am. Chem. Soc.* **114**(25), 10024–10035.
- Reichardt, C. and Welton, T. [2011], *Solvents and solvent effects in organic chemistry*, wiley-VCH.
- Röben, M. and Schmieder, P. [2011], 'Assignment of phycocyanobilin in HMPT using triple resonance experiments.', *Magn. Reson. Chem.* **49**(9), 543–548.
- Rohmer, T., Lang, C., Hughes, J., Essen, L.-o., Gärtner, W. and Matysik, J. [2008], 'Light-induced chromophore activity and signal transduction in phytochromes observed by ¹³C and ¹⁵N magic-angle spinning NMR.', *Proc. Natl. Acad. Sci. USA* **105**(40), 15229–34.
- Ryde, U. and Nilsson, K. [2003], 'Quantum chemistry can locally improve protein crystal structures.', *J. Am. Chem. Soc.* **125**(47), 14232–3.
- Sauer, S. P. A. [2011], *Molecular Electromagnetism: A Computational Chemistry Approach*, Oxford University Press.

- Schiffmann, C. and Sebastiani, D. [2011], 'Artificial bee colony optimization of capping potentials for hybrid quantum mechanical/molecular mechanical calculations', *J. Chem. Theory Comput.* **7**(5), 1307–1315.
- Schirmer, T., Bode, W. and Huber, R. [1987], 'Refined three-dimensional structures of two cyanobacterial C-phycocyanins at 2.1 and 2.5 Å resolution. A common principle of phycobilin-protein interaction.', *J. Mol. Biol.* **196**(3), 677–95.
- Schmidt, J., Hutter, J., Spiess, H.-W. and Sebastiani, D. [2008], 'Beyond isotropic tumbling models: nuclear spin relaxation in liquids from first principles.', *ChemPhysChem* **9**(16), 2313–6.
- Schweiger, A. and Jeschke, G. [2001], *Principles of pulse electron paramagnetic resonance*, Oxford University Press.
- Searles, D. J. and Huber, H. [2004], Molecular dynamics and NMR parameter calculations, in M. Kaupp, M. Bühl and V. G. Malkin, eds, 'Calculation of NMR and EPR Parameters: Theory and Applications', Wiley-VCH Verlag GmbH & Co. KGaA, chapter 11, pp. 175–189.
- Sebastiani, D. and Parrinello, M. [2001], 'A new *ab-Initio* approach for NMR chemical shifts in periodic systems', *J. Phys. Chem. A* **105**(10), 1951–1958.
- Sebastiani, D. and Rothlisberger, U. [2004], 'Nuclear magnetic resonance chemical shifts from hybrid DFT QM/MM calculations', *J. Phys. Chem. B* **108**(9), 2807–2815.
- Shankar, R. [1994], *Principles of Quantum Mechanics*, second edn, Plenum Press, New York.
- Simons, J. and Nichols, J. [1997], *Quantum Mechanics in Chemistry*, Oxford University Press, USA.
- Slichter, C. P. [1996], *Principles of Magnetic Resonance*, Springer.
- Snyder, D. a., Chen, Y., Denissova, N. G., Acton, T., Aramini, J. M., Ciano, M., Karlin, R., Liu, J., Manor, P., Rajan, P. a., Rossi, P., Swapna, G. V. T., Xiao, R., Rost, B., Hunt, J. and Montelione, G. T. [2005], 'Comparisons of NMR spectral quality and success in crystallization demonstrate that NMR and X-ray crystallography are complementary methods for small protein structure determination.', *J. Am. Chem. Soc.* **127**(47), 16505–11.
- Stevensson, B. and Edén, M. [2006], 'Efficient orientational averaging by the extension of Lebedev grids via regularized octahedral symmetry expansion.', *J. Magn. Reson.* **181**(1), 162–76.
- Stoll, S. and Schweiger, A. [2003], 'An adaptive method for computing resonance fields for continuous-wave EPR spectra', *Chem. Phys. Lett.* **380**(3-4), 464–470.
- Stone, a. J. [1963], 'Gauge invariance of the g tensor', *Proc. R. Soc. A* **271**(1346), 424–434.
- Stoneham, A. M. [1969], 'Shapes of inhomogeneously broadened resonance lines in solids', *Rev. Mod. Phys.* **41**(1), 82–108.
- Swope, W. C., Andersen, H. C., Berens, P. H. and Wilson, K. R. [1982], 'A computer simulation method for the calculation of equilibrium constants for the formation of physical clusters of molecules: Application to small water clusters', *J. Chem. Phys.* **76**, 637.
- Tuckerman, M. [2010], *Statistical Mechanics: Theory and Molecular Simulation*, Oxford University Press.
- van Lenthe, E., Baerends, E.-J. and Snijders, J. G. [1993], 'Relativistic regular two-component Hamiltonians', *J. Chem. Phys.* **99**, 4597–4597.

- van Lenthe, E., Baerends, E.-J. and Snijders, J. G. [1994], 'Relativistic total energy using regular approximations', *J. Chem. Phys.* **101**, 9783.
- VandeVondele, J., Iannuzzi, M. and Hutter, J. [2006], Large scale condensed matter calculations using the gaussian and augmented plane waves method, in M. Ferrario, G. Ciccotti and K. Binder, eds, 'Computer Simulations in Condensed Matter Systems: From Materials to Chemical Biology Volume 1', Vol. 703 of *Lecture Notes in Physics*, Springer Berlin Heidelberg, Berlin, Heidelberg, pp. 287–314.
- VandeVondele, J., Krack, M., Mohamed, F., Parrinello, M., Chassaing, T. and Hutter, J. [2005], 'Quickstep: Fast and accurate density functional calculations using a mixed Gaussian and plane waves approach', *Comput. Phys. Commun.* **167**(2), 103–128.
- Vanommeslaeghe, K. and Mackerell, A. D. [2012], 'Automation of the CHARMM General Force Field (CGenFF) I: bond perception and atom typing.', *J. Chem. Inf. Model.* **52**(1), 3144–3154.
- Verlet, L. [1967], 'Computer" experiments" on classical fluids. I. Thermodynamical properties of Lennard-Jones molecules', *Phys. Rev.* **159**(1), 98.
- Vila, J. a. and Scheraga, H. a. [2009], 'Assessing the accuracy of protein structures by quantum mechanical computations of $^{13}\text{C}(\alpha)$ chemical shifts.', *Acc. Chem. Res.* **42**(10), 1545–53.
- Weber, V., Iannuzzi, M., Giani, S., Hutter, J., Declerck, R. and Waroquier, M. [2009], 'Magnetic linear response properties calculations with the Gaussian and augmented-plane-wave method.', *Chem. Phys.* **131**(1), 014106.
- Yang, L.-W., Eyal, E., Chennubhotla, C., Jee, J., Gronenborn, A. M. and Bahar, I. [2007], 'Insights into equilibrium dynamics of proteins from comparison of NMR and X-ray data with computational predictions.', *Structure* **15**(6), 741–9.